Influence of the Post-Weld Heat Treatment on the Low-Temperature Toughness of ERW API X70 Line Pipe

by

Neil Ernest Anderson

A thesis submitted in partial fulfillment of the requirements for the degree of

Master of Science

in

Materials Engineering

Department of Chemical and Materials Engineering
University of Alberta

Abstract

Increasingly stricter performance requirements of pipelines are being driven by regulatory bodies, the energy industry, and public interest in protecting public safety, health, and the environment. A critical mechanical property influencing performance is toughness, and particular interest is focused on toughness performance at low temperatures (down to -45 °C). Toughness is typically measured by impact testing at the temperature of interest, with industry typically using the Charpy V-Notch impact test.

A study was conducted to identify the metallurgical factors influencing low-temperature toughness performance of grade API X70 pipe longitudinal weld seams manufactured by electric resistance welding. The electric resistance welding bondline is known to have different post-welding heat treatments and there is a specific interest in -45 °C performance. The investigation was undertaken using advanced characterization techniques, including electron backscatter diffraction and transmission scanning electron microscopy, and found that low-temperature toughness was correlated with post-weld heat treatments.

Post-welding heat treatment was observed to produce a fine-grained, allotriomorphic ferrite at the bondline. It was found that certain post-welding heat treatments produced predominantly coarse bainitic structures in the weld seam near the bondline, while others produced fine allotriomorphic ferrite homogeneous with the bondline. Martensite-austenite (M-A) constituents were also observed. Low-temperature toughness performance was observed to be higher in specimens which exhibited a homogeneous weld seam composed of fine-grained, equiaxed, allotriomorphic ferrite, with predominantly high angle grain boundaries (greater than 10°), minimized M-A size and fraction, and lower material strain. No crystallographic texture was observed in any of the specimens. Additionally, low toughness performance was observed in specimens with a soft-zone in the weld seam within 100-150 μm of the bondline. This soft-zone is suspected to be due to the development of a dual-phase microstructure in the weld seam adjacent to the bondline.

A design-of-experiment study was conducted to gain insight into the microstructural development during post-weld heat treatment, specifically investigating the effect of varying peak temperatures on low-temperature toughness. A Gleeble thermomechanical simulator was used to create Charpy V-Notch specimens and conduct dilatometry investigations. A correlation was found between $NbC_{0.87}$ precipitate solubility and phase transformation behaviour. These observations agreed with published literature and thermodynamic calculations regarding the role of MX type precipitates as austenite grain refiners, soluble Nb in austenite retarding the diffusional austenite-to-ferrite transformations, and soluble C in austenite promoting displacive austenite-to-ferrite transformations. Post-weld heat treatments which exceeded the critical temperature for complete precipitate solubility were found to produce a weld seam with a predominantly coarse-grained, bainitic microstructure adjacent to the bondline. This was inhomogeneous with the fine-grained, equiaxed, allotriomorphic bondline, and had less desirable low-temperature toughness performance. Post-weld heat treatments below the critical temperature for complete precipitate solubility were found to result in a homogeneous, fine-grained, equiaxed allotriomorphic ferrite weld seam and improved low-temperature toughness performance.

Inferring from this work, a hypothesis is proposed regarding the role of MX type precipitate formers on the microstructural development, and suggestions are given for the further work required to prove this hypothesis.

"A pseudo scientist, who uses undetermined suppositions, indefinite theories, and inexpressible hypotheses; which are based on unreliable information, uncertain quantities, and incomplete data; derived from non-reproducible experiments and incomplete investigations; using equipment and instruments of questionable accuracy, insufficient resolution, and inadequate sensitivity, to arrive at timid, tentative, cloudy, abstruse, and non-committed conclusions prefaced by the phrase, "IT DEPENDS"."

– Definition of a Metallurgist, Unknown

"An expert is a man who has made all the mistakes which can be made in a very narrow field."

– Niels Bohr

Acknowledgements

This project has been one where I have been incredibly fortunate to benefit from a great deal of mentorship, support, and enriching company. There are many people whose efforts I would like to acknowledge.

First, a great deal of this journey would not have been possible without my graduate studies supervisor, Dr. Leijun Li, whose supervision and mentorship has been exceptional. Dr. Li's patience, impressive technical knowledge, and friendly, approachable personality have been a bedrock of support. His belief in my capabilities has been inspirational, and I have been able to see marked growth both personally and technically under his tutelage. I have greatly enjoyed our discussions, and hope to be able to continue them in the future. Thank you.

I have also been extremely lucky in being able to draw on the experience of with industrial experts Dr. Laurie Collins, Dr. Muhammad Rashid, and Dr. Atish Ray. Thank you for ensuring that my academic studies never strayed too far from the realm of reality; I am, after all, an engineer.

I would like to thank the defence committee of Dr. Renato Macciotta Pulisci, Dr. Barry Wiskel, and Dr. Vinay Prasad for their time and consideration. I appreciate the resources which have been graciously provided by the Department of Chemical and Materials Engineering (CME) at the University of Alberta faculties Dr. Hani Henein, Dr. Barry Wiskel, and associate chair Dr. Vinay Prasad, through equipment access, knowledge and advice. Support from Lily Laser, Mia Law, Marion Pritchard, Kevin Heidebrecht, Walter Boddez, and the CME machine shop has been invaluable. I also appreciate the access to nanoFAb and assistance of nanoFAB staff.

I would also like to acknowledge Joseph Caputo of CME as a reader and reviewer of this thesis, and I am gratefully indebted to him for his valuable comments on this thesis.

I would like to sincerely thank my colleagues in our research group for their camaraderie, mentorship, discussions, and assistance: Dr. Yiyu Wang, Chris Di Giovanni, Rebekah Bannister, Rangasayee Kannan, Lieduo Yang, Lulu Guo, Rishav Raj, Mingzhang Yang, and Vini Dheer. Special thanks goes to Yiyu and Rangasayee for their mentorship and technical skills; I learned an incredible amount from your leadership, activities, and discussions. Very heartfelt thanks also goes to Rebekah for her assistance with the dilatometry work in this study; without your expertise much of this work would not have been possible. I would also like to acknowledge the assistance of Mingzhang Yang and Vini Dheer in gathering optical microscopy and hardness data. I hope to have an opportunity to work with all of you again in the future.

I would like to express my thanks and appreciation to the many other mentors I have been able to consult for advice with throughout my time here: Dr. Elizabeth Lee, Mr. Matthew Bell, and Mr. Greg Nelson, as well as the ESRM team of Mr. Gord Winkel, Dr. Norman Nibber, Dr. Lianne Lefsrud, Mr. John Cochio, and Ms. Ellen Watson, and Nicholas Bak, among others.

Financial support for this work came from the Natural Sciences and Engineering Research Council (NSERC) of Canada and Evraz North America, Inc., whom also supplied equipment access, material, and valuable subject matter expert time. My studies were also supported by scholarships from the University of Alberta and the Association of Iron and Steel Technologies.

Last but not least, thank you to my family, especially my parents, Eileen and E. Gordon Anderson, and my friends, especially Ashley Gandy, Robyn Fenske, Jay Gamma, and D. Mackellar Wilkie. I would not have completed this without you. Thank you all for the constant support.

Table of Contents

List of Tables

List of Figures

Chapter 1

Introduction and Background

1.1 Introduction

In general, large diameter pipeline operators and manufacturers are challenged by increasingly stricter performance requirements from regulatory bodies, the energy industry, and public opinion due to increased interest in protecting public safety, health, and the environment. Line pipe toughness is one of the most critical mechanical properties for ensuring containment during operation of pipelines. In North America, and especially Canada, there is particular interest in toughness performance in low-temperature applications (down to -45°C). With the exception of seamless pipe used in specific applications, manufacturing line pipe generally requires forming a steel sheet or plate of the desired thickness into the a pipe of the target diameter. By necessity, a joint is required to hold the sheet or plate in the new geometry. This joint is typically made by submerged arc fusion welding (SAW) in either a longitudinal (along pipe axis) or spiral (around the pipe axis) configuration, or with electric resistance welding (ERW), a form of upset welding, in a longitudinal configuration. Contemporary ERW pipe is made from microalloyed steel sheet or plate that has been manufactured using thermo-mechanically controlled processing, a complex technology that requires careful control of manufacturing parameters through the entire process starting from the melted alloy composition, to casting and rolling, into the forming operations, and finally through the joint formation. Significant work has been done to produce microalloyed steels with exemplary toughness performance. However, ERW joint formation requires high heat inputs and significant deformation at the weld seam, which results in an area with altered structure and properties. This area is typically harder and more brittle than the original steel; the degradation in toughness is combated through the introduction of a post welding heat treatment (PWHT). According to both the American Petroleum Institute (API) [1] and the Canadian Standards Association (CSA) [2], a normalizing PWHT is required.

Contemporary ERW utilizing high-frequency (HF) alternating current, is an attractive technology for manufacturing linepipe as it is a high-speed continuous process that produces a narrow and controllable heat affected zone (HAZ) without requiring any consumables and can be performed in atmosphere [3]. However, while these welds are generally well characterized, the relation between microstructural characteristics and toughness performance of HF-ERW linepipe is not well understood [4]. This is partly due to the nature of the academic literature available [4]. Despite the industrial potential of this welding process, many aspects of contemporary ERW remain understudied; this can be attributed to the large amount of equipment required, the complexity of the process, and that much of the published research available comes from industry and thus withholds any information deemed proprietary. In contrast, much of ERW literature focuses on "vintage" (pre-1980) linepipe; generally this pipe was manufactured with less progressive upset welding methods (low-frequency ERW, direct current ERW, flash welding, and the beginning of HF-ERW), which had less process control, and less stringent QA/QC requirements [3,5,6]. For example, a significant initiative within the last decade by the U.S. Pipeline Hazardous Materials Safety Administration to develop guidelines for vintage ERW [7] resulted in the production and aggregation of a large amount of information, a significant portion of which focuses on weld defects and their assessment and treatment from an asset integrity management approach [5,6,8–10].

The present study appraoches HF-ERW joint weld seam toughness performance from a physical metallurgy and welding metallurgy perspective, with a specific focus on the bondline region development due to PWHT peak temperatures. It focuses on the performance of HF-ERW joints in the absence of welding defects; this is explored extensively in literature dedicated to the treatment of pipe from an asset integrity perspective [5,6,8]. Instead, toughness performance is investigated and linked to changes in phase transformations and subsequent microstructure development due to the influence of the PWHT peak temperature on local chemistry and austenite grain size. Mechanical property testing, advanced characterization techniques, physical simulations, and dilatometry analysis were used in this investigation.

1.2 Research Objectives

Objectives of this research are to:

1. Use advanced characterization techniques to investigate the bondline region of manufactured HF-ERW pipes with varying PWHT cycles and differing low-temperature toughness performance.
    (a) Identify key microstructural features.
    (b) Develop an understanding of the relationship between produced microstructure and the manufacturing PWHT based on metallurgical fundamentals.
    (c) Correlate microstructural observations to low-temperature toughness performance of the ERW X70 bondline region.
2. Using the understanding from (1b), conduct a physical simulation trial to investigate the relationship between the peak temperature used in the normalizing PWHT and low-temperature toughness performance.
3. Identify opportunities to conduct targeted further research to advance the body of knowledge involved in the manufacturing, structure, and performance of HF-ERW pipe.

1.3 Organization of the Report

This report is organized into five chapters with three appendices. Instead of a traditional approach, where results and discussion may be broken into separate chapters, results chapters (*Chapters 3 & 4*) are instead separated by content and intent, with both the results and discussion incorporated into a single narrative.

The remainder of *Chapter 1: Introduction and Background* includes relevant background from published literature. *Chapter 2: Materials and Methodology* documents the experimental approach, techniques, and equipment used during this study. This is followed by a reporting of results, and the discussion of these, for a characterization investigation into manufactured HF-ERW pipe specimens and their reported toughness performance in *Chapter 3: Investigation of Manufactured ERW Pipes.* Learnings from manufactured pipe guided a controlled physical, thermomechanical simulation used to study the influence of the PWHT peak temperature on toughness performance from the perspective of phase transformation development; results and analysis are discussed in *Chapter 4: Physical Simulation of Post-Welding Heat Treatments.* The final chapter, *Summary and Future Work*, provides a summary of this study as well as identified opportunities for additional work. The appendices provide additional details on tested specimens and methodologies discussed in this report, and are referred to where appropriate in the body of the work. A bibliography of cited supporting publications is provided at the end.

1.4 Background

1.4.1 Manufacture of High Frequency Electric Resistance Pipe

High-frequency electric resistance welding (HF-ERW) is an automated, autogenous welding process [3]. It operates on the principle of Joule heating, where electrical current passes through the material, causing high temperatures to be reached [3]. A variation on HF-ERW uses induction to heat the faying surfaces [3]. Both methods use high frequency current due to the principles of heat conduction and two important physical properties of high frequency current: the “skin effect” & the “proximity effect” [3].

- Skin effect: the higher the frequency, the more restricted the current flow path is to the surface of the conductor [3].
- Proximity effect: the higher the frequency, the more restricted the current path in the workpiece is to the proximity of the current return path [3].

Thus, the higher the frequency, the shallower and narrower the current path [3]. This restricts the area of heat generation and subsequently confines the heat-affected zone (HAZ) to a relatively narrow area, affecting less material [3]. Historically, low-frequency current was used, but the advantages of high-frequency current have caused this to become obsolete [3].

The two faying surfaces are heated to melting, then a high degree of deformation (called the “squeeze”) is applied. The squeeze causes the molten material to be extruded from the inner diameter (ID) and outer diameter (OD) surfaces of the pipe, leaving a strong metallurgical bond. The extruded material is then removed from both surfaces, usually leaving a slightly thinner pipe wall at the weld itself. As there is no fusion zone due to the extrusion of molten material, this is considered a solid-state weld [3]. This weld typically has an “hour-glass” shape due to the current distribution and heat conduction.

As welding is conducted in atmosphere, slight de-carburization usually occurs at the interfaces during heating, resulting in a bondline that is depleted of carbon. Due to restriction of the heated area during welding, the rest of the pipe acts a heat sink, causing relatively high cooling rates. This combination of high deformation, compositional variation, & rapid cooling usually results in undesirable weld performance. This weld is usually relatively brittle and vulnerable to crack initiation and propagation, which can lead to catastrophic weld seam failures. In order to prevent this from occurring, a post-welding heat treatment (PWHT) to return the weld mechanical properties to that of the original base material, is required; this is termed a “normalizing” heat treatment, and requires the material to be heated to full austenitization [1,2]. Here again, high-frequency current is employed in order to restrict the heat treatment to the weld to minimize the adversely affected base material. High-frequency induction from the OD surface is used to apply the PWHT; depending on manufacturing line setup and line speed, more than one normalizing furnace may be employed in series to ensure sufficient heating occurs. As the heating occurs from the OD side a heating profile may develop from the OD side to the ID side, usually in a semi-elliptical shape, which must penetrate to the ID surface and fully cover the welding HAZ.

Due to the autogeneous nature of this welding process, the weld seam is extremely sensitive to the entire manufacturing history of the base material, starting from the casting of the slabs, through the rolling operations, and finally the forming operations prior to welding. Base material composition, microstructure, thickness, the quality of skelp edges, the fit-up geometry, and the PWHT cycle can all influence the final weld quality. Beyond ensuring that weld defects do not develop, the process must be tailored to develop the appropriate metallurgical features for the desired performance.

1.4.2 Selected Defects

While defects are not a focus of this study, ERW weld seam defects are detrimental to toughness and must be eliminated as contributors before a viable study of other influencing factors can be undertaken. Three defects are specifically of interest in this study. While overlapping terminology can cause some confusion regarding these defects throughout the industry, the terminology below will be used in this work.

- Hook cracks - Banded structures, such as stringers of oxides or sulfides developed during rolling can create and area vulnerable to crack propagation [5, 6]. When this occurs near the skelp edges and the welding upset is applied, these stringers can turn from parallel to the rolling direction to parallel to the bondline at the weld seam [5, 6]. Cracking that propogates along these features is a “hook crack”, so-called due to the curved crack that develops [5, 6].

- Cold welds and penetrators - Cold welds and penetrators are very similar as both refer to areas where the solid-state bondline is incomplete [5, 6]. This occurs when the heat input and squeeze are improperly balanced during welding [5, 6]. Either heat input is too high and the squeeze is too low resulting in entrapment of a high melting temperature oxide formed from un-extruded molten metal, or if the heat input is too low or the weld upset it too low a lack of fusion will occur [5, 6]. Usually a cold weld has longitudinal axial continuity and a penetrator refers to a short section that penetrates almost through the entire thickness of the weld [5, 6].

- “White line” - White line is a decarburized region due to diffusion of carbon and alloying elements into the molten metal before expulsion. When etched, it forms a lighter line due to the alloy-depleted steel forming a band of ferrite [11].

1.4.3 Toughness

In general, toughness refers to the materials resistance to fracture, or how much energy is required to overcome bonds in the material [12]. Fracture usually occurs through either ductile propagation, cleavage, or a mixture of these two modes [12]. Generally speaking, ductile fracture is a high-toughness fracture mode and occurs at higher temperatures in body centered cubic materials like ferritic steels [12]. Ductile fracture generally occurs through through plastic deformation causing void formation, growth, and coalescence [12]. At low temperatures, the fracture mode shifts to a cleavage fracture, which generally requires less energy and is where the material is considered to have low toughness [12]. Cleavage fracture occurs when stress intensity exceeds the fracture stress before yielding occurs [12]. Either the crack will propagate transgranularly along {100} crystallographic planes or intergranularly along grain boundaries when impurities have reduced the grain boundary cohesion [12]. Microalloyed steels generally have a transition region of 50-100 °C, where a mixture of these modes is present [12]. Usually the middle of this transition region is called the ductile-to-brittle transition temperature (DBTT) or fracture appearance transition temperature (FATT), depending on the method of determination [12]. Hence, one of the concerns with low-temperature applications is being in the cleavage fracture mode regime, known as the lower-shelf energy, where toughness is low below the DBTT. Toughness can be drastically different between the upper-shelf energy (ductile, high toughness regime) and the lower-shelf energy. Conventionally, all attempts are made to avoid the cleavage fracture method in engineering steels.

One of the most common methods of measuring toughness is the Charpy V-notch impact test [13]. This test uses a swinging pendulum of known energy to break a notched specimen of fixed geometry at a fixed temperature [13]. This test is intended to test the materials toughness under rigourous conditions; a triaxial stress state with a high strain rate [12]. The absorbed energy is taken as a measure of the resistance of the material to crack initiation and propagation [13]. This test is widely used in the industry as it has several advantages. It is relatively simple to use, easy to interpret, requires minimal equipment, is comparatively simple to train operators, and is is relatively quick. However, it is not the most useful toughness metric, and repeatability is somewhat suspect, especially with ERW pipe where the notch placement is critical. The distance of the notch from the bondline can have a drastic influence on the measured toughness; the lowest toughness that is practicably measurable is within ± 0.5 mm of the bondline [14]. A discussion of toughness methodologies can best be found elsewhere as fracture mechanics is a specialized discipline of its own.

1.4.4 Metallurgical Factors Influencing Toughness

Toughness is influenced by both the design of components (stress distribution from geometry and service conditions) as well as the the toughness of the material itself. This study will only consider the metallurgical considerations influencing toughness, not the design aspect. Metallurgical factors that influence the toughness of microalloyed steels are detailed below.

Microstructure

Microalloyed steels can produce different microstructures depending on their processing history. There is some debate over what may be the best microstructure for optimizing toughness. Some research into X60-X80 grade pipes has reported that a low carbon, fine-grained bainite resulted in the best performance, especially in low-temperature applications [15–18]. Others report that minimizing the bainite fraction and ensuring a predominantly acicular ferrite structure through controlled PWHT [19] or through the addition of Al, Ti, and Mn to increase oxide inclusions, and reducing the heat input during PWHT is more desirable [20].

Grain boundaries and grain size

Grain boundaries are the interface between adjacent planes with some angle of misorientation, consisting of dislocations to allow for the mismatch between adjacent planes [21]. During cleavage fracture, grain boundaries can act as sites of energy absorption, with high angle grain boundaries (HAGBs) requiring more energy for dislocation motion to circumvent than low angle grain boundaries (LAGBs) [21]. An increase in grain boundaries will increase resistance to cleavage fracture, with HAGBs being more effective than LAGBs. Grain size is typically measured on the basis of HAGBs; thus a refined grain size is proportionate to an increased area density of HAGBs [21]. A decreased grain size will result in both a lowered transition temperature as well as an increased energy requirement to cause cleavage fracture [12, 21, 22].

Crystallographic texture

Yan *et al.* found that X65 HF induction welded pipe had "crystallographically coarse" microstructure as a contributing factor to low toughness in the weld seam [4]. This crystallographically coarse microstructure occurs when several adjacent grains with similar crystallographic orientations are clustered together [4]. These grains are separated by lower angle misorientations, providing less of an energy barrier to resist cleavage fracture. As well, appreciable texture consisting of planes orientated within 10° of $\{100\}$ (i.e. family of (100) planes) parallel to the crack propagation direction were found, which would have lowered toughness as the $\{100\}$ planes are already preferentially orientated for cleavage fracture [4].

Inclusions, precipitates, and secondary phases

Generally, in microalloyed steels, inclusions, precipitates, and small retained secondary phases are detrimental to toughness performance in both cleavage and ductile fracture modes [12, 22]. In cleavage cracking, brittle particles or small regions ahead of the crack tip will fracture, forming micro-cracks that will then propagate throughout the rest of the material [12, 22]. These particles or phases also act as sites for void nucleation in ductile fracture modes [12, 22]. The detrimental effects can be minimized through controlling their size, shape, and distribution: finer particles, spherical rather than elongated morphologies, and having particles distributed intragranularly rather than segregated to grain boundaries are better for toughness performance [22].

1.4.5 Microstructure Development

Descriptions of microstructures in ferrous metallurgy suffer from the non-standardized usage of terminology and the misuse of or differences in opinion regarding the different classifications. For this reason, there are usually descriptive subtleties which complicate the understanding of microstructural development. Descriptors of morphology, equilibrium and metastable phases present, grain sizes, and distribution are usually all necessary to ensure a complete description of the observed microstructure. This is further complicated as it is unusual to only observe a single constituent in a microstructure; typically several components co-exist, but one may dominate. In this work, we will concern ourselves with the ferrous microstructures that develop from the austenite-to-ferrite transformation.

Diffusional Transformations

Diffusional transformations are those in which the nucleation and growth of structures is driven by the diffusion of elements, especially carbon [23, 24]. These include allotriomorphic ferrite, where the ferrite structure does not reflect the internal crystalline structure, which typically forms along grain boundaries and is sometimes termed grain boundary ferrite [23–25]. In contrast, the grain interior can be host to ferritic idiomorphs, where a faceted structure reflects the crystalline structure; typical descriptions include polygonal ferrite. Equiaxed ferrite refers to either allotriomorphic of idiomorphic ferrite as it is merely a descriptor of the aspect ratio, although it is generally applied to allotriomorphic ferrite that grows into grains as well as along austenite grain boundaries [23]. These ferritic structures are usually low carbon, low alloy, and occur under slower cooling rates where solute atoms are rejected along the growth front into the remaining austenite during transformation [23–25]. At slightly higher cooling rates, a side-plate structure termed Widmanstatten ferrite can form due to a change in the growth front kinetics which favour directional growth [23–25]. Widmanstatten ferrite will reject interstitial solute atoms such as carbon to the sides instead of the growth front (less distance to diffuse), but substitutional solute atoms are retained [25]. Allotriomorphic ferrite forms at the highest temperatures, and Widmanstatten ferrite at the lowest. Generally these microstructures are softer due to the lower carbon and alloy content. If sufficient carbon is present, this diffusion will create a lamellar eutectoid of low-carbon ferrite and high carbon cementite, called pearlite [23]. This creates a layered structure of high and low hardness regions. While beneficial for strength, pearlite is generally detrimental to ductility and toughness [23].

Invariant Plane Strain Transformations

Invariant plane strain transformations (or displacive transformations) are those where cooling happens rapidly, resulting in insufficient time for diffusion to accommodate the rejection of solute elements that occurs as austenite transforms to ferrite [24,26]. Instead, a shearing reaction occurs as the crystal lattice distorts itself in order to accommodate the solute atoms [24,26]. In steels, this typically means a transition from face centered cubic (austenite) to a body centered tetragonal crystal lattice rather than the body centered cubic typically associated with ferritic structures [24, 26]. Termed martensite, this shear transformation propagates rapidly through the steel. This results in a higher alloy, higher carbon structure which is typically harder and more brittle [24,26]. This structure is also associated with high strain levels due to the shear necessary to accommodate the solute atoms [24, 26]. Martensite is the lowest temperature reaction to occur in ferrous alloys.

Mixed Transformations

Other microstructures that commonly occur in microalloyed steels are produced by mechanisms where both invariant plane strain and diffusion play a role, at temperatures between the diffusional ferrite transformations and the complete shear martensite reaction [24, 27, 28]. At slower cooling rates and lower alloying compositions, acicular ferrite forms [24, 25, 28]; acicular ferrite develops when the transformation reaction can occur faster by nucleating new ferrite grains rather than by diffusional growth [25]. This requires sufficient nucleation sites to exist within the grains, which are typically non-metallic inclusions and precipitates [24,25,28–30]. Acicular ferrite is usually thin, lenticular plates that appear as chaotic, “needle-like” fine grains in two dimensions [25, 28]. This fine-grained chaotic microstructure results in desirable mechanical properties, with a good balance between both high strength and superior toughness [25, 28]. Acicular ferrite forms by a shear transformation into supersaturated ferrite grains followed by the rejection of excess carbon into remaining austenite by diffusion [28]. Due to the shear reaction, larger substitutional atoms are unable to diffuse and are retained in the ferrite [28].

Bainite generally occurs at faster cooling rates and higher alloying compositions than acicular ferrite [25], and has a larger invariant plane strain component than acicular ferrite [24, 27]. However, these two microstructures can both occur under the same conditions; in this case, a major factor in whether bainite or acicular ferrite is the dominant transformation is the presence of sufficient nucleation sites for acicular ferrite [24, 29, 30]. Bainite is not dependent on intragranular nucleation sites as it nucleates and grows from austenite grain boundaries [25, 27]. Bainite is characterized by the coexistence of ferrite lathes and cementite films or precipitates [24, 27]. Upper bainite (high temperature bainite) occurs through the growth of ferrite plates which reject carbon and introduce dislocations to the surrounding austenite [24, 27]. Cementite or carbides then precipitate from this enriched austenite between the ferrite plates [24, 27]. Lower bainite (low temperature bainite) occurs similarly, but with very fine carbide precipitation within the supersaturated ferrite grains as well [24, 27]. The fine precipitates in lower bainite result in lower bainite being both stronger and tougher than upper bainite [27].

Martensite-Austenite

Due to the rejection of alloying elements, especially carbon, during austenite-to-ferrite transformations the final areas of asutenite can be quite enriched with solute elements. These areas may partially transform to martensite with a fraction being retained austenite. It is difficult to resolve the two without transmission electron microscopy so these areas are generally referred to as martensite-austenite (M-A) constituents. These constituents are typically hard and brittle, and can have both elongated and more equiaxed morphologies depending on processing. Generally these are considered undesirable for toughness performance in microalloyed steels [31, 32]; although some work has suggested that the presence of M-A can be beneficial to energy values at room temperature, at low temperature M-A acts as a crack initiation site [33]. A common method to improve toughness is to reduce the fraction and size of M-A constituents [31, 32].

1.4.6 Electron Backscatter Diffraction

Electron backscatter diffraction (EBSD) is an advanced characterization technique that can provide a great deal of information on the structure, crystal orientation, and phases of crystalline materials. Post-processing of collected data can provide additional misorientation information, such as misorientation associated with grain boundaries and material strain. In order to effectively resolve microstructure level information, the probe size must by necessity be smaller than the microstructural features that are under investigation [34]. Due to the use of electrons as the exploring radiation, nanometer resolution is possible using EBSD [34]. This technique uses a scanning electron microscope (SEM) with a flat sample held on a tilt, usually at a 70° angle from horizontal, and a specialized detector [34]. Automated EBSD can be used to create maps of the selected areas based on the information of interest, known as phase mapping, orientation mapping (crystal orientation imaging), etc, which makes a degree of quantification possible. [34]. The electron beam is rastered over the surface of the sample; electrons enter the sample, and a portion are backscattered due to interactions with the materials atoms [34]. As these electrons exit, a portion exit at angles meeting the Bragg condition of the lattice spacing of the crystalline structure of the material [34]. These electrons form Kikuchi bands once detected. Since the geometry of the system is known, comparison to known standards of Kikuchi bands allow for the calculation of the phase and crystallographic orientation of the material [34]. This information can all be computed concurrently, reducing instrument time.

While powerful, this technique is limited to surface material that is within the interaction volume. It is also highly sensitive to surface preparation; metallographic samples are usually analyzed in the as-polished or only lightly etched condition as topography is exacerbated by the tilt of the sample and can prevent the electron beam from interacting with the sample surface effectively.

Additional details for strain analysis

Strain analysis is mainly conducted during post-processing operations (with the exception of the image quality metric), and is effectively limited to qualitative to semi-quantitative indicators of strain rather than the extrapolation of absolute values to describe the strain condition [35]. Strain analysis is extremely sensitive to surface condition and sample preparation; it is important to prepare all specimens similarly so that any introduced strain is constant across all specimens [35]. However, EBSD is capable of identifying relatively high strain areas in the material [35], which can be quite insightful into material and transformation behaviour. Residual strain from dislocations can be measured by local variations in lattice orientation within the material [35].

Image Quality Approach

At each point of the scan, a quality metric is assigned to quantify the quality of the diffraction pattern that was detected [35]. As strain will degrade pattern quality, mapping these metrics provides a method for visualizing strain in the selected area [35]. However, there are other factors that influence pattern quality such as grain boundaries, sample preparation, surface topography, additional phases, and instrument conditions and settings [35]. As well, crystallographic orientation can have minor influence on pattern quality. For these reasons, while image quality can be used as an indicator of strain, it must be compared to other contributing factors and not taken solely as a measure of the strain [35].

Local Misorientation Approach - Grain Average Misorientation

Grain average misorientation (GAM) is a method which measures the average misorientation between points *within a grain* [35]. This approach is sensitive to the step size used, the critical tolerance angle selected, and grain size [35].

Local Misorientation Approach - Kernel Average Misorientation

Kernel Average Misorientation (KAM) is similar to GAM, but instead of a grain, a “kernel” of a size of a certain number of pixels is used. Residual strain from dislocations can be measured by local variations in lattice orientation within the material [35]. This results in a more local visualization of strain as values are assigned on a pixel-by-pixel basis, rather than averaged over an entire grain as is the case when GAM is used. Residual strain from dislocations can be measured by local variations in lattice orientation within the material [35]. This approach is sensitive to the step size used, the critical maximum angle selected for display (mainly to exclude grain boundaries), and kernel size and shape selected [35].

Chapter 2

Materials and Methodology

2.1 Approach

This study was undertaken using a two-stage approach. In stage one, an investigative and comparative methodology, adapted from failure analysis and metallurgical product performance investigations, was used to investigate specimens provided from pipe manufacterers. This consisted of the collection of available process and material data from the manufacterer, the application of both widely used and specialized characterization techniques, and collection of mechanical property information from both the manufacturer's quality assurance/quality control (QA/QC) operations and from tests conducted in-house. Due to limited sample availability, information access and logistical considerations, independent verification of provided data was not always possible nor practicable.

In stage two, learnings from stage one were leveraged to conduct a trial investigating the effect of PWHT peak temperature on low-temperature toughness performance. This was necessary to have a controlled specimens to be used for toughness testing, since PHWT 1 and PWHT 2 are nominal processes used by the manufacturer. Discussions with subject matter experts employed by the manufacturer throughout this study have indicated that there is significant variation in the ERW production process parameters, which can result in variation in the finished product. This variation, while known, is not documented in such a fashion to be correlated to any particular production run. Thus, it was necessary to acquire samples where it was possible to eliminate or minimize the influence of factors other than PWHT cycle that may affect the pipe. A study of PWHT peak temperature was selected due to known difference between the nominal PWHT 1 and PWHT 2, and the lack of sufficient available information regarding other manufacturing parameters. These other factors include:

- chemical composition
- pipe diameter
- wall thickness
- applied squeeze during welding
- welding temperature
- production line speed and ERW production line equipment setup
    - cooling rate and cooled temperature after welding
    - PWHT cycle
    - cooling rate
- thermomechanical controlled processing during the production of skelp
    - rolling schedule
    - thickness of skelp (wall thickness of pipe)
    - width of skelp (affects the effectiveness of the squeezing during welding)
    - skelp edge condition and geometry
- variations in equipment positioning and geometry

2.2 Materials

Table 2.1 summarizes the materials used in both stages of this study, where carbon equivalent (CE_{Pcm}) is calculated using Eq. 2.1 [1] from chemical composition reported by the manufacturer (shown in Table 2.2); values shown are the average of the provided heats. Fig. 2.1 shows schematics of PWHT cycles 1 and 2 from the manufacturer and the PWHT cycle for the peak temperature study. It was assumed that the target temperature of each of normalizing stage is reached at the end of the normalizer; time intervals were calculated based on a representative line speed obtained from the manufacturer. A constant cooling rate was used for the peak temperature study to eliminate the influence of changing cooling rates.

Table 2.1: Summary of materials used. (Restricted for proprietary reasons.)

Specimen ID (PWHT-Toughness, *PWHT-Peak Temp.)	Production	Diameter, *in.(mm)*	Wall Thickness, *in.(mm)*	PWHT Parameters	CE_{Pcm}
1-L	Manufactured Pipe	24 (610)	0.406 (10.3)	Three-stage normalizing $\sim A_{c1}\| > A_{c3}\| >>> A_{c3}$	0.167
1-H	Manufactured Pipe	24 (610)	0.5 (12.7)	Three-stage normalizing $\sim A_{c1}\| > A_{c3}\| >>> A_{c3}$	0.156
2-H	Manufactured Pipe	16 (406)	0.281 (7.1)	Three-stage normalizing $> A_{c1}\| >> A_{c3}\| >> A_{c3}$	0.156
$^*3 - T_P$	Gleeble Simulation From as-welded pipe	24 (610)	0.353 (9.0)	Three-stage normalizing $\sim A_{c1}\| >> A_{c3}\|T_P$	0.175

$$CE_{Pcm} = C + \frac{Si}{30} + \frac{Cr + Cu + Mn}{20} + \frac{Ni}{60} + \frac{(Mo)}{15} + \frac{(V)}{10} + 5B \tag{2.1}$$

Table 2.2: Base material chemical composition reported by manufacturer. Values are an average of reported heats (wt.%). Balance is Fe. (Restricted for proprietary reasons.)

Material	C	Nb	Ti+V	Mn	Si	Cu+Ni+Cr+Mo	N (ppm)	S (ppm)	Pcm
1-L	0.043	0.068	0.025	1.650	0.180	0.672	90	20	0.167
1-H	0.040	0.070	0.023	1.580	0.170	0.622	90	20	0.156
2-H	0.035	0.075	0.028	1.653	0.167	0.644	90	10	0.156
3-T$_P$	0.052	0.074	0.02	1.620	0.140	0.760	110	60	0.175

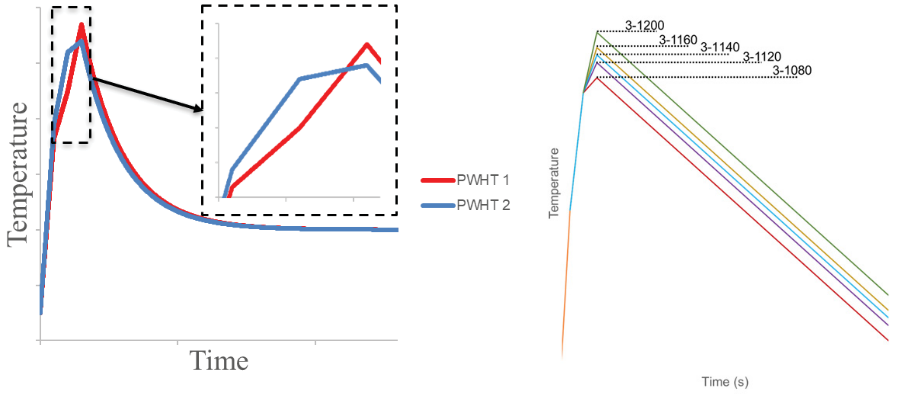

(a) (b)

Figure 2.1: (a) Schematic of manufacturer PWHT, where exact time intervals in PWHT-2 are unknown but assumed similar to PWHT-1. (b) Schematic of PWHT-3 cycle used in Gleeble PWHT T$_P$ trial.

2.3 Investigation of Manufactured Pipe Specimens

2.3.1 Microstructure and Mechanical Properties

A representative metallurgical specimen was received from the manufacturer for each of 1-L, 1-H, and 2-H. Metallurgical specimens were used for characterization analysis and hardness testing, and analysis was conducted at the approximate mid-thickness of each specimen. Table 2.3 summarizes the goals and methodologies of the investigative activities. Charpy V-Notch impact test data was also obtained from the manufacturer for analysis and comparison between 1-L, 1-H, and 2-H.

Table 2.3: Summary of investigative activities.

Objective	Experimental Technique	Anticipated Outcomes
Microstructure and Phase Observations	OM SEM EDS STEM EBSD	Identification of microstructural constituents Identification of inclusions and precipitates Grain size measurements Observations of microstructural homogeneity
Strain Determination	EBSD	Mapping of strained areas Determination of material condition Correlation of strain to toughness performance
Micro-texture Determination	EBSD	Mapping of crystallographic orientation Determination of presence of texture Correlation of texture to toughness performance
Mechanical Performance	Micro-hardness (Vickers) Charpy V-Notch Impact Test	Mechanical property homogeneity Material susceptibility to low-temperature brittle failure Toughness performance metrics

Metallograhic sample preparation

Metallographic specimens were prepared using a Buehler MetaServ 250 grinder-polisher with a Vector power head to the required finish depending on the observation technique being used. Specimens were ground with silicon carbide grinding papers then mechanically polished with a series of diamond suspensions to a 0.25 μm finish, followed by 0.05 μm alumina, and finally 0.02 μm colloidal silica where necessary. Samples were subsequently etched with a 2% nital solution (nitric acid in ethanol). Transmission scanning electron microscopy (T-SEM) required a finer finish than possible using mechanical polishing alone. After 0.02 μm colloidal silica, a Fischione Instruments 220 twinjet electropolisher was used to polish the specimen. A solution of 10% perchloric acid (70% concentration) in ethanol cooled to -50 °C and a voltage of 10-20 V was used. Required finishes & etching details are shown in Table 2.4.

Table 2.4: Metallographic specimen preparation requirements.

Technique	Minimum Finish	Etching Technique	Notes
OM	0.05 μm alumina	2% nital, swab 10-20s	
SEM w/ EDS	0.05 μm alumina	2% nital, swab 10-20s	
EBSD w/ EDS	0.02 μm colloidal silica	2% nital, swab 2-5s	After lightly etching, polish for 30s on 0.02 μm colloidal silica
T-SEM	Electropolished	10% perchloric acid (70% concentration) + 90% ethanol at -50 °C, 10-20 V, 4-5 min.	Used a twinjet electropolisher. Thinned until electron transparency was achieved.

Optical Microscopy

Optical microscopy was conducted using an Olympus BX61 microscope and the Olympus StreamMotion software.

Scanning Electron Microscopy

Scanning electron microscopy (SEM) was conducted using a Zeiss Sigma field emission scanning electron microscope (FE-SEM), using a 30μm aperture and an accelerating voltage of 20 kV. A Zeiss Gemini in-lens secondary electron (SE), SE, and backscattered electron (BSD) imaging modes were employed.

Energy Dispersive X-ray Spectroscopy

For energy dispersive X-ray spectroscopy (EDS), the previously discussed Zeiss Sigma FE-SEM was equipped with an Oxford Instruments X-Max^N 150 detector and the Oxford Instruments AZtec software version 2.4 was used for data acquisition and analysis. A 30μm aperture and an accelerating voltage of 20 kV was used.

Electron Backscatter Diffraction

For electron backscatter diffraction (EBSD), the previously discussed Zeiss Sigma FE-SEM was equipped with an Oxford Instruments NordlysNano detector and Oxford Instruments AZtec software version 2.4 for data acquisition. Data post-processing and analysis was conducted with the Oxford Instruments HKL Channel5 software. An accelerating voltage of 20 kV, a 60 μm aperture, and a tilt of 70° were employed. Orientation of EBSD observations are shown in Fig. 2.2. While metallurgical examinations were conducted on 1-L and 2-H near the beginning of the study, 1-H was added late in the study once toughness performance data was obtained. Analysis of toughness performance indicated that use of EBSD to investigate 1-H was prudent, and data was collected at this time, which resulted in slightly different acquisition step sizes due to evolving understanding of the material and changing time, personnel, and equipment resource allocations. The effect of this change on the results will be discussed in *Chapter 3*.

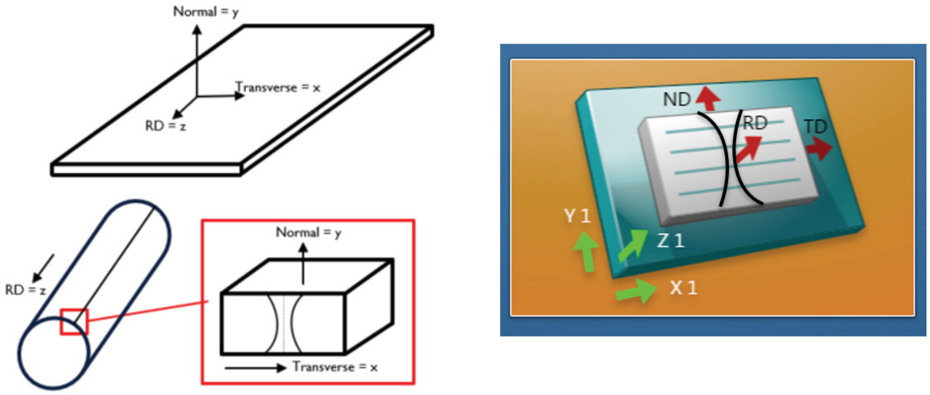

Figure 2.2: Specimen orientation in EBSD analysis.

Transmission Scanning Electron Microscopy

For transmission scanning electron microscopy (T-SEM), the Zeiss Sigma FE-SEM was equipped with an T-SEM sample holder and Zeiss EVO STEM MK2 detector. An accelerating voltage of 30 kV and a 60 μm aperture were employed.

Hardness Testing

Hardness testing was performed using a Wilson VH3100 hardness tester with Minuteman software. A Vickers hardness indenter was used with a 10s dwell time. Results are reported as HVXX, where "XX" is the load used, in kg. Statistical analysis utilizing t-test comparison of the bondline with the adjacent area was conducted with a 95% confidence interval to determine if differences were statistically significant.

Charpy V-Notch Impact Testing Data

Charpy V-notch impact testing (CVN) data was supplied the manufacturer. Data was collected as part of ongoing QA/QC procedures used to qualify product for sale and use. Testing adheres to ASTM A370 [13], as well as other relevant industrial standards and requirements [1, 2]. Physical CVN specimens were not obtained. For comparison, all energy values were approximately converted to the equivalent full size specimen values using Eq. 2.2 [1] (see ASTM A370 [13] for specimen sizing).

$$CVN_{fullsize} = \frac{Energy(J)}{sub - size} \tag{2.2}$$

where sub-size is: half size = 1/2 ; three-quarter size = 3/4; etc.

2.4 Physical Simulation of Post-Welding Heat Treatments

In the second part of this study, CVN and dilatometry specimens were created to study the effect of the peak temperature used in a representative PWHT process. In order to minimize the influence of other factors and mimic the manufacturing line PWHT as accurately as practicable, all specimens were created from a single section of pipe welded but not PWHT on the manufacturing line. A representative schematic of the sampling location is shown in Fig. 2.3. The facilities of the Research and Development division of Evraz North America at Regina, Saskatchewan, Canada were used for all specimen preparation and mechanical property testing, with the exception of characterization work.

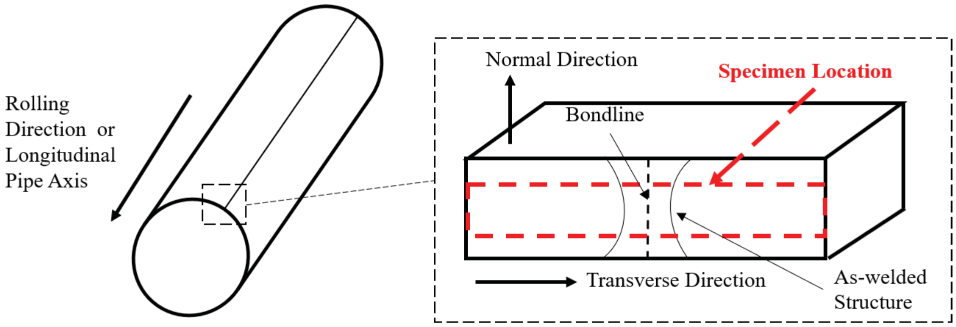

Figure 2.3: Specimen Sampling for PWHT T_P study from as-welded pipe.

Both the CVN and dilatometry specimens were PWHT-ed using a Dynamic Systems Inc. (DSI) Gleeble 3800 thermomechanical simulator. Electric resistance heating in a vacuum of approximately $4 * 10^{-1}$ torr was performed, using water cooled copper jaws and a free span of 20 mm. This produced a heat-affected zone (HAZ) sufficient in width to completely remove the as-welded structure of the welded pipe, and was similar to that observed in manufactured samples. Control thermocouples were placed on the bondline for both the CVN and dilatometry samples to ensure target temperatures were reached at the bondline.

Charpy V-Notch Impact Test Specimens

Due to the thickness of the as-welded pipe provided, CVN specimens were machined as half-size specimens (5mm x 10 mm, as per ASTM A370 [13]), with deviations from standard specimen dimensions noted in *Appendix A*; energy values obtained were converted to full size using Eq. 2.2 for comparison with manufactured pipe results. CVN specimens were then PWHT-ed using the representative PWHT 3 described in Table 2.1 and Fig. 2.1, with T_P of 1080° C, 1120° C, 1140° C, 1160° C, & 1200°C. A constant linear cooling rate of 6.4 °C/s was maintained in order to eliminate the effect of cooling rate variations; this rate was determined to be somewhat representative of a linear approximation of in-line cooling during manufacturing. After PWHT, specimens were notched at the bondline, which was determined by hand polishing the weld seam region to a 15 μm finish with silicon carbide grounding paper and subsequently macro-etching with 5% nital until the bondline was detectable. Specimens were then cooled to the test temperature using an ethanol bath and dry ice before being broken according to ASTM A370 [13] using a SATEC Systems Inc. Model SI-1K3 Charpy impact tester. Fig. 2.4 summarizes the CVN specimen preparation activity flow.

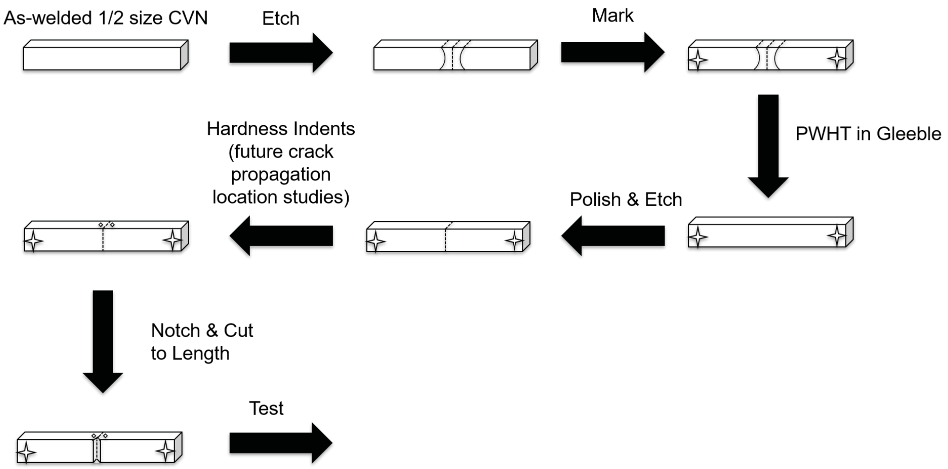

Figure 2.4: Work flow for creating PWHT T_P study CVN specimens.

Dilatometry Specimens

Dilatometry specimens were machined as round bars with a 6mm diameter, etched with 5% nital to position the thermocouples on the weld bondline, and were tested as per ASTM A1033 [36] for resistance heated specimens. However, instead of the specified thermal cycles in ASTM A1033 [36], dilatometry specimens were PWHT-ed using the representative PWHT 3 described in Table 2.1 and Fig. 2.1, with T_P of 1080 °C, 1120 °C, 1140 °C, 1160 °C, 1180 °C, & 1200 °C. Two tests at each peak temperature of 1160 °C and 1200 °C were conducted. A constant linear cooling rate of 6.4 °C/s was maintained in order to eliminate the effect of cooling rate variations; this rate was determined to be somewhat representative of a linear approximation of in-line cooling during manufacturing.

In order to investigate the effect of cooling rate, dilatometry specimens were also used to create a minimalistic continuous cooling transformation (CCT) diagram spanning the peak temperature range of interest. Specimens were PWHT-ed using the representative PWHT 3 described in Table 2.1 and Fig. 2.1, but only with selected peak temperatures of 1080 °C and 1200 °C, and controlled linear cooling rates of 3 °C/s, 5 °C/s, and

10 °C/s until 400 °C, when specimens were allowed to free cool. Specimens with the appropriate peak temperatures and cooling rates of 6.4 °C/s were also included from the T_P trial. Transformation temperatures were observed to determine the material response to cooling rate. Microstructural investigation of the CCT specimens was not completed; of greater interest was to explore if changes in cooling rate produced a response in material transformation behaviour.

Determination of Phase Transformation Behaviour

For comparison, equilibrium phase transformation start temperatures were calculated for a representative X70 pipe chemistry (see *Appendix B* for the methodology). Collected dilatometry data was analyzed to investigate the phase transformations occurring during the PWHT cycle. Dilation (more generally known as strain), was plotted versus temperature and smoothed using a Savitsky-Golay filter, which creates a polynomial with a smoothing filter that does not mask sharp points in the data [37, 38]. Transformation temperatures (A_{c1}, A_{c3}, A_{r1}, & A_{r3}) were determined by changes in slope as per ASTM A1033 [36]; the first order numerical derivative of dilation with respect to temperature was taken and plotted versus temperature in order accurately determine changes in slope correspond to phase changes, including minute changes associated with precipitates or other small volume fraction phases. Evidence of homogenization during the heating cycle of the PWHT was determined by deviations in slope above A_{c3} on the dilation versus temperature plot [39]. See *Appendix C* for details regarding determination of transformation behaviour.

Metallographic Characterization

All metallographic characterization activities were conducted as previously discussed in *2.3: Investigation of Manufactured Pipe Specimens*.

Chapter 3

Investigation of Manufactured ERW Pipes

3.1 Weld Defects

A brief survey was first conducted to ensure that in the specimens provided, the toughness performance was not being influenced by the presence of welding defects. Representative specimen macrostructures are shown in Fig. 3.1. No evidence of cracking, penetrators, stringers, or lack-of-fusion defects that would indicate poor skelp edge quality or improper squeeze and heat input balance during welding were detected in the provided representative specimens. There was also no indication of significant misalignment of the weld seam, and the area of PWHT was reasonably centered on and covered the welded structure. The HAZ of the PWHT penetrated to the ID surface of the weld seam, however was not uniform across the full thickness; discussions with representatives of the manufacturer indicated this was due to heating from the OD surface of the pipe and the penetration of the induction fields, which varied as a function of pipe thickness. It was determined that this was representative of normal operations, and was not termed a defect for the purposes of this study. While the bondline of the PWHT-1 specimens did show up as brighter than the adjacent material, this was not considered a true "white line" defect for the purposes of this study; this white line feature did not present in the as-welded specimens, but rather after PWHT. As both the 1-L and the 1-H specimens were observed to have this feature, it can be assumed the presence of this structure is not a determining factor for the toughness performance, and as such further analysis is necessary to determine the true cause of toughness performance degradation. Thus, weld defects were assumed to not be an influence in this study.

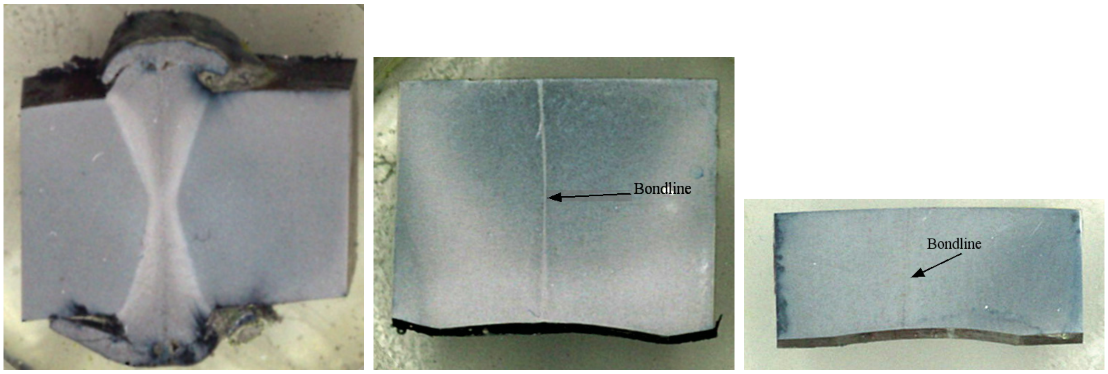

(a) As-welded, PWHT-1 **(b)** PWHT-1 **(c)** PWHT-2

Figure 3.1: Representative macrostructure of manufactured specimens.

3.2 Toughness Performance

Toughness performance of the weld seams of manufactured pipe as measured by CVN testing conducted by the manufacturer's QA/QC operations is shown in Fig. 3.2, and averages of low-temperature performance at -30° C and -45° C are shown in Table 3.1. Despite the same nominal manufacturing conditions, changeover 1-L has performed significantly worse than changeover 1-H; even at -5° C, there are a large number of tests that would not meet the target 40 J minimum criteria of this study, and no tests meet or exceed the 40 J minimum at the -45° C temperature of interest. Changeovers 1-H and 2-H performed rather similarly, with 1-H exhibiting somewhat better performance at and above -5° C, almost identical performance at -20° and -30°, and 2-H exhibiting slightly stronger performance at -45°. As well, discussions with subject matter experts employed by the manufacturer indicate that PWHT 2 usually performs better than PWHT 1 in past experience [40].

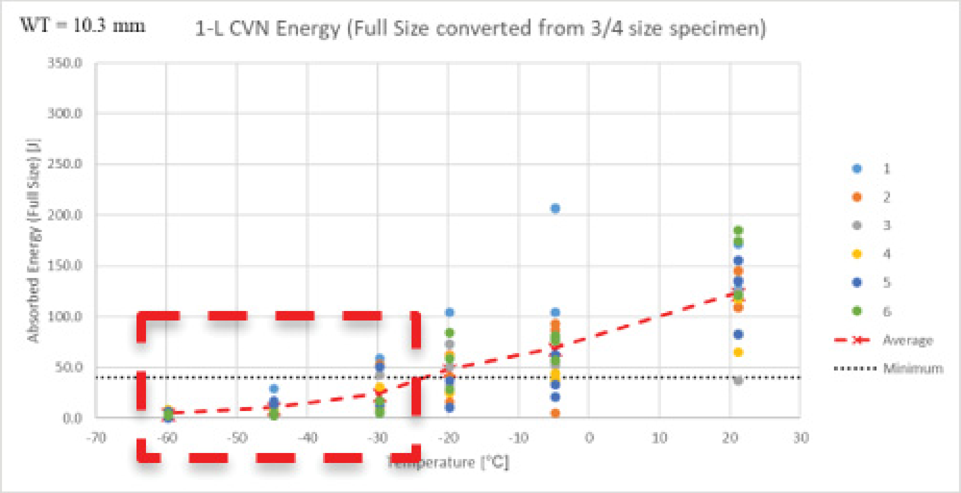

(a) CVN performance of changeover 1-L, reported from 6 pipes.

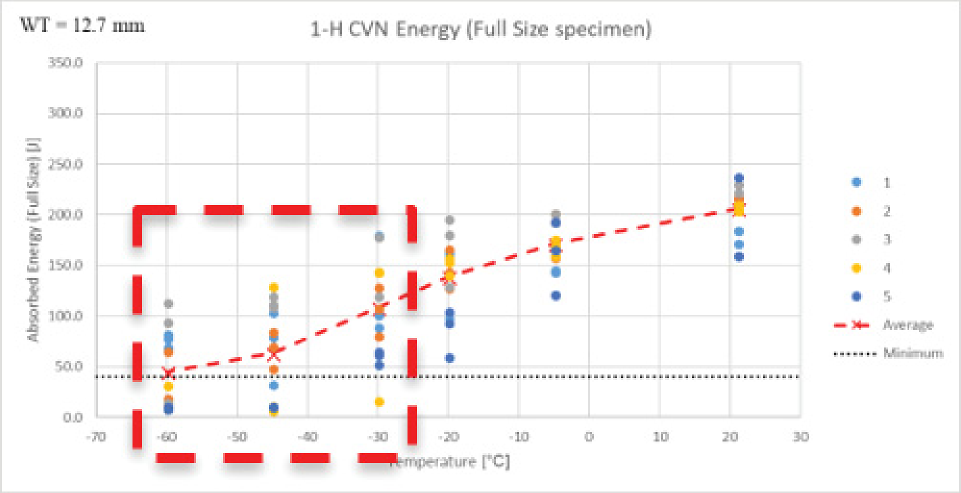

(b) CVN performance of changeover 1-H, reported from 5 pipes.

Figure 3.2: CVN results reported from manufacturer. Target minimum taken as 40 J, from CSA Z245.1-14 [41], which is more stringent than the recently published CSA Z245.1-18 [2] and API 5L-18 [1].

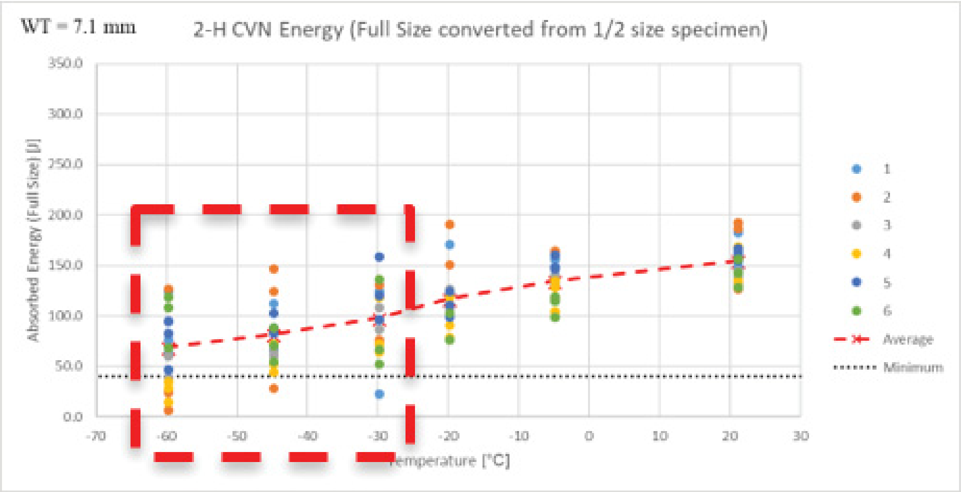

(c) CVN performance of changeover 1-H, reported from 6 pipes.

Figure 3.2: CVN results reported from manufacturer. Target minimum taken as 40 J, from CSA Z245.1-14 [41], which is more stringent than the recently published CSA Z245.1-18 [2] and API 5L-18 [1]. (cont.)

Table 3.1: Low-temperature average CVN performance of manufactured pipe.

Test Temperature (° C)	1-L	1-H	2-H
-30	24.1 ± 19.4	108.0 ± 47.0	97.6 ± 34.6
-45	10.2 ± 6.9	63.1 ± 46.1	82.1 ± 29.7

3.3 Microstructural Observations

Fig. 3.3 shows the microstructures at the bondline of the manufactured weld seams observed with optical microscopy, viewing the cross-section of the weld with the outer diameter surface (OD) of the pipe at the top, and the inner diameter (ID) surface at the bottom, taken at the mid-wall thickness. 1-L and 1-H show very similar features, with a 100-125 μm bondline composed of a very fine grained (~1-10 μm) allotriomorphic ferrite and heterogeneous, predominantly coarser grained bainite (~15-20 μm), HAZ adjacent to the bondline. The HAZ in both samples also has a small fraction of fine-grained allotriomorphic ferrite at bainitic grain boundary intersections. In contrast, 2-H shows a very homogeneous bondline and adjacent area at the weld seam, composed of fine-grained allotriomorphic ferrite. The bondline ferrite in all samples appears relatively equiaxed, although, the ferrite in 1-L may be slightly elongated along the through-thickness axis of the bondline. All three specimens have darker etching, smaller "island" phases at grain boundary intersections (and near the fine-grained ferrite in the case of the PWHT -1 specimens), however optical microscopy was able to provide little further information.

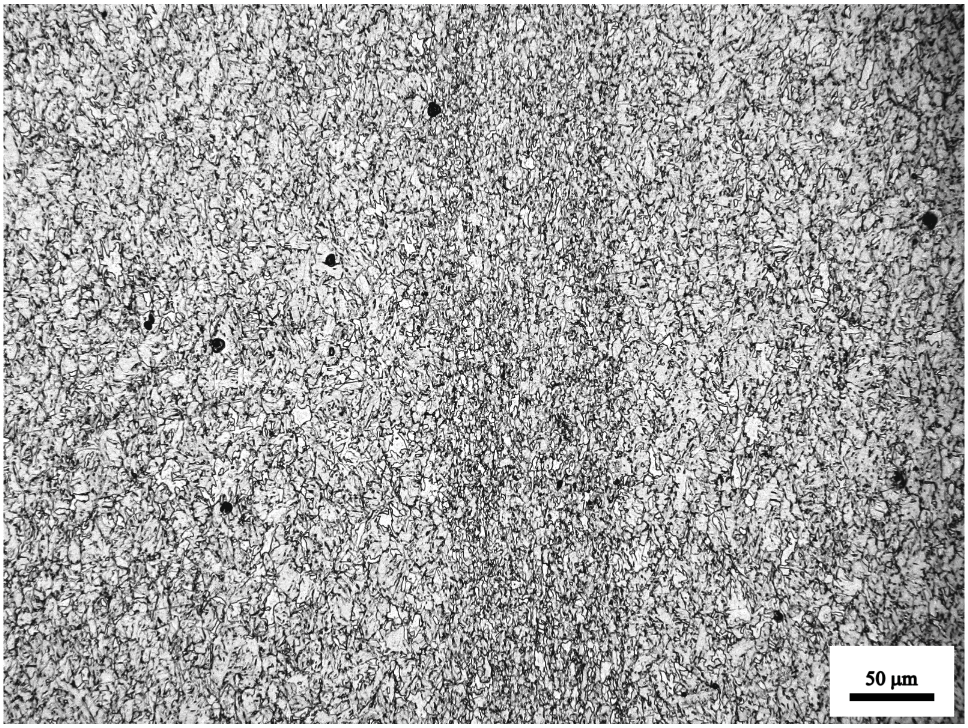

(a) 1-L.

Figure 3.3: Optical microscopy of the weld seam of manufactured specimens.

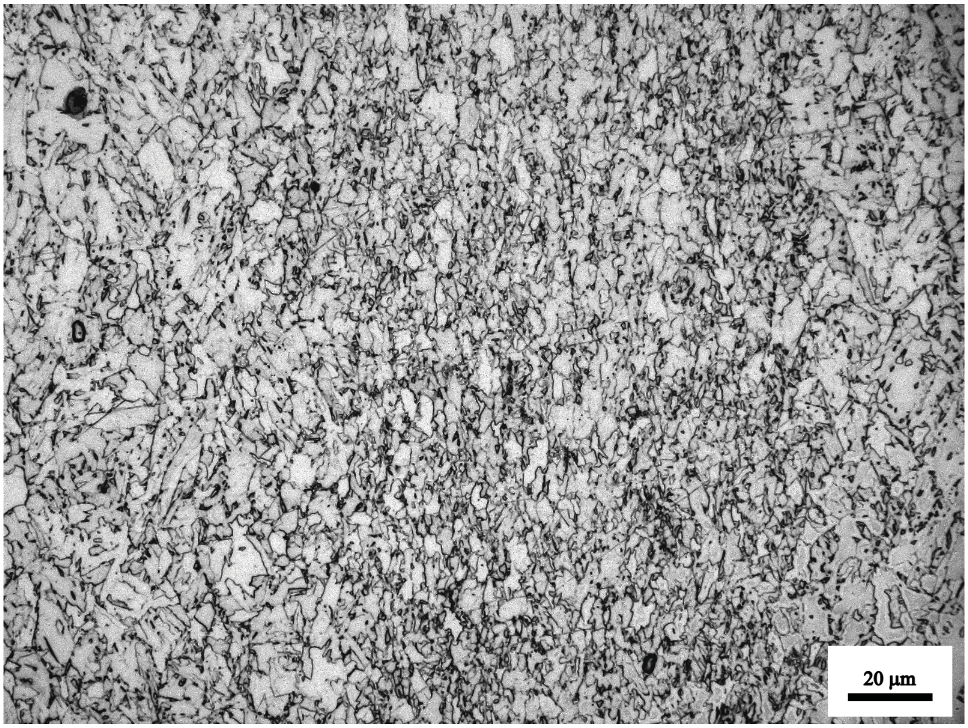

(b) 1-L, magnified.

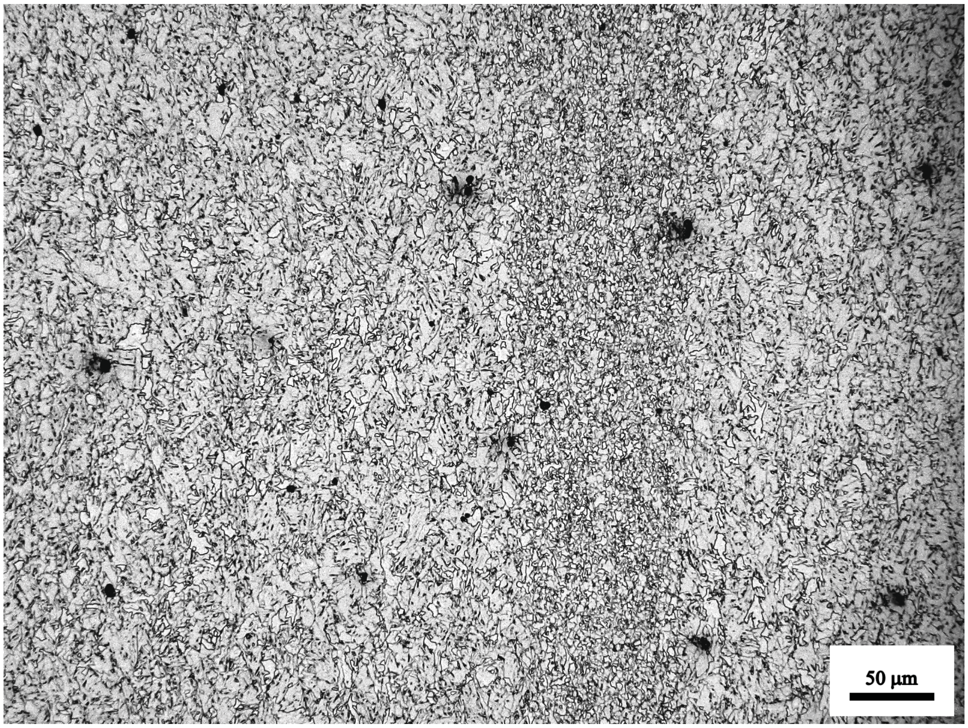

(c) 1-H.

Figure 3.3: Optical microscopy of the weld seam of manufactured specimens. (cont.)

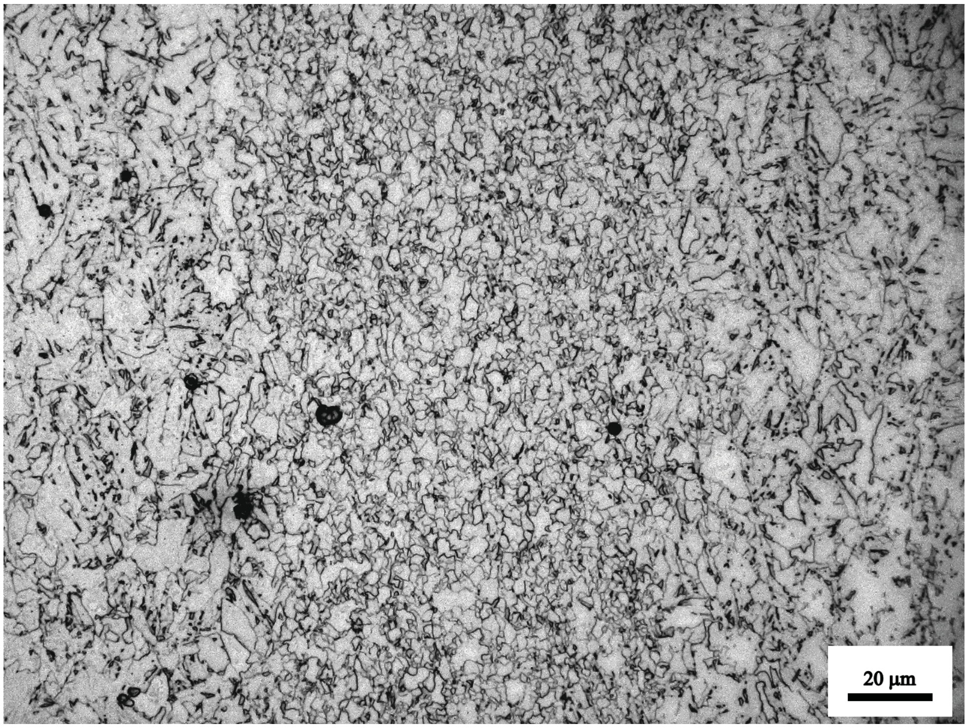

(d) 1-H, magnified.

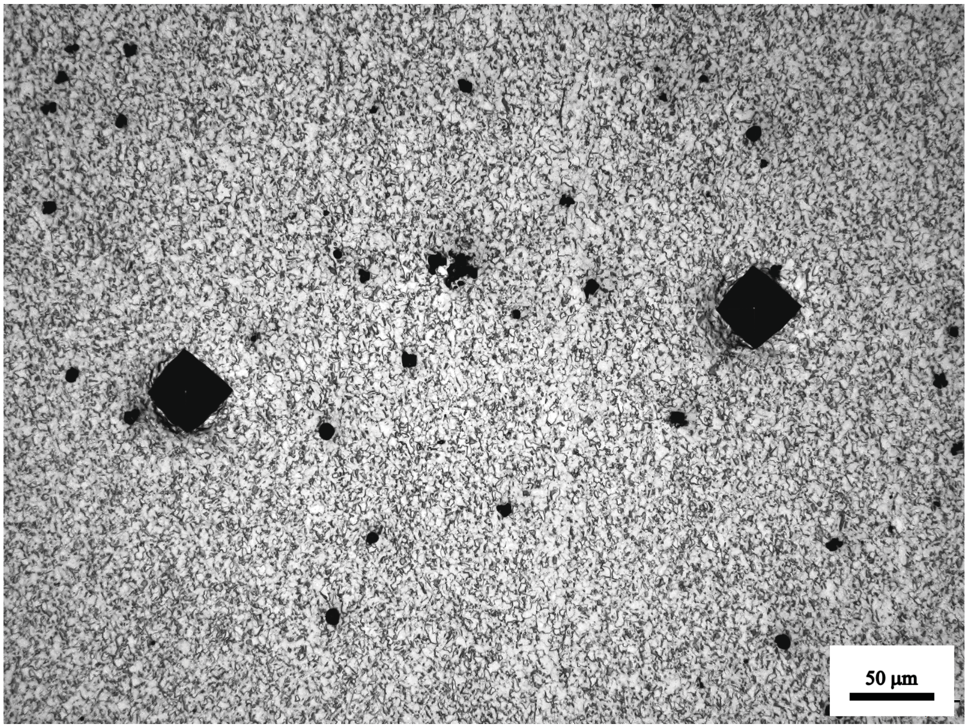

(e) 2-H.(With hardness indents for later study identification.)

Figure 3.3: Optical microscopy of the weld seam of manufactured specimens. (cont.)

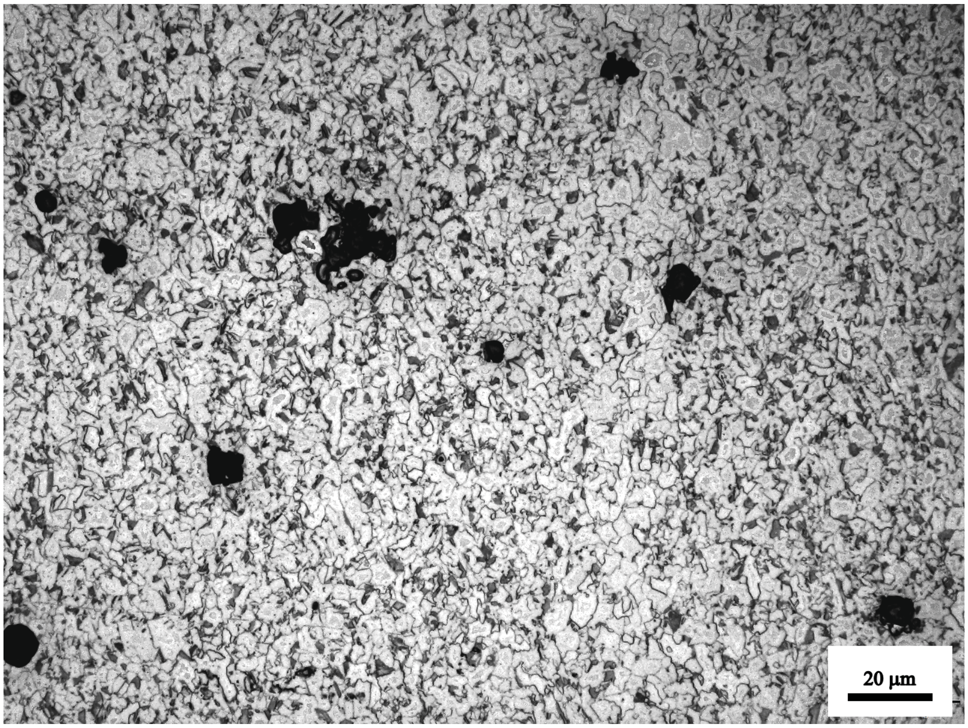

(f) 2-H, magnified.

Figure 3.3: Optical microscopy of the weld seam of manufactured specimens. (cont.)

Representative areas were further studied with SEM. Using secondary electron imaging (Fig. 3.4), the darker etching islands found in optical microscopy are shown to be topographically raised features of 1-2 μm. These features, seen in specimens from both, PWHT-1 and PWHT-2, correspond to brighter regions when observed with backscatter imaging (Fig. 3.5), indicating areas with a potentially higher concentration of heavy alloying elements. These areas are also higher in carbon, as evidenced from the EDS results in Fig. 3.6. Fig. 3.7 summarizes results from transmission-SEM, conducted on 1-L adjacent to the bondline. It was discovered that these features are also areas of higher deformation (darker in bright field imaging, indicating a high amount of dislocations). EDS conducted in tandem with the T-SEM revealed slightly elevated levels of C, as well as inconsistent observations of slightly elevated levels of Al, Cu, Mn and Si in some of the highly deformed areas. This combination of observations leads to the conclusion that there is a high likelihood that the darker etching islands in optical microscopy are likely M-A features, enriched in alloying elements and carbon, with a high dislocation density introduced during the displacive transformation to martensite. These areas would be the last to transform during the austenite-to-ferrite transformation on cooling, leading to locally enriched regions that transform to martensite or, if sufficiently enriched, stabilize the remaining austenite which is then retained.

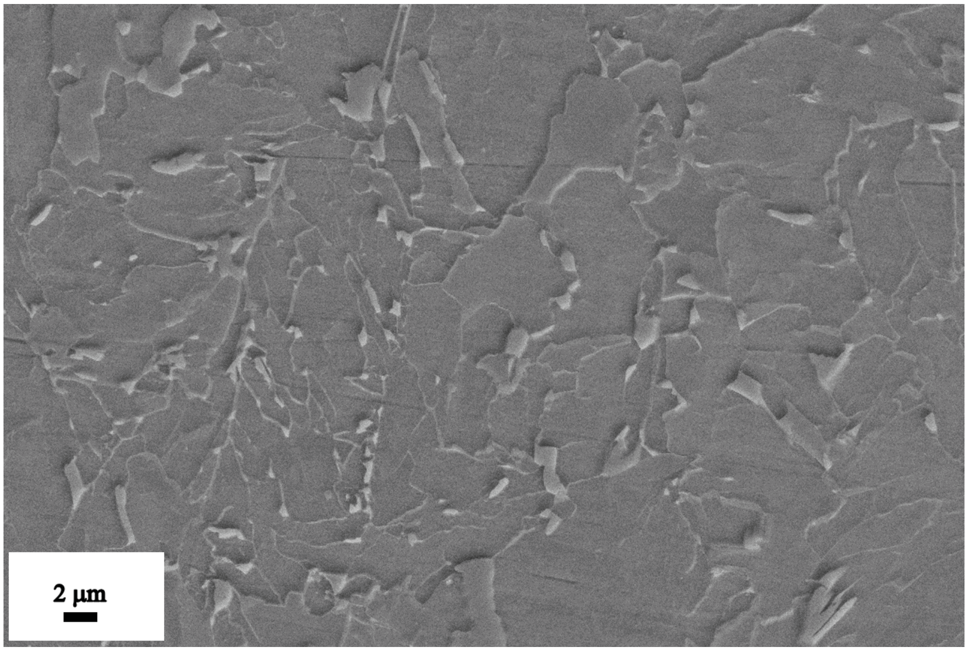

(a) 1-H adjacent to bondline.

Figure 3.4: SE observations of the weld seam of high toughness manufactured specimens.

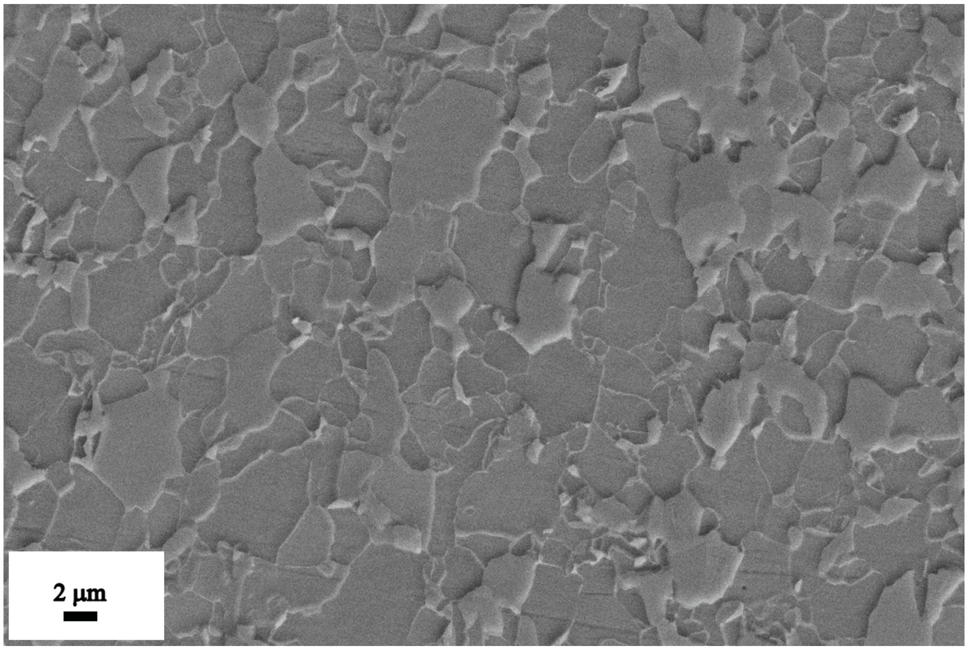

(b) 1-H bondline.

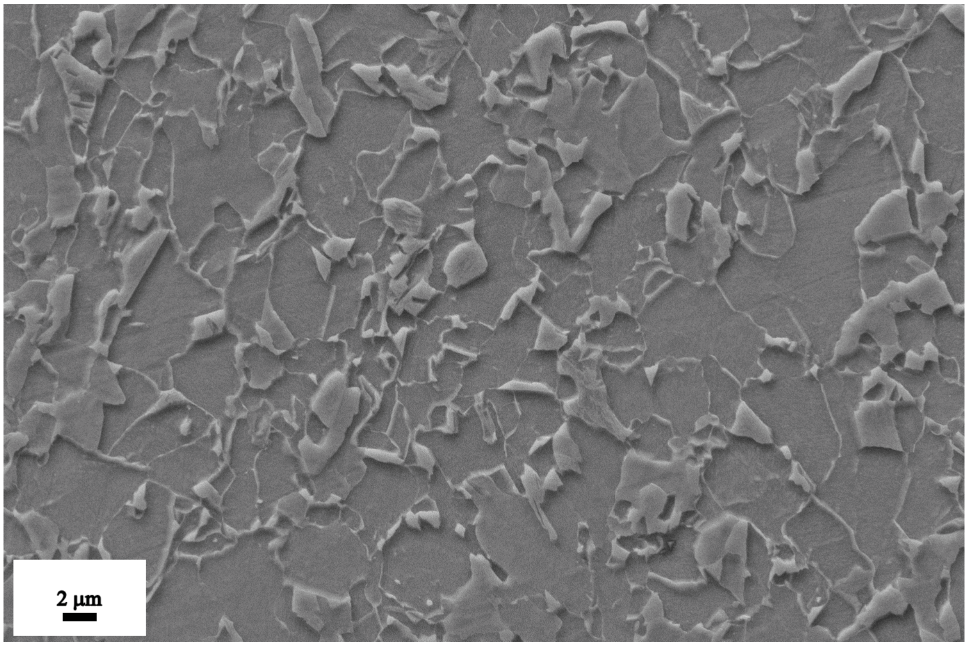

(c) 2-H, bondline.

Figure 3.4: SE observations of the weld seam of high toughness manufactured specimens. (cont)

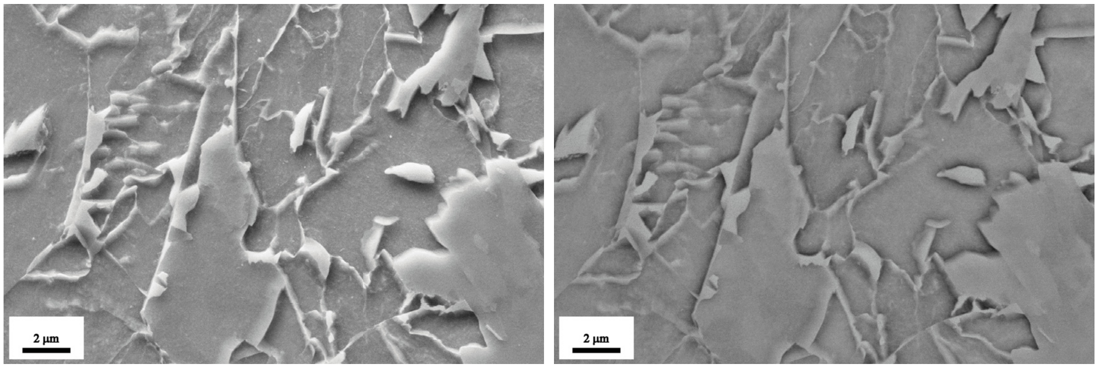

(a) 2-H, secondary electron imaging **(b)** 2-H, backscatter imaging.

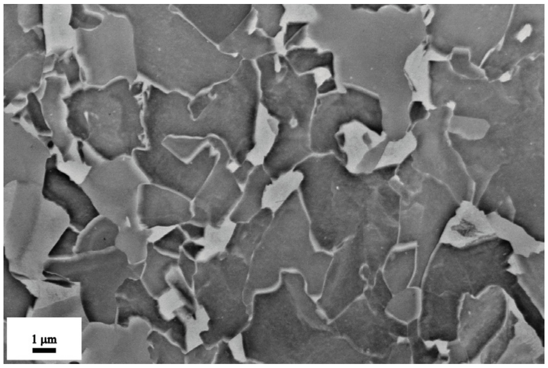

(c) 1-L, backscatter imaging.

Figure 3.5: BSD observations of the weld seam of high toughness manufactured specimens.

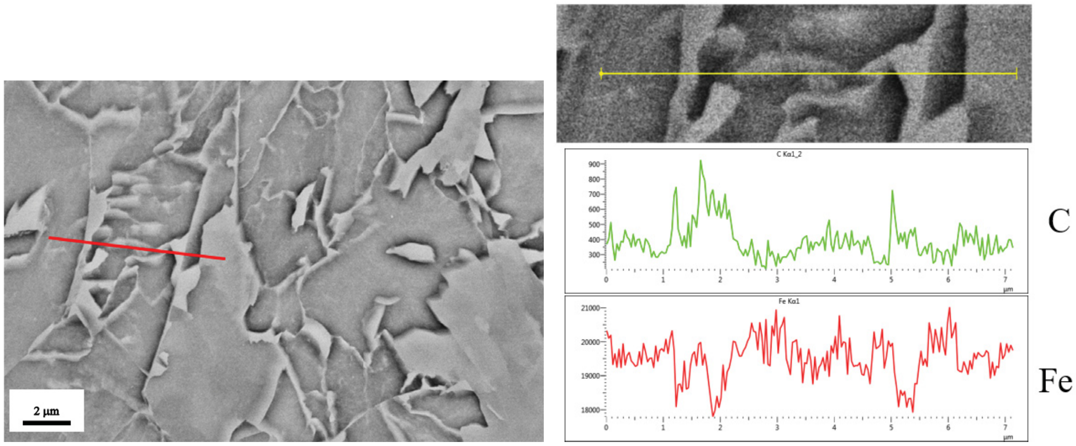

(a) 2-H, BSD, EDS line scan area. **(b)** EDS results.

Figure 3.6: EDS results showing increased carbon content in “island features”.

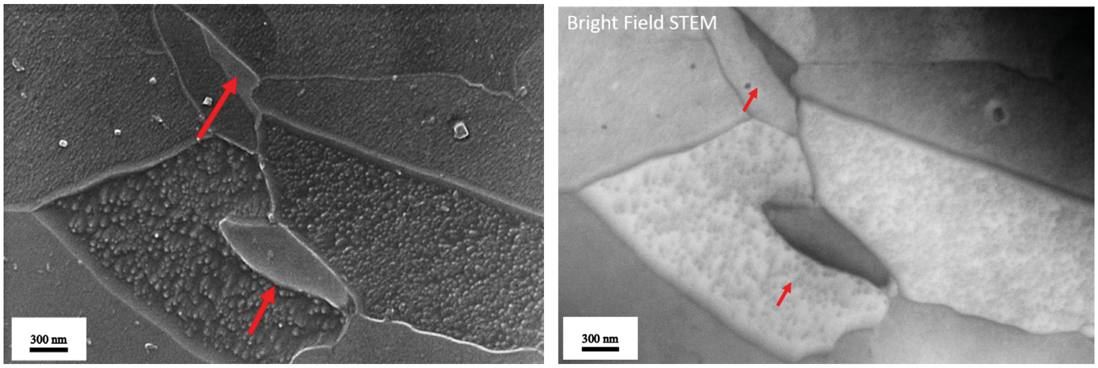

(a) SE imaging of “island” features.

(b) BF imaging of “island” features.

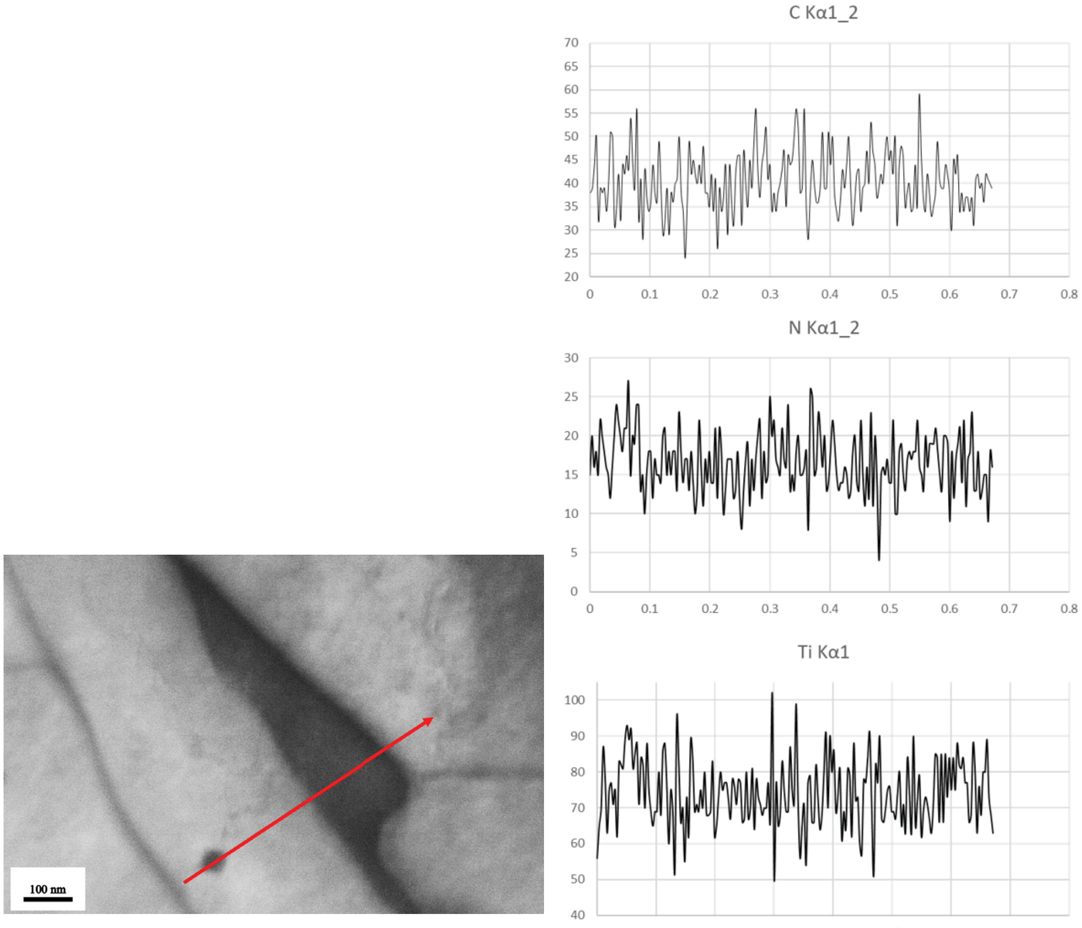

(c) EDS line scan across particle and “island” features.

(d) EDS results of line scan in (c).

Figure 3.7: T-SEM with EDS investigation of “island” phases in sample 1-L. Not shown, but similar observations to those made for Al and Cu were made for Mn and Si at other “island” features.

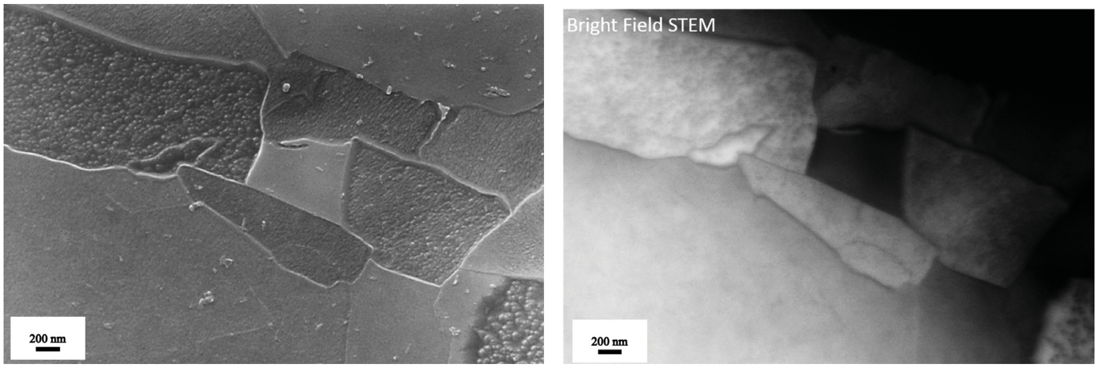

(e) Second "island" with different morphology, SE.

(f) Second "island" with different morphology, BF.

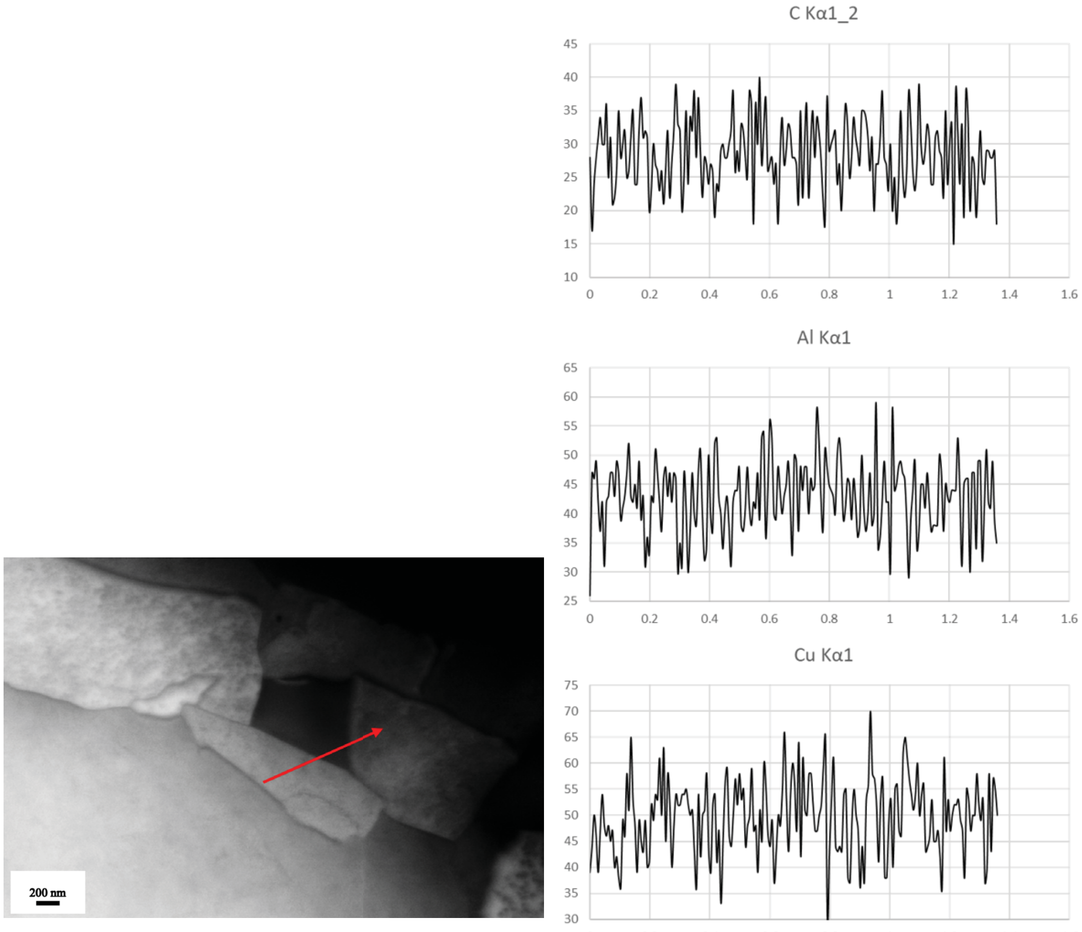

(g) EDS line scan across second "island", BF

(h) EDS results of line scan in (g).

Figure 3.7: T-SEM with EDS investigation of "island" phases in sample 1-L. Not shown, but similar observations to those made for Al and Cu were made for Mn and Si at other "island" features. (cont.)

Inclusions & Precipitates

In addition to the inclusions or precipitates visible in Fig. 3.3 as the black regions (or the holes where these were removed during polishing and etching) and the TiN precipitates identified in Fig. 3.7 (c) & (d) in 1-L, other observations of inclusions and precipitates were made. Fig. 3.8 shows representative colour optical microscopy images of 1-L and 1-H showing larger cubic particles than observed in T-SEM (gold) and round particles (grey). Identification of these particles was carried out using SEM with EDS analysis in the as-polished condition on an as-welded sample from PWHT 1, where these features were also observed, shown in Fig. 3.9. It was found that the spherical features were casting inclusions consisting of Ca, Al, Mn, Mg, S, & O, and the cubic features are Ti & Nb nitrides. Additional T-SEM on 1-L in Fig. 3.10 further confirms that the cubic features observed are mainly consist of TiN. These particles were also in the as-polished condition of 1-L, 1-H & 2-H, but are not shown in the interest of brevity. Since the inclusions and precipitates present in the material are determined by processing prior to the PWHT (casting, rolling, welding, etc.), and little information was available regarding the prior condition of the material, it was determined to be out of the scope of this study; only a cursory identification was conducted to confirm that they were indeed the expected precipitates and inclusions for microalloyed steels of this chemical composition.

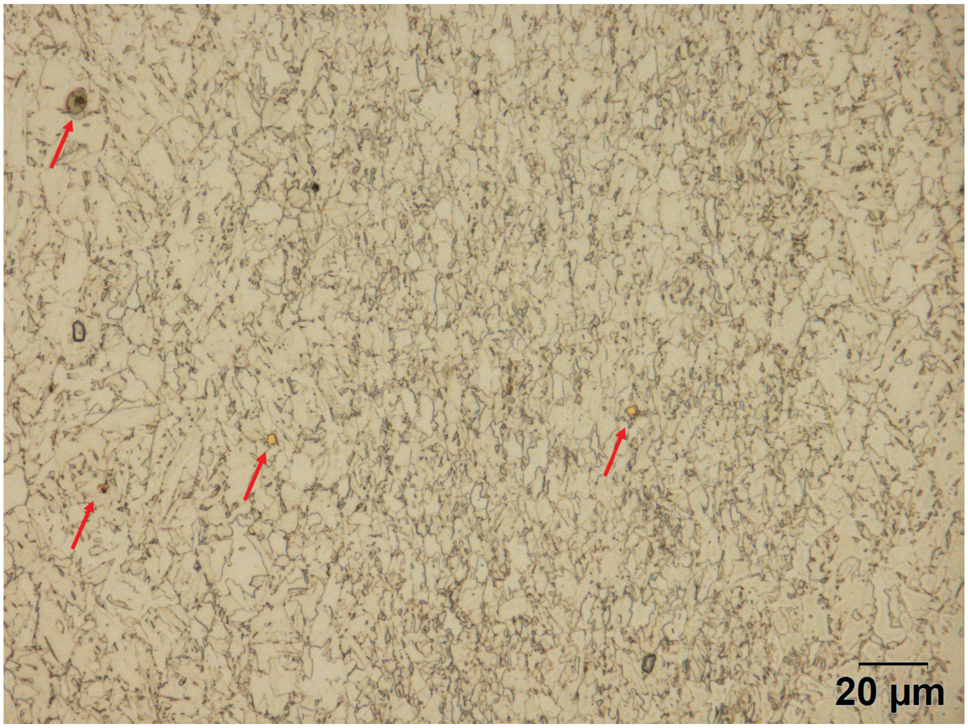

(a) 1-L.

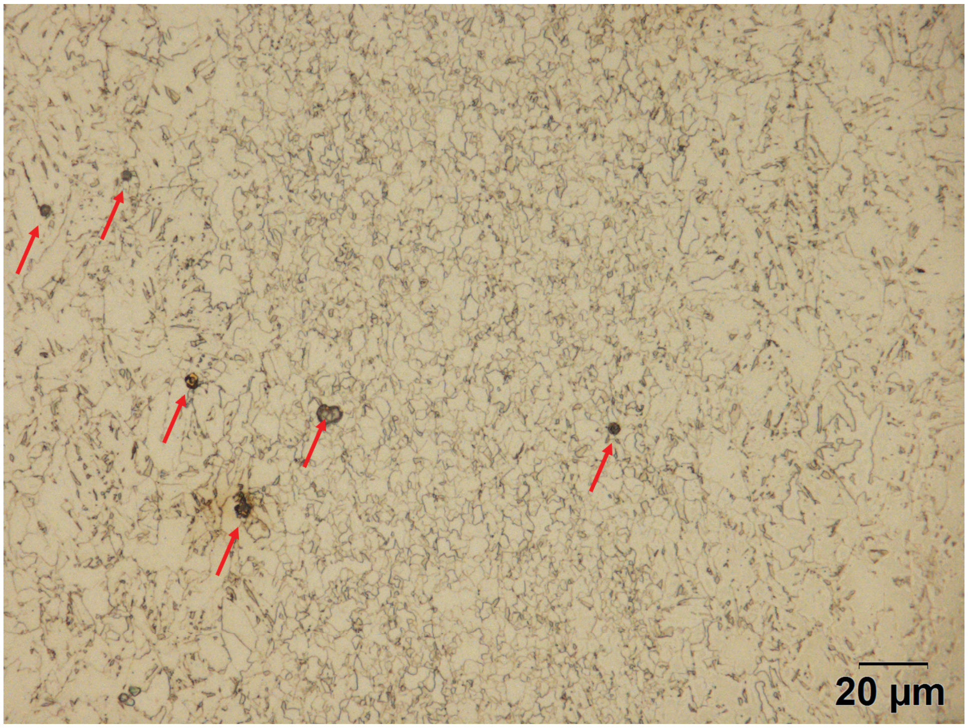

(b) 1-H.

Figure 3.8: Colour optical microscopy used to observe precipitates and inclusions.

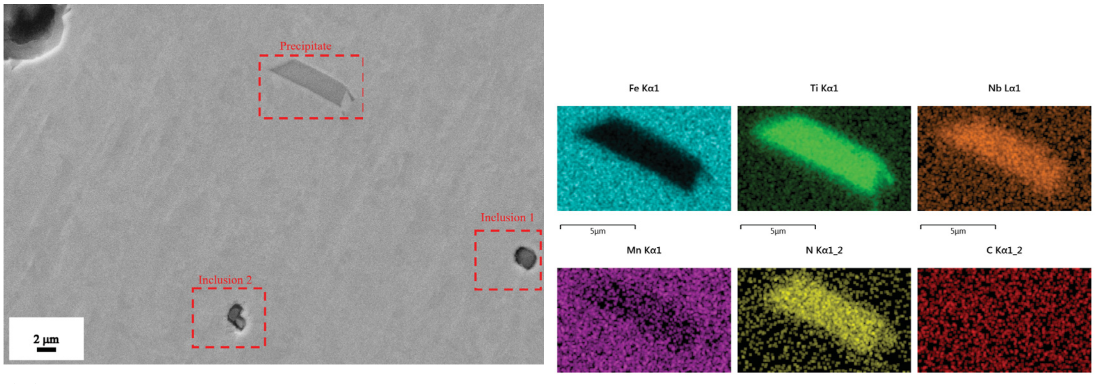

(a) As-welded samples from PWHT 1 processing, as-polished

(b) Precipitate EDS results.

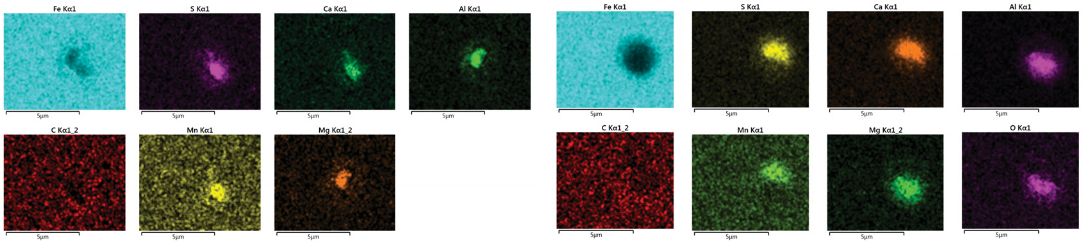

(c) Inclusion 2 EDS results.

(d) Inclusion 1 EDS results.

Figure 3.9: SEM with EDS to observe inclusions and precipitates in the as-welded material.

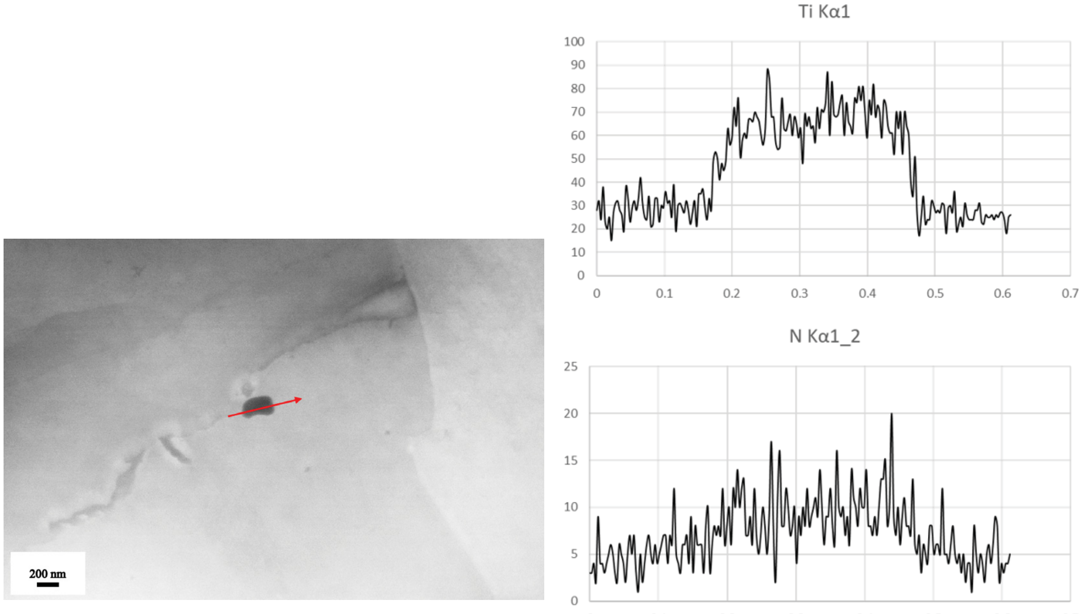

(a) Cubic precipitate in 1-L, bright field imaging.

(b) Precipitate EDS results.

Figure 3.10: T-SEM with EDS to observe a cubic precipitate in 1-L.

3.3.1 EBSD Observations

EBSD was next performed to provide a degree of quantitative certainty to supplement the qualitative observations of microstructural features. Grain size, grain boundary, phase, strain, and texture information were obtained from EBSD acquisition and post-acquisition data analysis. Due to the availability of equipment, high associated cost, and lengthy acquisition time, EBSD data was collected for 1-L and 2-H first, and EBSD data was collected for 1-H much later in the project once toughness performance metrics were obtained; due to the similarities observed in optical microscopy, it was not determined that a further study on 1-H would be needed until toughness performance data showed drastic differences in toughness between 1-L and 1-H. For specimens 1-L and 2-H, EBSD data was collected at a step size of 0.3 μm both at the bondline and in the area next to the bondline (NTB). Next, the instrument was focused on the bondline area and a slightly finer step size of 0.2 μm was used to acquire data in this smaller area in an effort to increase resolution in the fine grained regions. Later, a larger, coarser map with a step size of 0.8 μm was obtained that included both the bondline and the microstructure next-to-bondline for specimen 1-H. This was mainly to observe if similarities existed between 1-L and 1-H. While direct comparisons between 1-L and 2-H can be made, comparisons with 1-H must be made with care due to the decreased resolution associated with an increased step size. For quantitative measurements of specimens 1-L and 2-H, measurements of the bondline were taken from the 0.2 μm map of the bondline to ensure no adjacent grains were included, and that the smaller features were more accurately captured using the smaller step size. For the area next-to-bondline, the 0.3 μm step size maps were used. For 1-H, subsets were extracted from the larger map and are marked in the relevant figures.

Grain Size, Grain Boundary Distribution, and Phase Identification

Fig. 3.11 - 3.13 show the image quality and phase maps of all specimens, overlaid with subgrain and grain boundaries. Grain boundaries (high angle grain boundaries, HAGB) are defined as having misorientation angle $\theta \geq 10°$, and subgrain boundaries (low angle grain boundaries, LAGB) are defined as $2° \leq \theta < 10°$. Image quality maps show relatively strong acquisition; darker areas show regions of poorer image quality, with black being areas that were unable to be indexed to selected phases, or where patterns were unable to be obtained during acquisition. Usually, these areas represent areas of topographical interference, or high deformation causing the lattice parameter to deviate substantially. Phases selected for acquisition were BCC iron for ferrite and bainite, and FCC iron for austenite. Possible precipitate phases ($(\mathrm{Ti,Nb,V})_y(\mathrm{C,N})_x$) were also selected during initial acquisition; while some were detected, primarily NbC and TiN, these were small and were detected as single pixels that did not survive subsequent noise reduction processing. This is suspected to be due to the generally small size of such precipitates, although larger cubic precipitates were occasionally observed in optical microscopy.

It can be seen that all three specimens are almost entirely BCC iron phases. Specimen 1-L shows small, dispersed regions of austenite, consistent in positioning and morphology with the island phases observed in SEM and T-SEM. Since many of the non-indexed areas are associated with detected austenite and it is reasonable to conclude that these are M-A features; the austenite is a small portion, with the non-indexed areas being martensite. The change in lattice parameter from BCC to BCT and the high deformation associated with the displacive martensite transformation have deviated the lattice parameter such that it cannot be identified using the BCC iron standard lattice parameter used for reference. Specimen 2-H is almost austenite free, although non-indexed regions are present. This suggests that either: (1)the M-A features are almost entirely martensite with the austenite being below the resolution of the acquisition, or (2) etching topography is responsible for the non-indexed regions, or (3) a combination of both. As this sample is etched slightly deeper, it is most likely a case of topography with possibly minor and undetected M-A. The "island" features seen in optical microscopy are likely an etching effect due to local redistribution of alloying elements in the ferrite during solid-state transformation from austenite. While specimen 1-H is also mostly austenite free, this is likely an effect of the larger acquisition step size. With a step size of 0.8 μm, and the M-A features being 1-2 μm, the majority of austenite was likely only detected as isolated pixels that were removed during noise reduction data processing. Despite this, a few austenite readings were observed, likely larger M-A features.

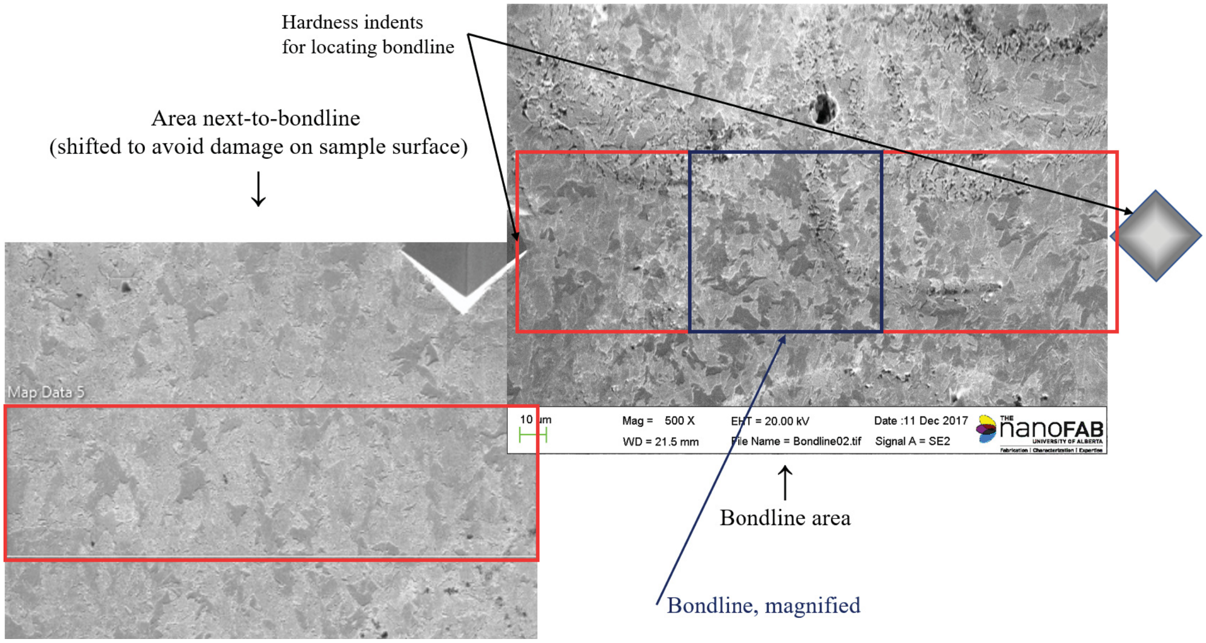

(a) Location of EBSD data acquisition.

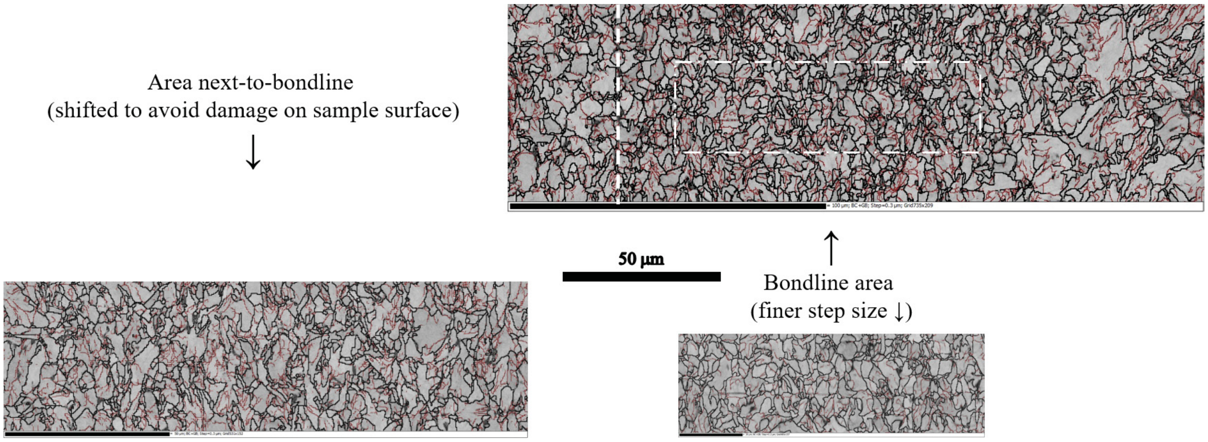

(b) Band contrast (image quality) map with overlaid with 2° subgrain boundaries (maroon) and 10° grain boundaries (black).

Figure 3.11: 1-L specimen EBSD maps showing image quality, phase, and grain size.

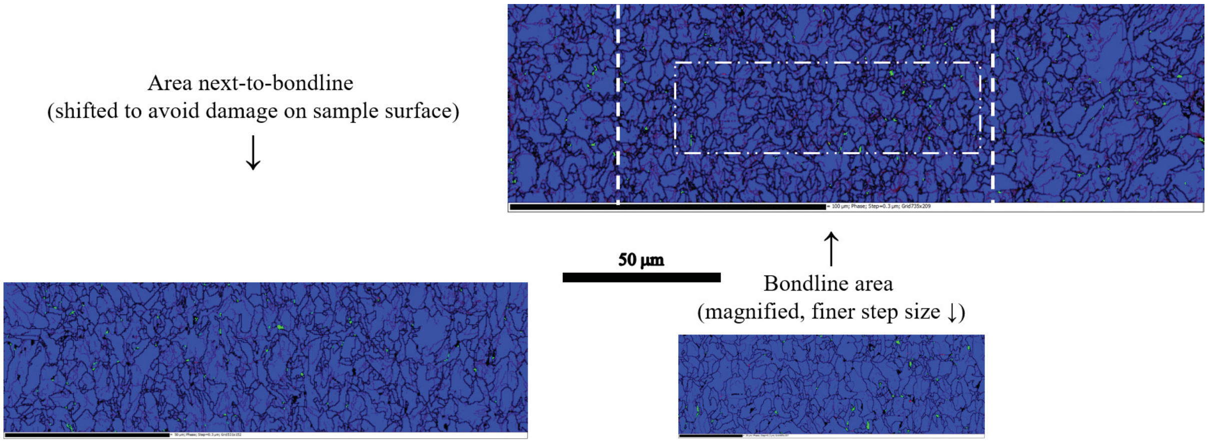

(c) Phase map showing bcc (ferrite) in blue, and fcc (austenite) in green. Overlaid with 2° subgrain boundaries (maroon) and 10° grain boundaries (black).

Figure 3.11: 1-L specimen EBSD maps showing image quality, phase, and grain size.(cont.)

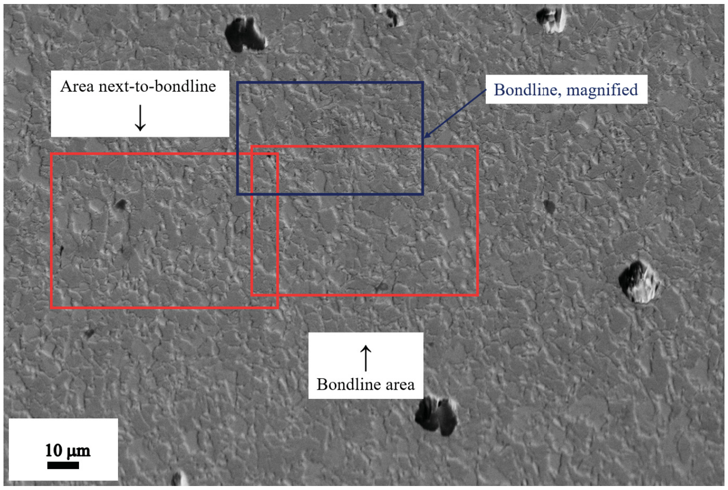

(a) Location of EBSD data acquisition.

Figure 3.12: 2-H specimen EBSD maps showing image quality, phase, and grain size.

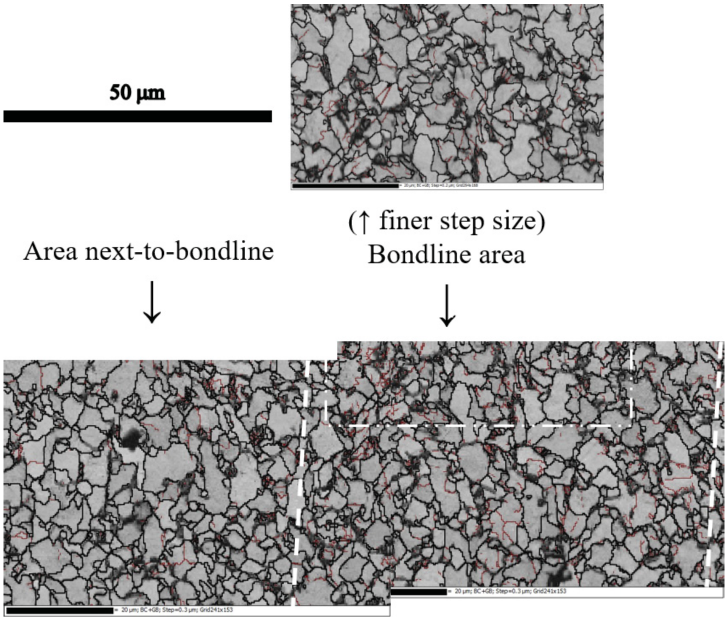

(b) Band contrast (image quality) map with overlaid with subgrain boundaries (maroon) and grain boundaries (black).

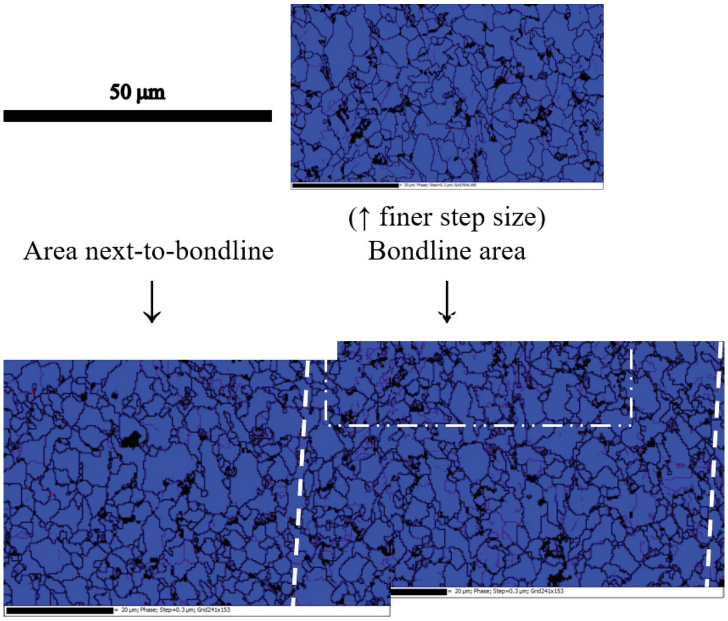

(c) Phase map showing bcc (ferrite) in blue, and fcc (austenite) in green. Overlaid with subgrain boundaries (maroon) and grain boundaries (black).

Figure 3.12: 2-H specimen EBSD maps showing image quality, phase, and grain size. (cont.)

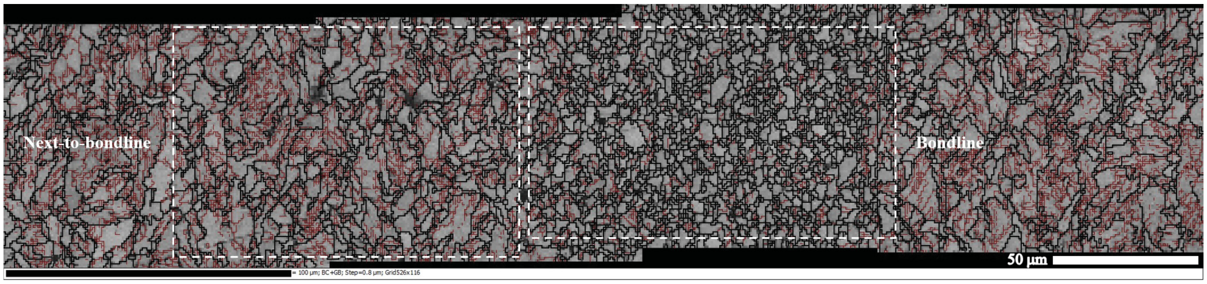

(a) Band contrast (image quality) map with overlaid with subgrain boundaries (maroon) and grain boundaries (black).

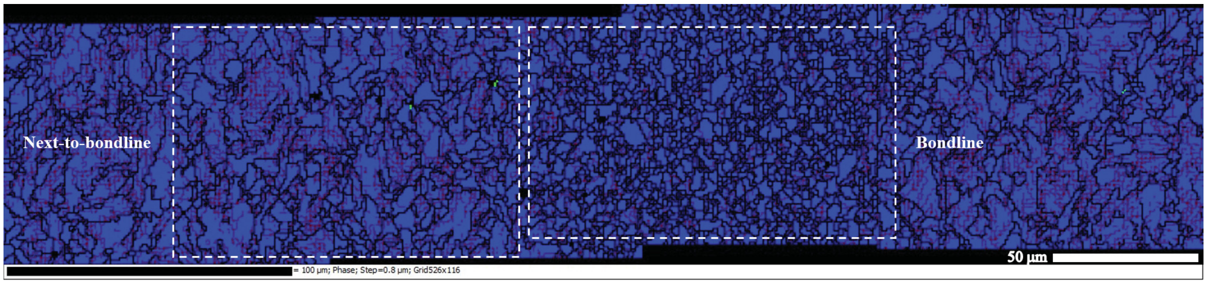

(b) Phase map showing bcc (ferrite) in blue, and fcc (austenite) in green. Overlaid with subgrain boundaries (maroon) and grain boundaries (black).

Figure 3.13: 1-H specimen EBSD maps showing image quality, phase, and grain size (SEM location unavailable).

Grain boundary distributions, reported as relative frequency, of the bondline and the area next-to-bondline are shown in Fig. 3.14. It can be seen that the in the bondline itself, the grain boundaries of 1-H and 2-H are predominantly HAGBs (67% & 63%, respectively), while in 1-L the inverse is true, with 40% HAGBs. In the area adjacent to the bondline, however, 1-L and 1-H are very similar, with only 32% and 31% fraction of HAGBs, respectively. The area next to the bondline in 2-H is consistent with the bondline itself with 68% HAGBs. These measurements are consistent with the visual observations in the maps. This indicates that 2-H has relatively less substructure or deformation than 1-L. It can be surmised that 1-H has a higher degree of substructure or deformation next to the bondline, similar to 1-L, and less substructure or deformation within the bondline, similar to 2-H. While the bondline measurements of higher HAGBs fraction and less substructure is consistent in both of the tougher specimens, the accuracy of the comparison is unknown due to the increased step size used in 1-H. Substructure and deformation will be discussed in greater detail later in *Strain Analysis*.

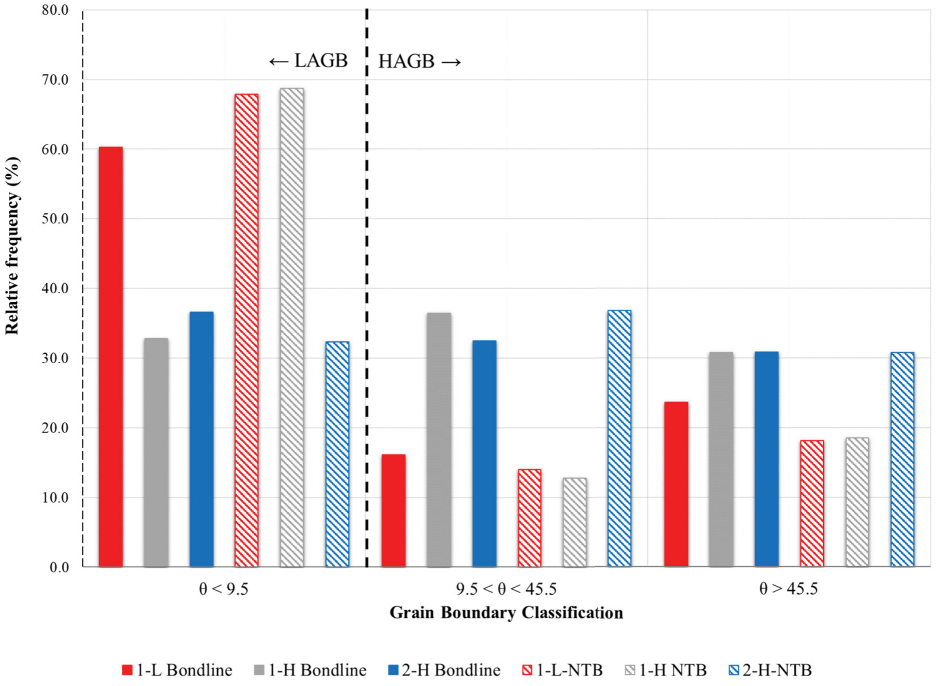

Figure 3.14: Grain boundary distribution for each of the specimens in the bondline and area next to bondline (NTB).

Grain size measurements are presented in Fig. 3.15 & 3.16, reported as histograms of the equivalent circle diameter with a bin size of 0.125 μm, in relative frequency and relative area fractions. Grains touching the borders of the selected area were excluded from the population as these grains may not be complete. To be included in the population, grain area was required to be greater than 10 pixels (as recommended by the Channel5 manual [42] to meet ISO 13067), and to have grain boundary angles where $\theta \geq 10°$. Area fraction was calculated using upper bin size of the equivalent circle diameter, converting to equivalent circle area, and multiplying by the frequency before normalizing over the total area. It can be seen that the increased step size in 1-H has cut off the small grains measured in 1-L and 2-H (change in minimum detected grain size from 0.7 μm in the bondline or 1.1 μ next to the bondline respectively to 2.9 μm), and subsequently shifted the average value slightly higher.

Overall however, the bondline grain size is very similar, with maximum grain sizes of 12.6 μm, 9.2μm, and 8.3μm for 1-L, 1-H, and 2-H, respectively, with the majority of grains being less than 7 μm. 1-L has a noticeable but minor fraction of grains larger than this in the bondline; while these large grains represent a relatively small fraction of the population, they account for a significant area fraction. While only ∼15% of the area in 1-H and 2-H consists of grains larger than 7 μm, 37% of the area in 1-L is contributed by grains larger than 7 μm. The bondline follows the conventional understanding that a refined grain size will lead to increased toughness performance.

The material adjacent to the bondline for sample 2-H is very similar to that in the bondline, with a maximum grain size of 8.9 μm. The grain size in 1-L and 1-H is larger, as observed by optical microscopy and SEM, with 1-H having significantly larger grain size. Maximum grain sizes were 17.7 μm and 45.5 μm in 1-L and 1-H respectively, and over 25% of 1-H's area is contributed by a small population of grains that are 45 μm.

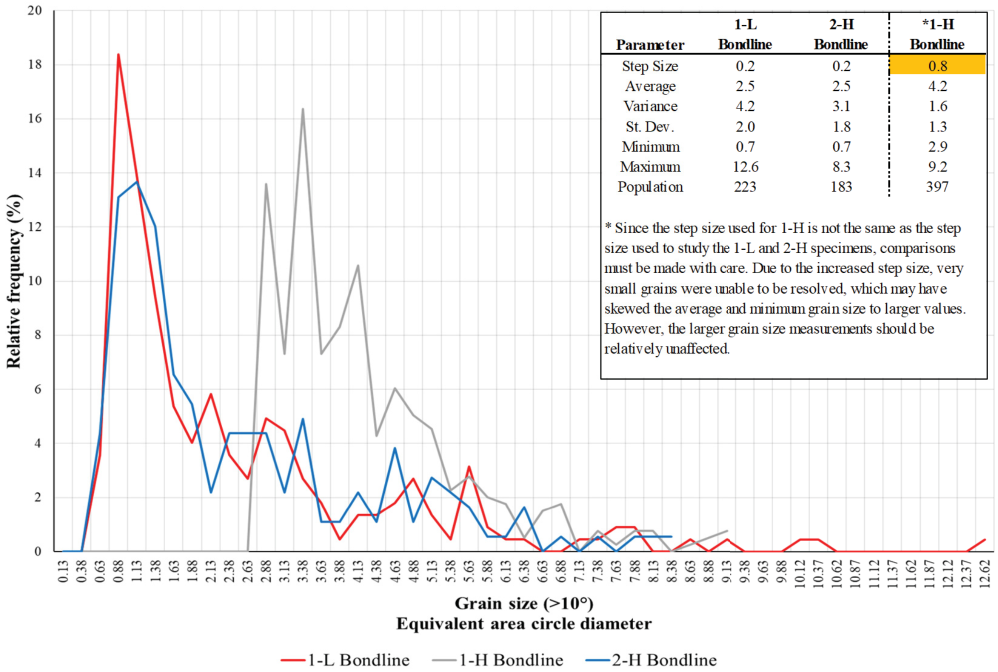

Parameter	1-L Bondline	2-H Bondline	*1-H Bondline
Step Size	0.2	0.2	0.8
Average	2.5	2.5	4.2
Variance	4.2	3.1	1.6
St. Dev.	2.0	1.8	1.3
Minimum	0.7	0.7	2.9
Maximum	12.6	8.3	9.2
Population	223	183	397

* Since the step size used for 1-H is not the same as the step size used to study the 1-L and 2-H specimens, comparisons must be made with care. Due to the increased step size, very small grains were unable to be resolved, which may have skewed the average and minimum grain size to larger values. However, the larger grain size measurements should be relatively unaffected.

(a) Relative frequency of grain sizes measured at the bondline

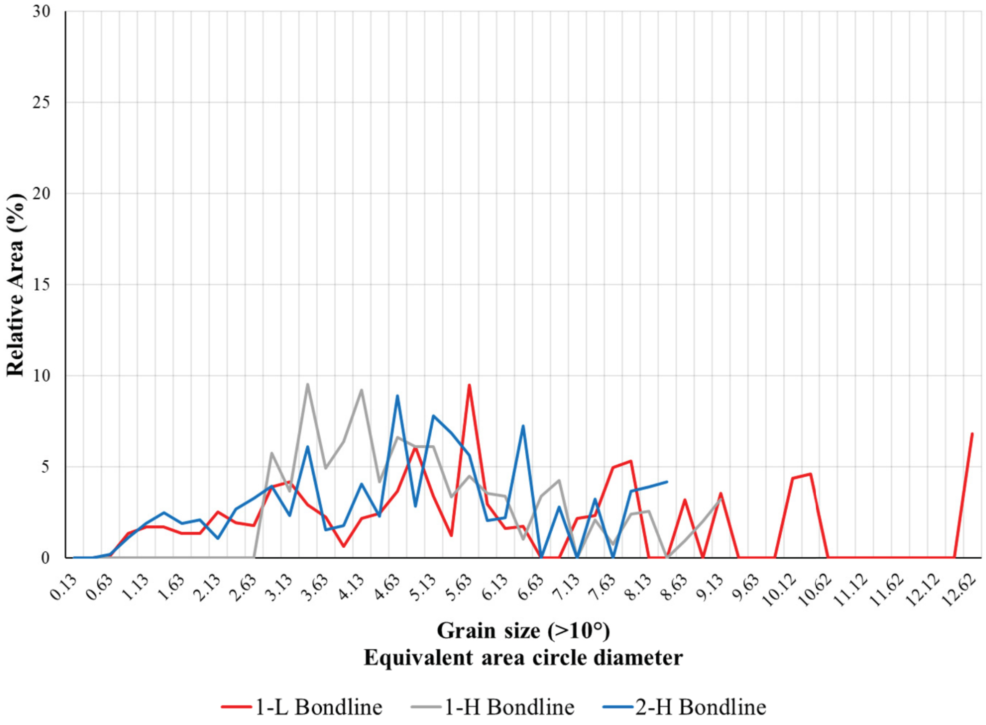

(b) Relative area contribution of grain sizes measured at the bondline

Figure 3.15: Bondline grain size measurements from EBSD. Grains were defined as those surrounded by HAGBs.

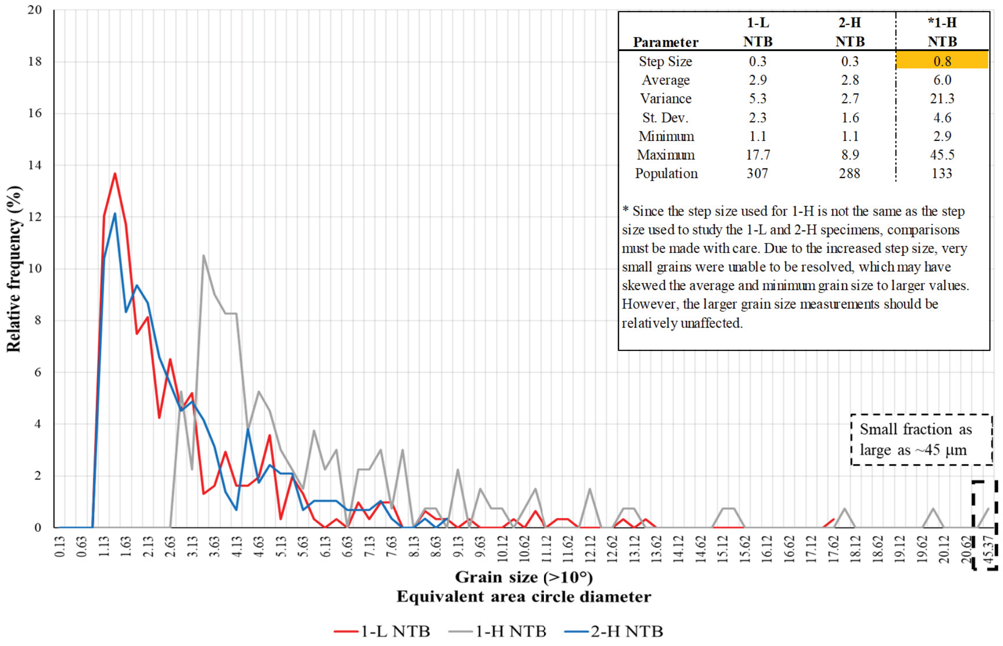

Parameter	1-L NTB	2-H NTB	*1-H NTB
Step Size	0.3	0.3	0.8
Average	2.9	2.8	6.0
Variance	5.3	2.7	21.3
St. Dev.	2.3	1.6	4.6
Minimum	1.1	1.1	2.9
Maximum	17.7	8.9	45.5
Population	307	288	133

* Since the step size used for 1-H is not the same as the step size used to study the 1-L and 2-H specimens, comparisons must be made with care. Due to the increased step size, very small grains were unable to be resolved, which may have skewed the average and minimum grain size to larger values. However, the larger grain size measurements should be relatively unaffected.

(a) Relative frequency of grain sizes measured next-to-bondline.

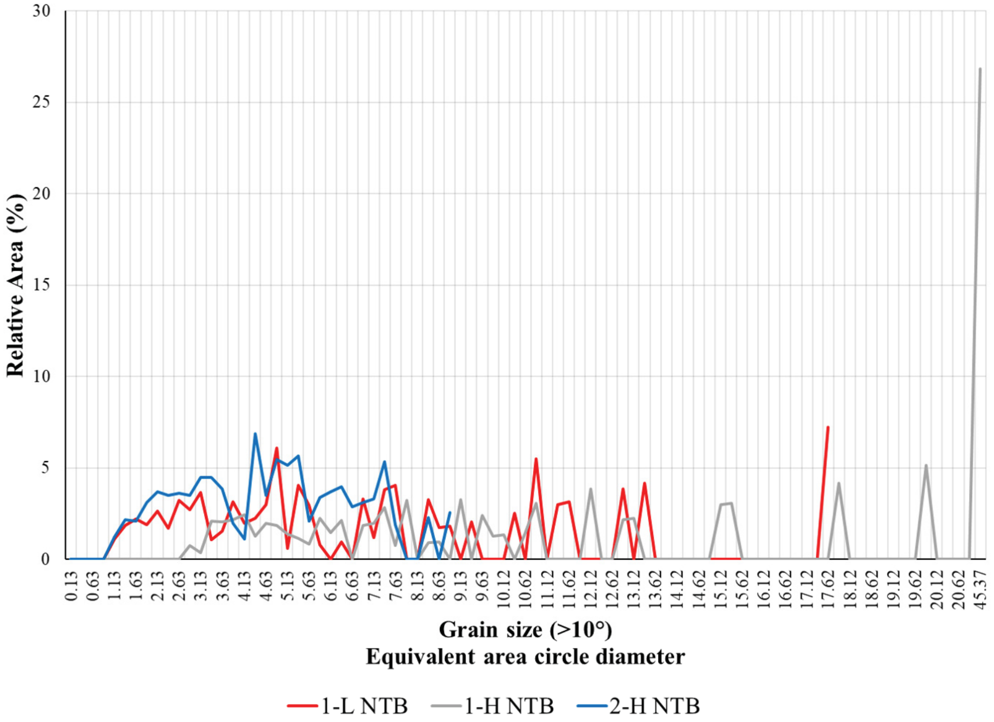

(b) Relative area contribution of grain sizes measured next-to-bondline.

Figure 3.16: Next-to-bondline grain size measurements from EBSD. Grains were defined as those surrounded by HAGBs.

Micro-texture

Fig. 3.17 - 3.19 show the local crystallographic orientations at the bondline and the area adjacent to the bondline. Three dimensional crystallographic orientation, represented using Euler space, and inverse pole figure (IPF) mapping of the RD-ND plane are presented. The ND-RD plan corresponds to the plane which runs along the longitudinal axis of the seam weld and through the thickness of the pipe from the ID to OD surfaces, and is thus the plane of interest in regard to toughness performance to prevent propagation of cracks. It is the tested plane of crack propagation in CVN testing. Of particular interest is the fraction of grains oriented with [001] planes along the crack propagation plane (shown in red).

Overall, a similar trend to the morphological grain size can be observed; 1-L and 1-H have a fine-grained bondline and a coarser grained area next-to-bondline, and 2-H has a refined grain size in both locations. However, in the IPF maps it can be seen that regions of similar crystallographic orientation create clusters of larger crystallographic grains that cross the morphological grain boundaries, resulting in an overall coarser crystallographic grain size along the plane of interest. Pole figures were analyzed but are not shown in the interest of brevity; there appears to be little to no texture in any of the specimens.

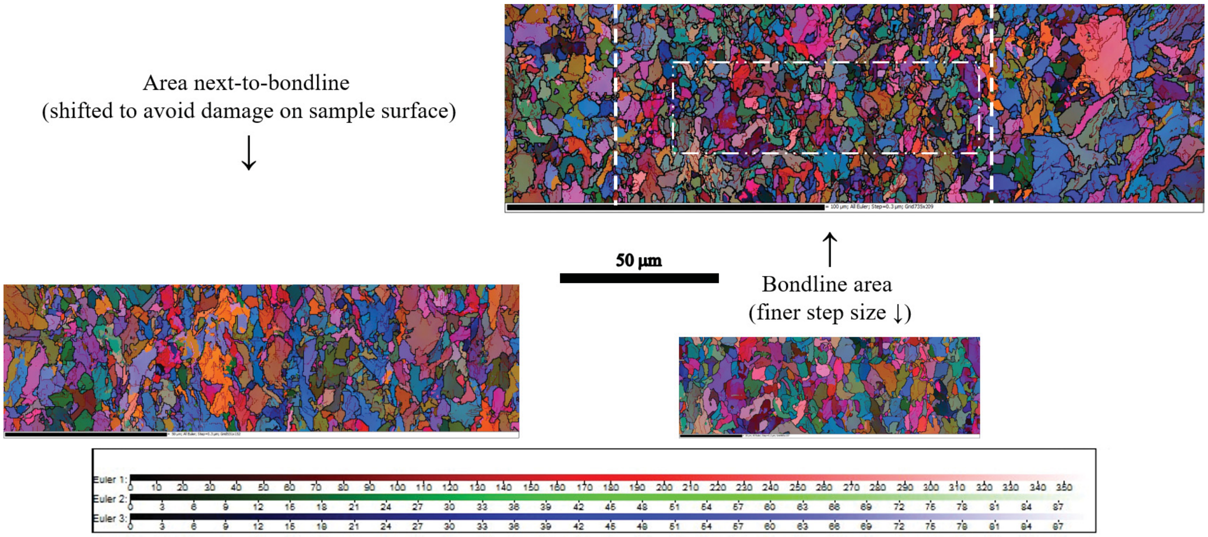

(a) All Euler angles map overlaid with 2° subgrain boundaries (maroon) and 10° grain boundaries (black).

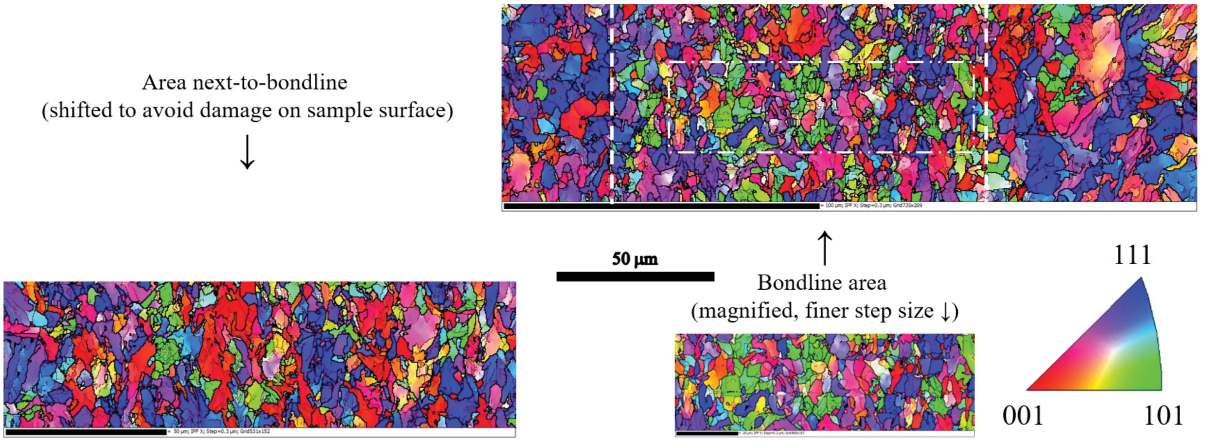

(b) Inverse pole figure of the crystallographic orientations parallel to crack propagation (RD and ND plane) map overlaid with 2° subgrain boundaries (maroon) and 10° grain boundaries (black).

Figure 3.17: 1-L specimen EBSD maps showing crystallographic orientations.

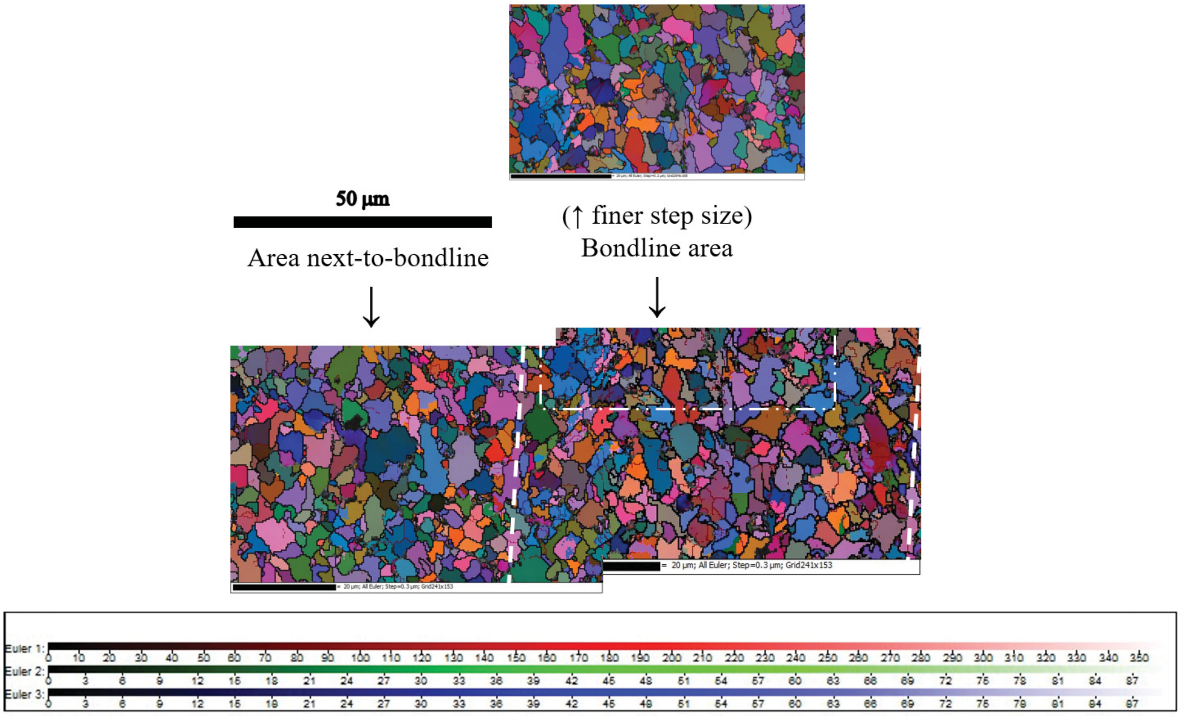

(a) All Euler angles map overlaid with 2° subgrain boundaries (maroon) and 10° grain boundaries (black).

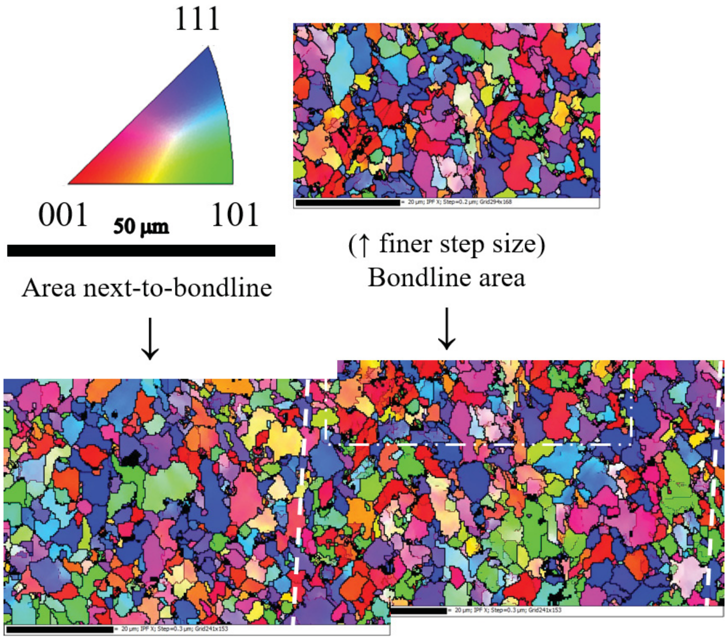

(b) Inverse pole figure of the crystallographic orientations parallel to crack propagation (RD and ND plane) map overlaid with 2° subgrain boundaries (maroon) and 10° grain boundaries (black).

Figure 3.18: 2-H specimen EBSD maps showing crystallographic orientations.

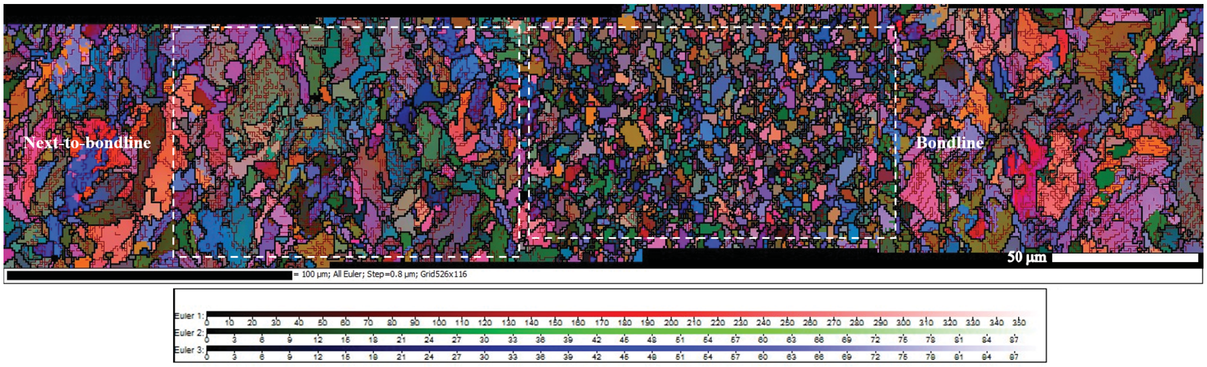

(a) All Euler angles map overlaid with 2° subgrain boundaries (maroon) and 10° grain boundaries (black).

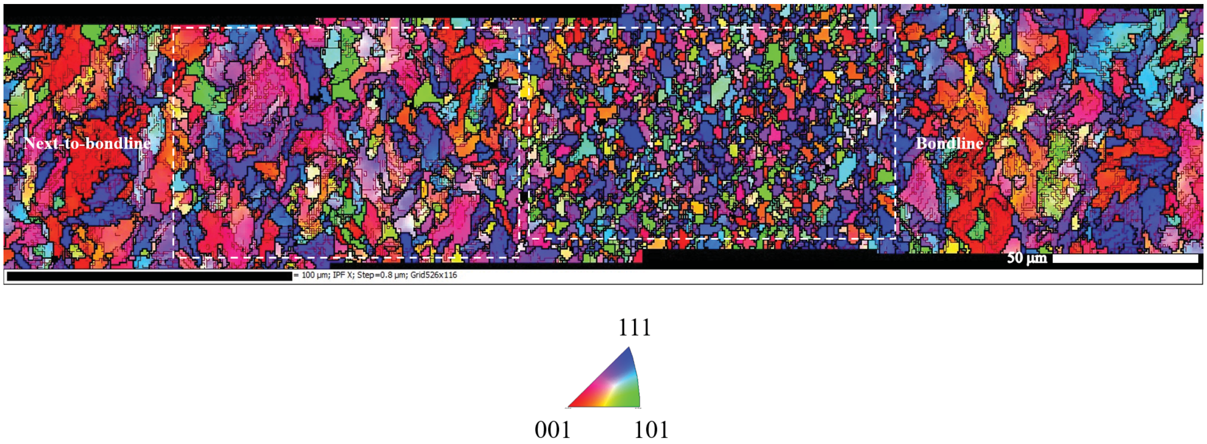

(b) Inverse pole figure of the crystallographic orientations parallel to crack propagation (RD and ND plane) map overlaid with 2° subgrain boundaries (maroon) and 10° grain boundaries (black).

Figure 3.19: 1-H specimen EBSD maps showing crystallographic orientations.

Strain Analysis

Strain analysis was conducted during post-acquisition processing. Maps created using two different strain analysis methods are shown in Fig. 3.20 - 3.22; Kernel Average Misorientation (KAM) to visualize localized strain, and Grain Average Misorientation (GAM) to visualize strain on a grain-by-grain level. KAM maps are plotted to a maximum of 5° misorientation, and GAM maps were calculated using a critical misorientation angle, θ_c, of 1°. Due to the sensitivity of strain analysis to step size, only maps of identical step size can be compared. Drastic changes can be observed in the maps at the same location going from an acquisition step size of 0.3 μm to 0.2 μm for specimens 1-L and 2-H. Thus while 1-L and 2-H can be compared to each other, maps of 1-H can only be used for internal comparisons.

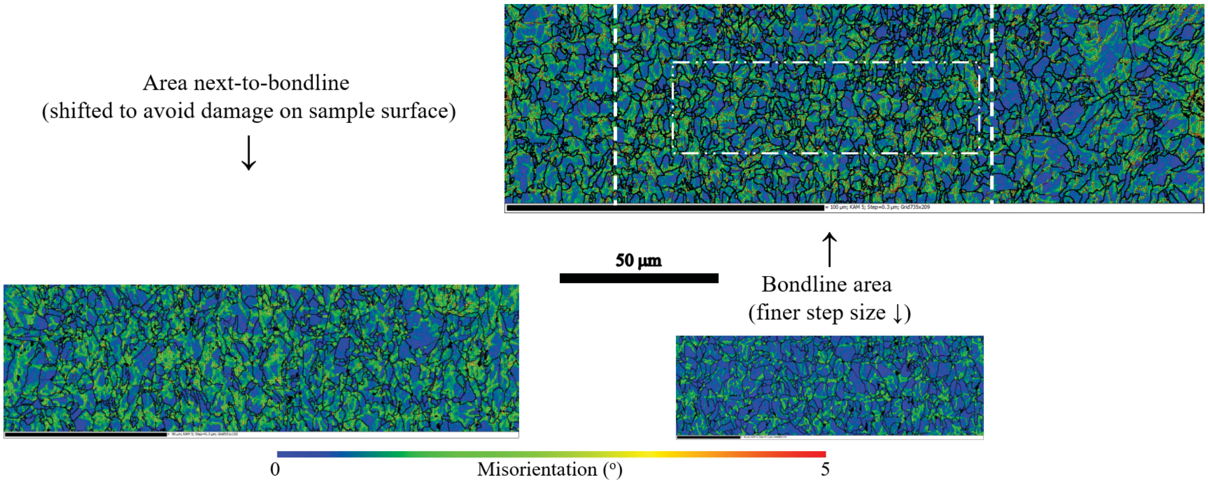

(a) KAM map using a maximum 5° misorientation cutoff overlaid with 2° subgrain boundaries (maroon) and 10° grain boundaries (black).

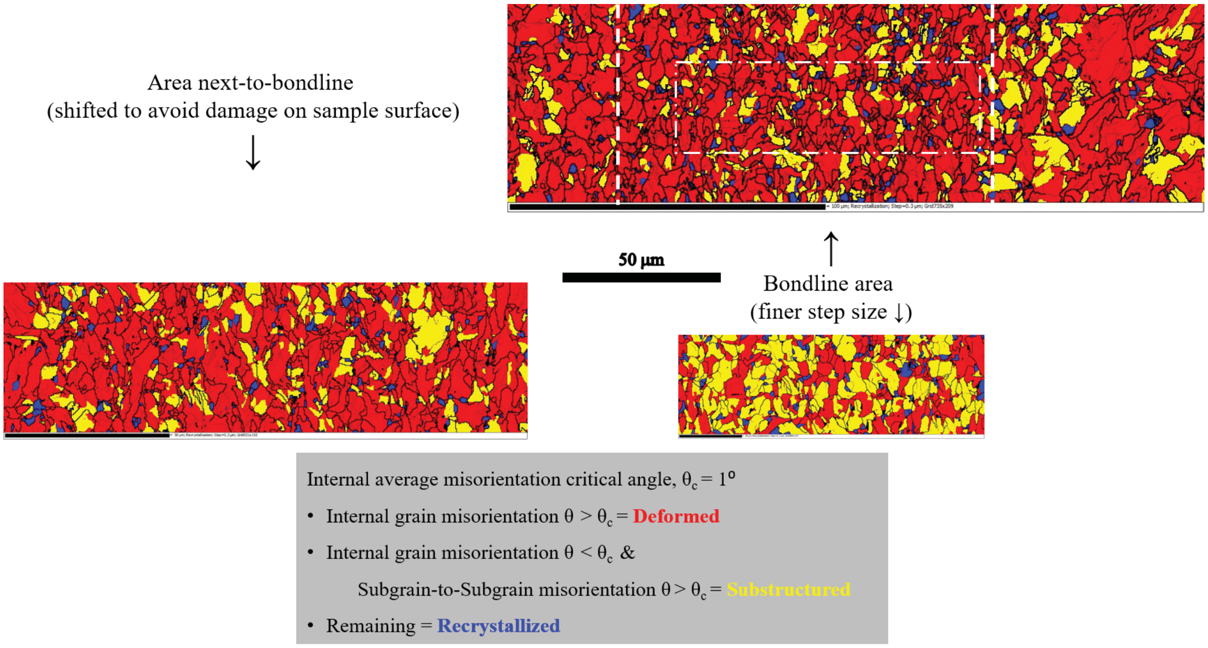

(b) GAM map overlaid with 2° subgrain boundaries (maroon) and 10° grain boundaries (black).

Figure 3.20: 1-L specimen EBSD maps showing strain measurements.

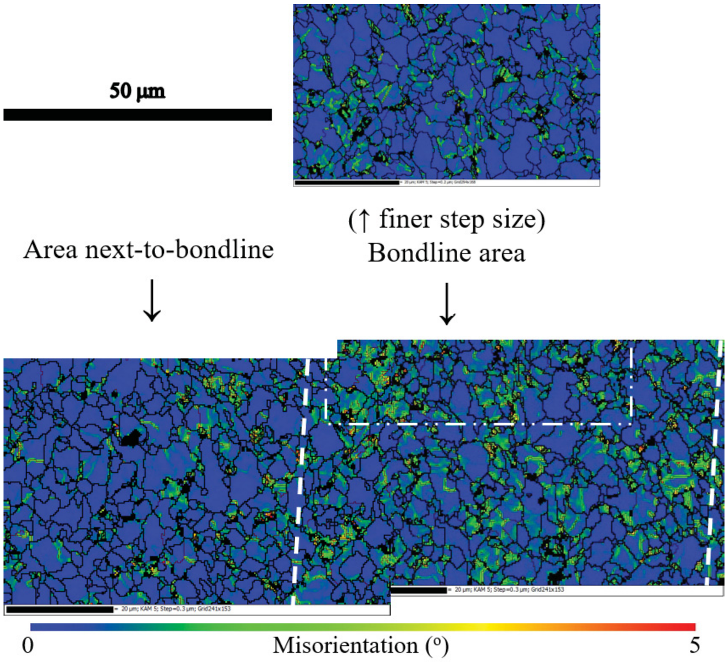

(a) KAM map using a maximum 5° misorientation cutoff overlaid with 2° subgrain boundaries (maroon) and 10° grain boundaries (black).

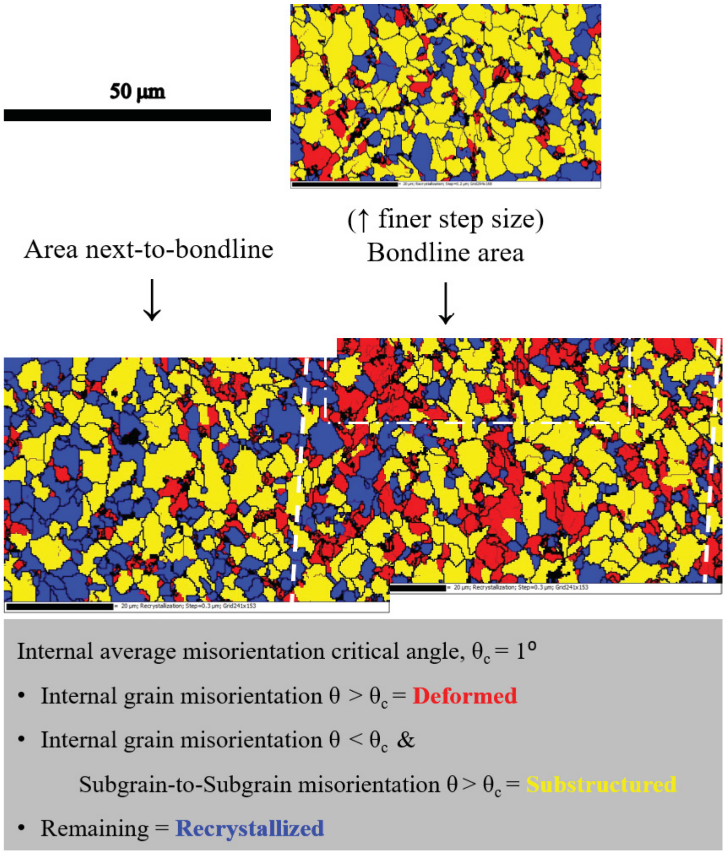

Internal average misorientation critical angle, $\theta_c = 1°$

- Internal grain misorientation $\theta > \theta_c$ = **Deformed**
- Internal grain misorientation $\theta < \theta_c$ &

  Subgrain-to-Subgrain misorientation $\theta > \theta_c$ = **Substructured**
- Remaining = **Recrystallized**

(b) GAM map overlaid with 2° subgrain boundaries (maroon) and 10° grain boundaries (black).

Figure 3.21: 2-H specimen EBSD maps showing strain measurements.

From Fig. 3.20 it can be seen that 1-L is predominantly strained to the extent of being classified as deformed in both the bondline and the area next to the bondline as measured with a 0.3 μm step size. Very few grains are calculated to be no-to-very low strain (recrystallized), which correspond to smaller ferrite grains at triple points. A refined step size at the bondline reveals that with increased resolution, the fraction of substructured and deformed grains is approximately even, whereas the slightly larger step size suggested that the material was almost entirely deformed. This is in contrast with specimen 2-H in Fig. 3.21, which has much lower strain with non-uniform distribution. The area adjacent to the bondline is shown to be mainly recrystallized and substructured, with the bondline trending to an increased presence of deformed grains, although the majority are revealed to be substructured when the step size is decreased. Specimen 1-H in Fig. 3.22 can be seen to have both a highly strained and deformed area adjacent to the bondline, with a small fraction of unstrained (recrystallized) grains similar to 1-L, and a relatively unstrained bondline, similar to but not as low in strain as 2-H. However, it is unknown what a strain analysis with a smaller step size and better resolution may reveal. If the trend seen in switching from 0.3 μm, to 0.2 μm in 1-L and 2-H continues, then we would expect to see a shift toward lower strain and a higher fraction of recrystallized and substructured grains with decreasing step size. In all three specimens, areas of highest strain tend to focus around the non-indexed regions, further supporting that these are M-A constituents with high local strain from the highly displacive martensite transformation. Fig. 3.23 quantifies these observations at the highest resolution available for each specimen and region.

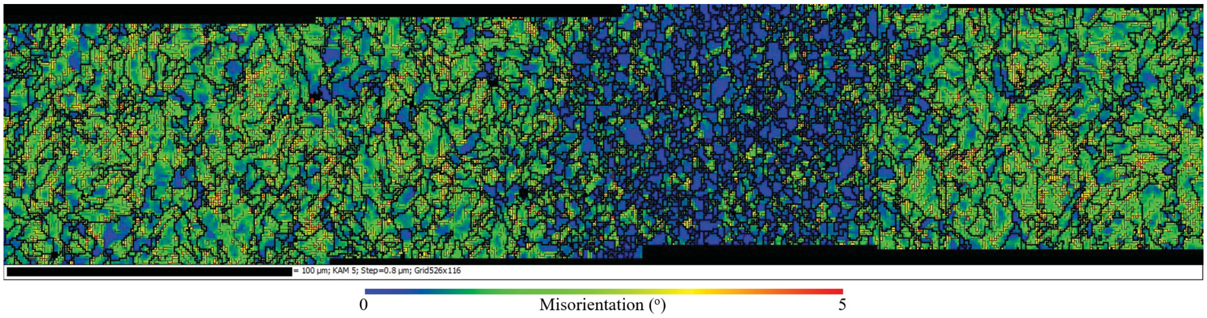

(a) KAM map using a maximum 5° misorientation cutoff overlaid with 2° subgrain boundaries (maroon) and 10° grain boundaries (black).

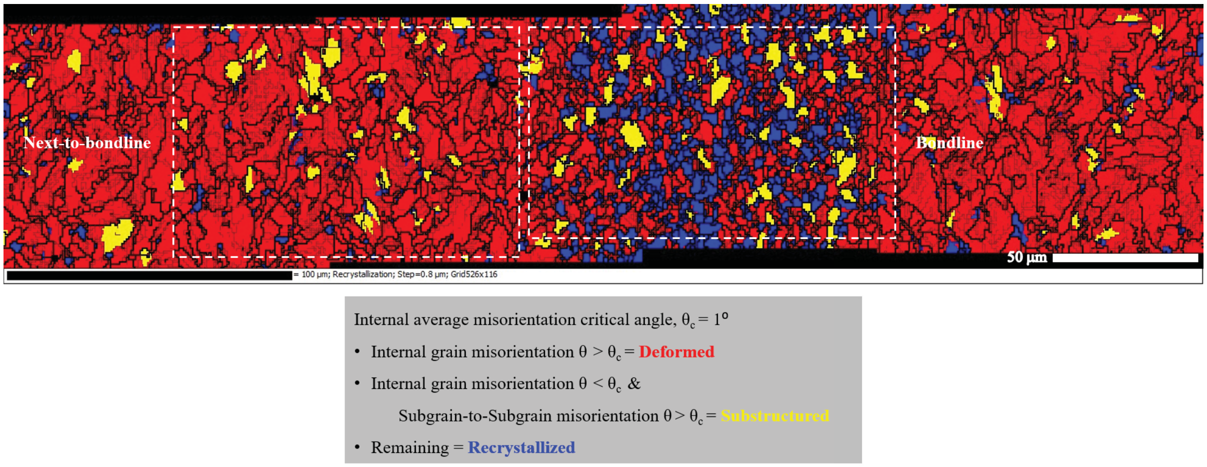

(b) GAM map overlaid with 2° subgrain boundaries (maroon) and 10° grain boundaries (black).

Figure 3.22: 1-H specimen EBSD maps showing strain measurements.

The strain analysis reflects observations made in optical microscopy in Fig. 3.3. The high strain in the coarse-grained area adjacent to the bondline in 1-L and 1-H is consistent with the bainitic structure of these regions. The fine-grained, equiaxed ferrite in 1-H and 2-H is relatively strain free; the strain observed in the bondline ferrite of 1-L can be explained by the retained morphological elongation stemming from deformed grains persisting at the bondline.

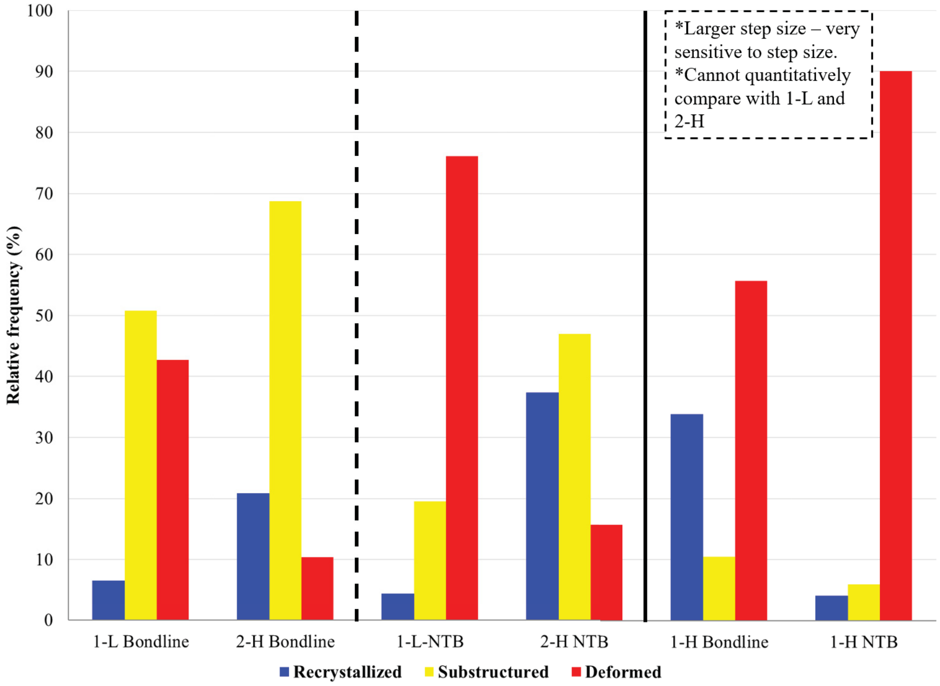

Figure 3.23: Quantitative fractions of strained material for each of the specimens in the bondline and area next to bondline (NTB). The bondline maps of 1-L and 2-H use the 0.2 μm step size maps, and the NTB area uses the 0.3 μm step size for the quantitative analysis. Specimen 1-H has a step size of 0.8 μm.

3.3.2 Weld Seam Micro-Hardness

Micro-hardness measurements were used to investigate local mechanical properties at the bondline and adjacent to the bondline in all specimens. Fig. 3.24 shows a schematic of the methodology used. With a load of 50 g, it was observed that indent size was approximately 25 μm. A vertical and horizontal spacing of 75 μm was used to avoid strain hardening effects on subsequent indents. By offsetting each row by 25 μm, a line scan perpendicular to the bondline through-thickness axis can be approximated. This matrix was performed such that local micro-hardness values of both the bondline and the area adjacent to the bondline were captured. Two areas per sample were taken, close together at the approximate mid-thickness, in order to obtain a larger sample set for statistical analysis. Area 1 is closer to the OD surface than area 2 in all specimens. Results are displayed in Fig. 3.25 and Tables 3.2 & 3.3. For the statistical analysis, statistically different refers to significantly different as determined by t-test comparison using a 95% confidence interval. Outliers were removed before statistical analysis and are marked on Fig. 3.25; these are suspected to be indents that encountered porosity or softer inclusions. Statistical analysis was performed at 3 levels:

- To determine if Area 1 and Area 2 were statistically similar or not.
    - Only in specimen 1-H were the two areas found to be statistically different. Both areas were still considered a single population in subsequent analysis.
- To determine if the specimens were statistically different from each other.
- To determine if the bondline was statistically different from the area next to the bondline within each specimen.

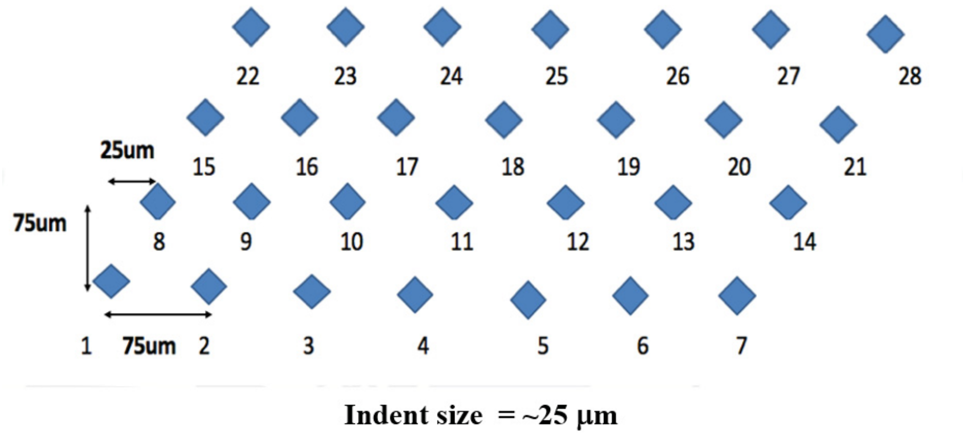

Figure 3.24: Representative schematic of hardness matrix. Note that actual number of points varied based on bondline thickness at location.

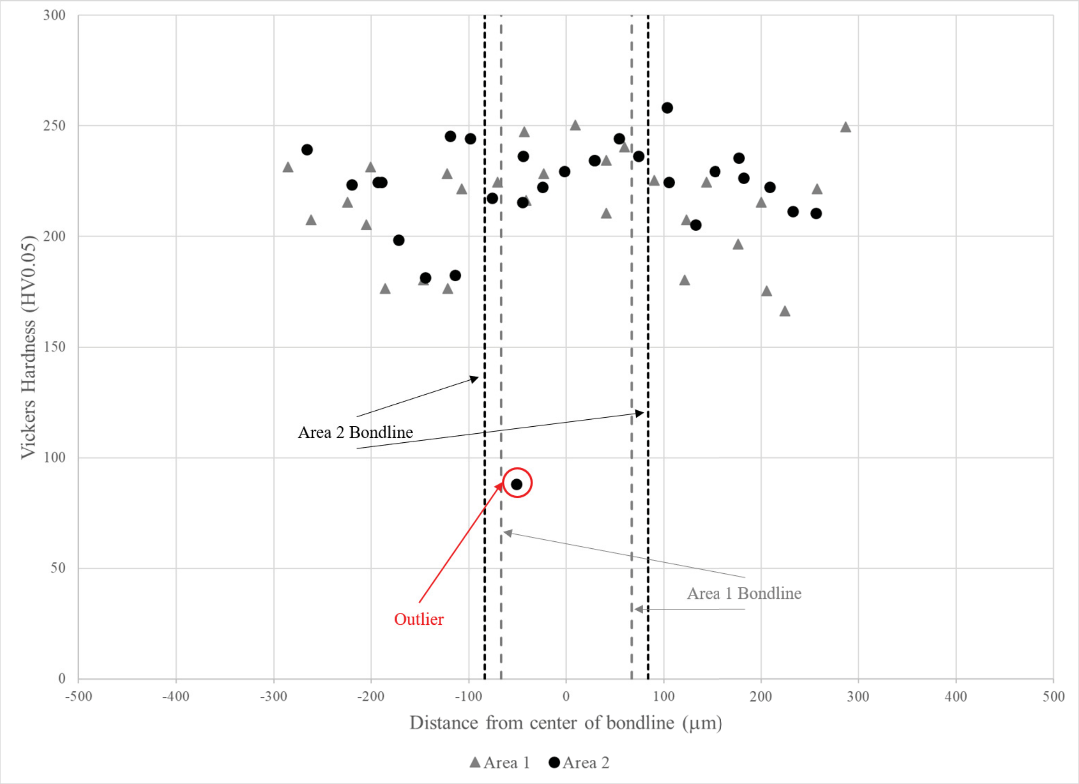

(a) Specimen 1-L.

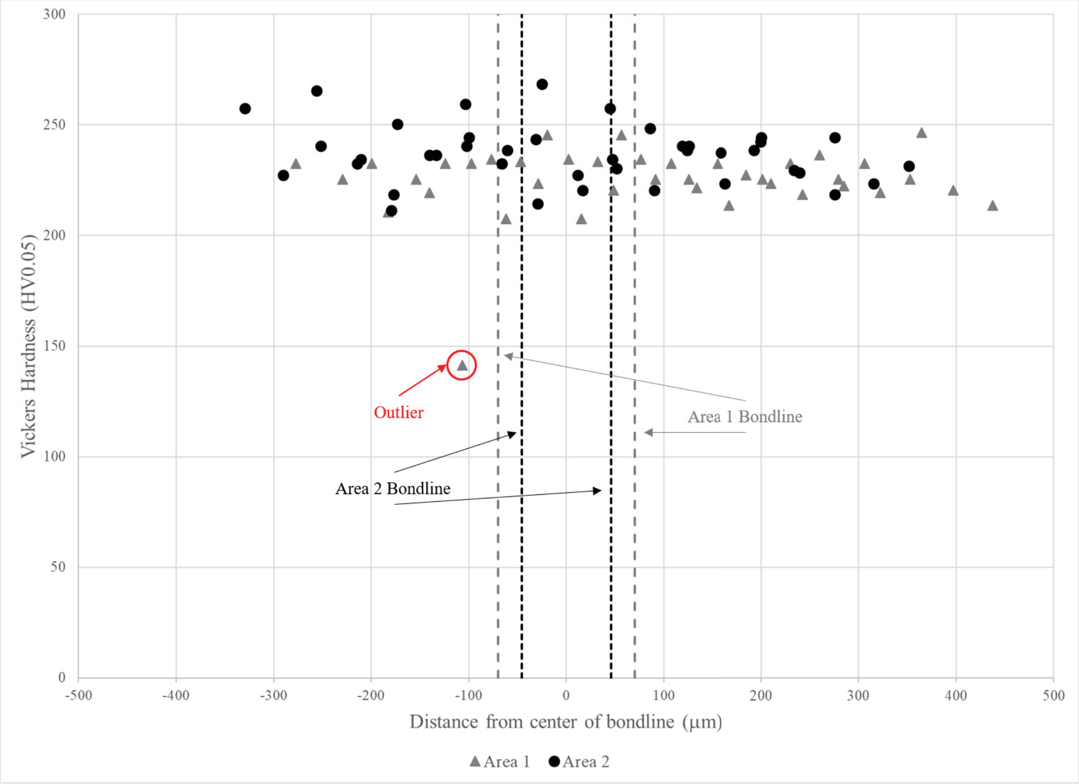

(b) Specimen 1-H

Figure 3.25: Local micro-hardness as a function of the distance from the bondline.

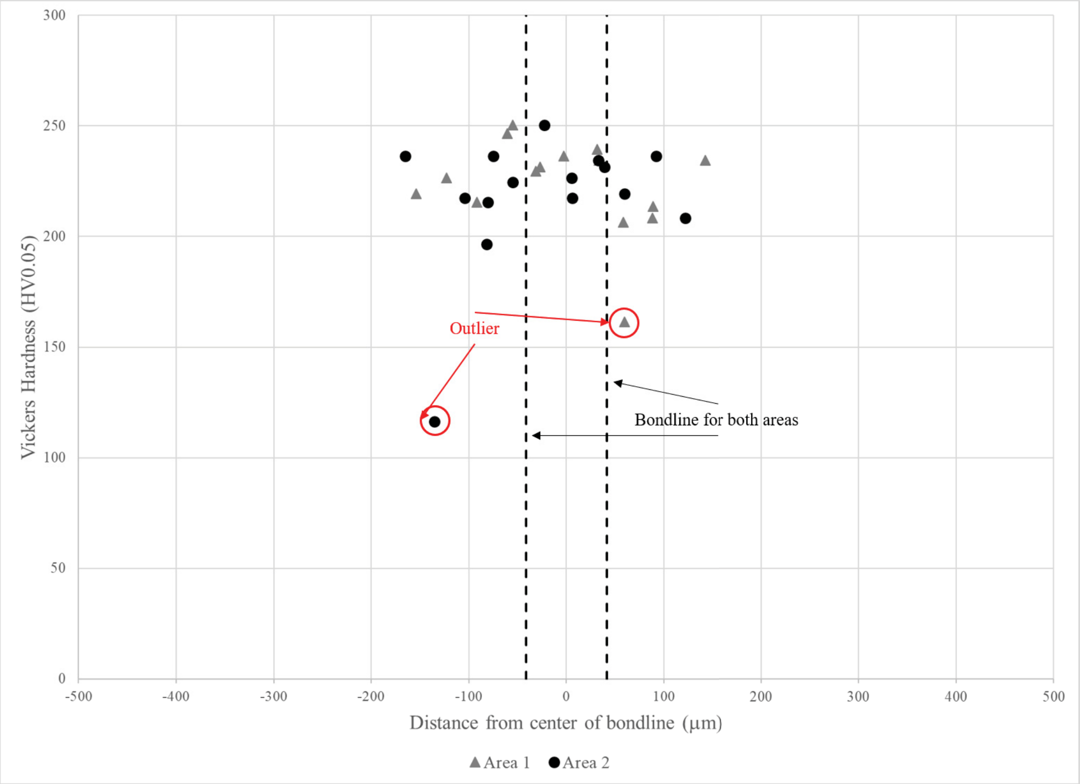

(c) Specimen 2-H.

Figure 3.25: Local micro-hardness as a function of the distance from the bondline. (cont.)

Table 3.2: Micro-hardness specimen comparison statistical analysis results.

Specimen	Mean (HV0.05)	Variance (HV0.05)	Statistically Different From
1-L	220	474	Specimen 1-H
1-H	231	179	Specimen 1-L
2-H	227	184	None

Table 3.3: Micro-hardness at the bondline versus next to the bondline statistical analysis results.

Specimen	Bondline Mean (HV0.05)	Bondline Variance (HV0.05)	NTB Mean (HV0.05)	NTB Variance (HV0.05)	Statistically Different
1-L	232	142	215	528	Yes
1-H	233	243	232	134	No
2-H	230	139	223	214	No

Statistically, specimens 1-L and 1-H are the only two specimens different from each other when looking at the entire weld seam region. Hardness values typically fall within 200-250 HV0.05 in specimens 1-H and 2-H, with 1-H having some values higher than this. While the bondline of specimen 1-L is similar, it has a significant softening in the area next to the bondline, ranging from approximately 160-250 HV0.05. This softening was determined to be statistically significant and mainly occurs within 100-150 μm of the bondline. Internally, specimen 1-H shows very similar micro-hardness across the bondline and the area adjacent to it. While 2-H shows a slightly softer area next to the bondline when compared to the bondline, this difference is not statistically significant.

3.4 Summary of Findings

Overall, many observations of competing factors possibly influencing toughness were made by applying standard and advanced mechanical property measurement and metallographic characterization techniques. The difficulty arises in attempting to identify the dominating factor(s) and correlate them with their origin and development during manufacturing. This difficulty is compounded by the many unknowns inherent to the investigated specimens. Table 3.4 summarizes the observations made, as well as their suspected influence on toughness based on known fundamentals and the observations in this work. PWHT 2's greater toughness may be due to the resulting low strain, homogeneous ferrite structure in both the bondline and adjacent area. The observation of a softened region in the HAZ of specimen 1-L adjacent to the bondline may account for the drastically poorer toughness performance of this changeover. Without the tested CVN specimens from this changeover to investigate the crack initiation and propagation path, this cannot be confirmed in this study; however, discussions with subject matter experts employed by the manufacturer indicate that crack propagation in low-toughness samples has been observed to be in this region adjacent to the bondline [43]. The mechanism of the formation of the softened region is unclear, however, a possible hypothesis to explain the softened zone can be made by drawing parallels to work by Wang *et al.* [44].

Studying Grade P91 fusion weldments creep performance, Wang *et al.* found that creep performance of PWHT-ed weldments was degraded in a "soft-zone" that corresponded to the inter-critical heat affected zone (ICHAZ). This was attributed to the influence of local composition variation and prior structures from the base material and welds, which preferentially austenitized, resulting in a heterogeneous structure of soft tempered retained grains and harder newly transformed grains. Similar observations of a softened microstructure and strain distribution were made in this investigation. Further characterization is needed to conclusively determine if a similar mechanism is responsible in the manufactured ERW welds investigated in this study. It is suspected that a similar dual phase microstructure, of soft allotriomorphic ferrite and harder bainite in the area forming the soft zone may be responsible. It is also unclear why this phenomena would present in this material; the use of a nominal PWHT cycle with peak temperatures higher than the austenitization temperature makes an ICHAZ in this area unlikely. It is suspected that prior structures developed during the ERW welding are creating inhomogeneous regions that form dual-phase structures on cooling; this theory is supported by subject matter experts employed by the manufacturer [43], but remains to be conclusively proven. Another possible explanation would be variations in heat input and subsequently the cooling rate developing from differing manufacturing line speeds, target temperatures, or changes in pipe wall thickness; it is possible a dual phase structure may present on cooling if the cooling rate is near the ferrite-to-bainite transition. This suggests a fairly high sensitivity to the peak temperature achieved during the PWHT. Investigating this hypothesis requires a more detailed understanding of the manufacturing parameters used and a more in-depth characterization of the soft zone in order to correlate material response to manufacturing history. Further discussion of this can be found in *Chapter 4*, and a potential study to investigate this phenomenon will be outlined further in *Future Work* in *Chapter 5*.

Table 3.4: Summary of investigative observations.

Factor	Observations	Suspected Influence on Toughness
Microstructure and Grain Size	1-L - fine-grained, elongated, allotriomorphic ferrite at the bondline and coarse bainitic ferrite in the adjacent area. 1-H - majority is fine-grained, equiaxed, allotriomorphic ferrite at the bondline and coarser bainitic ferrite in the adjacent area. Has coarsest grain size in both bondline and adjacent area, as large as $\sim$45 μm in adjacent to the bondline. 2-H - fine-grained, equiaxed, allotriomorphic ferrite across weld seam.	A fine-grained, equiaxed, allotriomorphic ferrite at the bondline appears to improve toughness performance. Elongation consistent with retained deformation appears to drastically reduce toughness performance.
Grain Boundaries	1-L - Predominantly LAGBs 1-H - Predominantly LAGBs in the area adjacent to the bondline and predominantly HAGBs in the bondline itself. 2-H - Predominantly HAGBs.	HAGBs provide a more effective energy barrier to dislocation motion.
M-A Constituents	Small fraction of fine (1-2 μm), distributed M-A observed in all specimens. PWHT 1 appears to produce more M-A than PWHT 2.	Minimizing M-A contributes to improved toughness performance.
Micro-texture	Crystallographic grain size trends are similar to morphological grain size, although, the plane parallel to the plane of crack propagation can be seen to have some clusters resulting in larger crystallographic grain size than morphological grain size. Crystallographic orientations are reasonably random and distributed; little to no texture was observed.	Texture of [001] planes oriented parallel to the plane of crack propagation can increase susceptibility to brittle crack propagation. This was not observed.
Local Strain	1-L - Predominantly relatively highly strained across the entire weld seam area. Most grains are substructured if not deformed. A small fraction of recrystallized grains present at GB triple points. 1-H - Area adjacent to the bondline is highly strained and deformed compared to the bondline, which has relatively lower strain with a significant recrystallized fraction. A small fraction of unstrained grains are present at BG triple points in the next-to-bondline area 2-H - Relatively low strain across the entire weld seam region, with predominantly substructured grains and a significant recrystallized fraction.	A low-strain bondline appears to contribute to improved toughness performance.
Micro-hardness	1-L - A 100-150 μm area next to the bondline shows significant local softening and is statistically different from the bondline itself. This specimen's weld seam regions is statistically softer than the weld seam region of specimen 1-H. 1-H - Fairly uniform in terms of hardness across the weld seam region, in the range of 200-260 HV0.05. 2-H - Hardness in the range of 200-250 HV0.05 with a slight softening in the area next to the bondline, however not statistically significant.	Formation of a statistically significant softened zone may provide a preferential crack path within the weld seam and reduce toughness next to the bondline.

Chapter 4

Physical Simulation of Post-Welding Heat Treatments

4.1 Low-Temperature Toughness Performance

Specimens created using the Gleeble thermomechanical simulator were tested at -30 °C and -45 °C, with the results shown in Fig. 4.1, and the averages summarized in Table 4.1. A similar temperature profile to PWHT 2 was used, as this was observed by subject matter experts of the manufacturer to produce more consistent, better performing low-temperature toughness weld seams [40]. Since exact times during the PWHT cycle were unknown, but were known for PWHT 1, the times were assumed to be similar and used accordingly. Different peak temperatures on the final normalizer were investigated; as this is one of the known differences. Averages from the CVN testing of the manufactured pipe changeovers are provided for comparison.

Table 4.1: CVN average performance comparing manufactured and simulated specimens.

	Manufactured				**Gleeble Simulated**					
Temp. (°C)	1-L (J)	1-H (J)	2-H (J)	|	3-PWHT1 (J)	3-1080 (J)	3-1120 (J)	3-1140 (J)	3-1160 (J)	3-1200 (J)
-30	24.1 ± 19.4	108.0 ± 47.0	97.6 ± 34.6	|	58.0 ± 18.0	72.0 ± 10.4	66.5 ± 39.2	73.3 ± 28.0	51.5 ± 20.0	33.5 ± 17.7
-45	10.2 ± 6.9	63.1 ± 46.1	82.1 ± 29.7	|	59.3 ± 17.0	78.7 ± 41.1	74.7 ± 46.7	75.3 ± 13.3	60.7 ± 32.6	15.3 ± 2.3

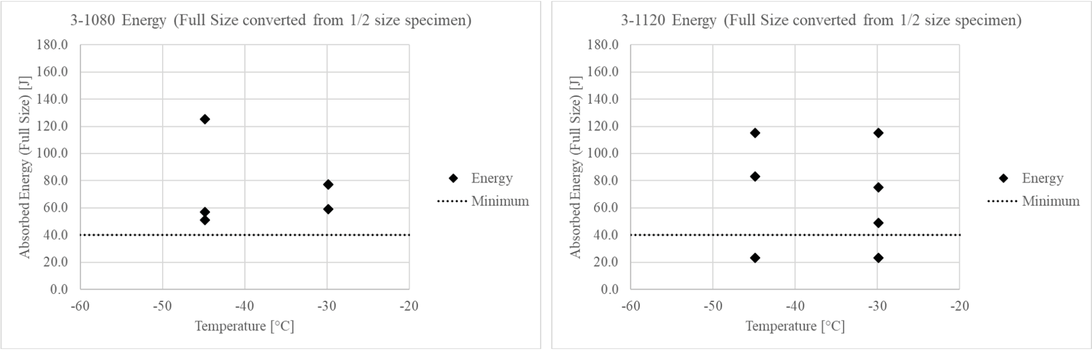

(a) 3-1080. **(b)** 3-1120.

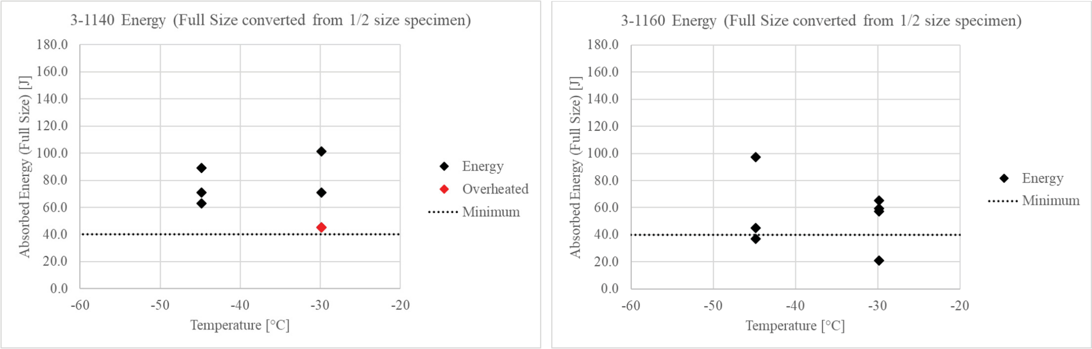

(c) 3-1140. **(d)** 3-1160.

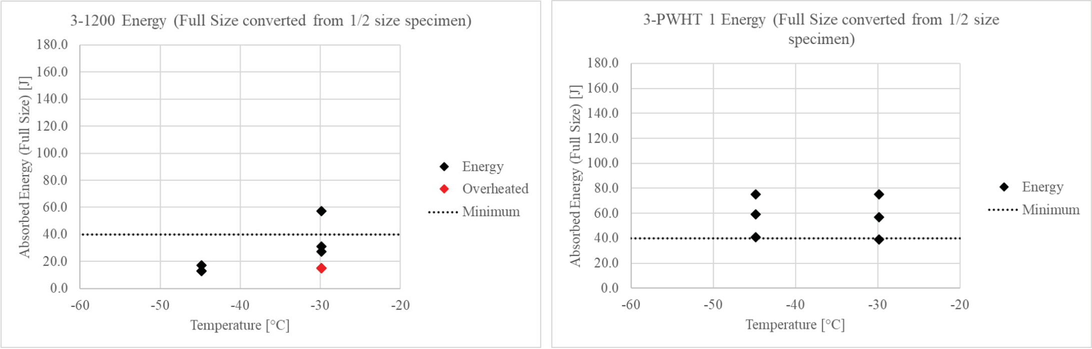

(e) 3-1200. **(f)** 3-PWHT1

Figure 4.1: CVN low-temperature results for simulated PWHT specimens. Overheated specimens experienced momentarily high temperature spikes above the target temperature during the PWHT cycle.

It can be seen that the most promising performance was exhibited by specimens PWHT-ed at lower peak temperatures, with low-temperature toughness performance decreasing at and above 1160 °C. Individual specimens that experienced high-temperature "spikes" during heating area shown as "Overheated"; it is interesting to note that these specimens are ones in which the lowest toughness performance is exhibited (a more detailed accounting of the creation of each specimen is provided in Appendix A). It is also worth noting that the simulation of PWHT 1 using the thermomechanical simulator resulted in performance approximately halfway between the 1-L and 1-H changeovers. Conversations with subject matter experts employed by the manufacturer suggest that the absolute performance of simulated specimens is lower than in manufactured specimens due to the low frequency resistance heating of the Gleeble system, which produces a wider thermal distribution than expected in in-line heating [45]. It is unknown if that is the case for these specimens. It must be noted that due to material and equipment availability, these results represent a very small sample size; more specimens would need to be created and tested to achieve any level of statistical confidence in the comparison of toughness performance.

4.2 Transformation Behaviour

Transformation behaviour was studied through dilatometry for the PWHT cycle used to create the CVN specimens tested as part of the PWHT simulation trial, with an additional peak temperature of 1180 °C. Fig. 4.2 shows the transformation temperatures during both heating and cooling, as well as the predicted austenite-to-ferrite microstructure formation temperatures in equilibrium cooling. Since the cooling rate experienced by the sample, 6.4 °C/s, is quicker than equilibrium, it is expected that true transformation start temperatures are actually lower than predicted based on the chemical composition.

It can be seen that 3-T_P specimens had similar A_c temperatures, which is to be expected as they would have had identical heating rates between the first and second normalizer target temperatures, which were kept constant for this cycle. While the A_c temperatures showed little change with increasing T_P, the same cannot be said for the

A_r temperatures. The A_{r1} temperatures remain relatively consistent around 500 °C. However, as the T_P increases from 1080 °C to 1140 °C, the A_{r3} decreases by as much as 49 °C (718 °C to 669 °C); at higher T_P the A_{r3} becomes relatively stable slightly above the predicted equilibrium bainite start (B_S) temperature (642 °C). However, this general trend is complicated by the observation that 3-1160A and 3-1160B, which were PWHT-ed identically, displayed a wide variation in transformation temperature behaviour. Specimens were unavailable to conduct further tests to establish the variation in this trend, and makes it impossible to determine if 3-1160A is an outlier at this time.

This change in A_{r3} can be explained through the phenomenon of hardenability. Two interrelated influencing factors of hardenability are especially relevant; austenite grain size and soluble chemical composition. As the T_P is increased, the austenite grain size will grow, increasing the hardenability. As well, with increasing temperature there is a greater solubility for precipitate forming elements: of particular interest are the MX type precipitates of (Nb, V, Ti)(C,N); for this material and this PWHT cycle, Nb(C,N) is especially relevant. Nb is known to increase hardenability through the retardation of allotriomorphic ferrite formation [46, 47], and increased soluble carbon and nitrogen also increases the driving force for higher-interstitial-containing displacive transformations such as bainite and martensite. As well, as precipitates are dissolved into austenite, their pinning effect on asutenite grain growth is diminished, resulting in further grain growth [46]. Eq. 4.1 [46, 48] was used to calculate NbC solubility, and Nb in solution in austenite was calculated using Eq. 4.2 [49] and solved using the quadratic equation.

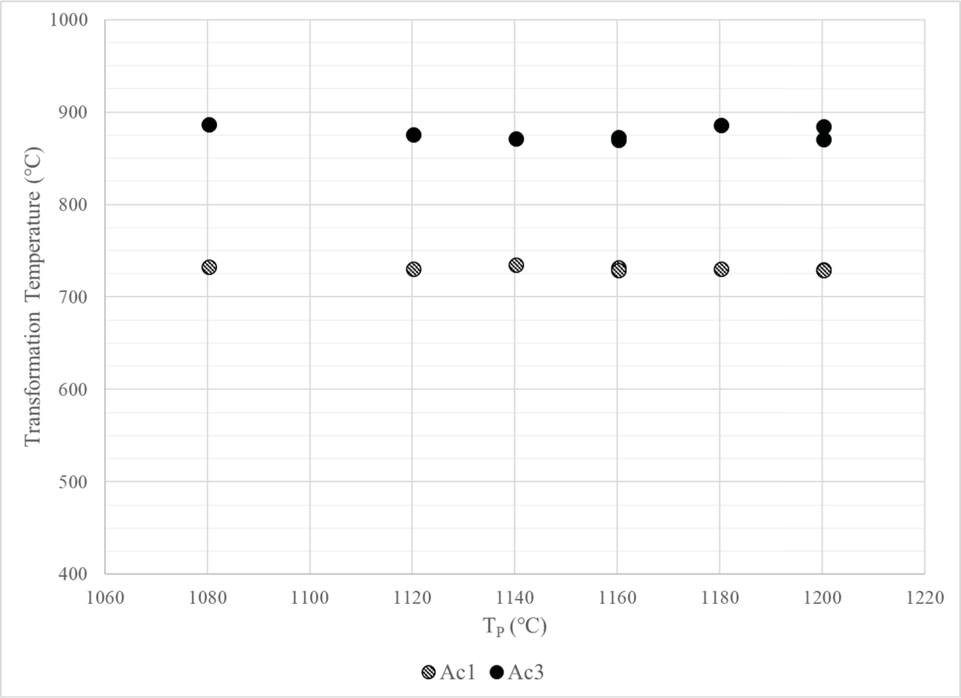

(a) Transformations during heating (A_c).

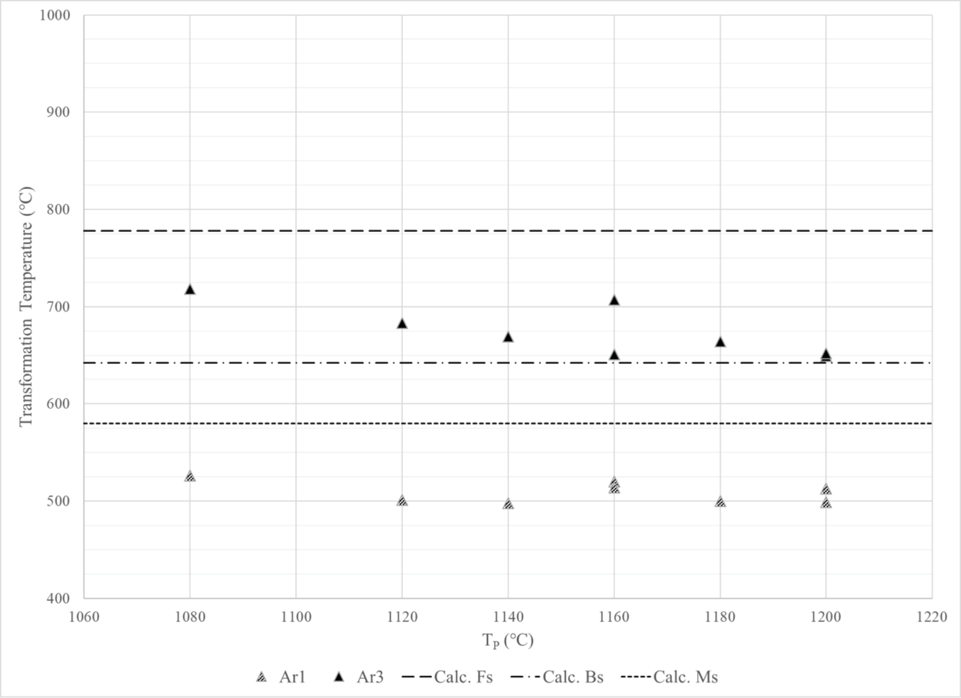

(b) Transformations during cooling (A_r).

Figure 4.2: Transformation during PWHT simulation trial, as measured by dilatometry.

$$log(k_s) = log([Nb][C]^{0.87}) = -\frac{7520}{T} + 3.11 \quad (4.1)$$

$$\frac{A_c}{A_{Nb}} * Nb_{NbC}^2 - (C_{Total} + \frac{A_C}{A_{Nb}} * Nb_{Total}) * Nb_{NbC} + (Nb_{Total} * C_{Total} - k_s) = 0 \quad (4.2)$$

Increases in soluble Nb content with increasing peak temperature from thermodynamic calculations for the material used in the simulation trial are shown in Fig. 4.3. It can be seen in Fig. 4.3 that thermodynamically, at a peak temperature of 1080 °C, 70% of the available Nb, 0.053 wt%, will be soluble in austenite. At peak temperatures slightly below 1140 °C, the Nb will be completely soluble. This is reflected in the observed asymptotic behaviour of the A_{r3} at and above peak temperatures of 1140 °C, where the A_{r3} approaches the equilibrium B_S, and provides a strong argument for soluble Nb retarding allotriomorphic ferrite transformations being responsible for changes in transformation behaviour and subsequent microstructures in the material. The slightly higher A_{r3} of the 3-1140 specimen compared to those with higher peak temperatures can be explained by incomplete dissolution of precipitates due to kinetics and slight increases in soluble interstitial elements at higher peak temperatures. Fig. 4.4 shows that in a similar chemistry material, increasing carbon content will slightly lower the phase transformation start temperatures by stabilizing the austenite (calculation method discussed in *Appendix B*). This agreement between thermodynamic predictions of soluble Nb and C, and observed A_{r3} behaviour, strongly suggests that Nb(C,N) behaviour is a dominant factor in controlling the toughness of ERW welds.

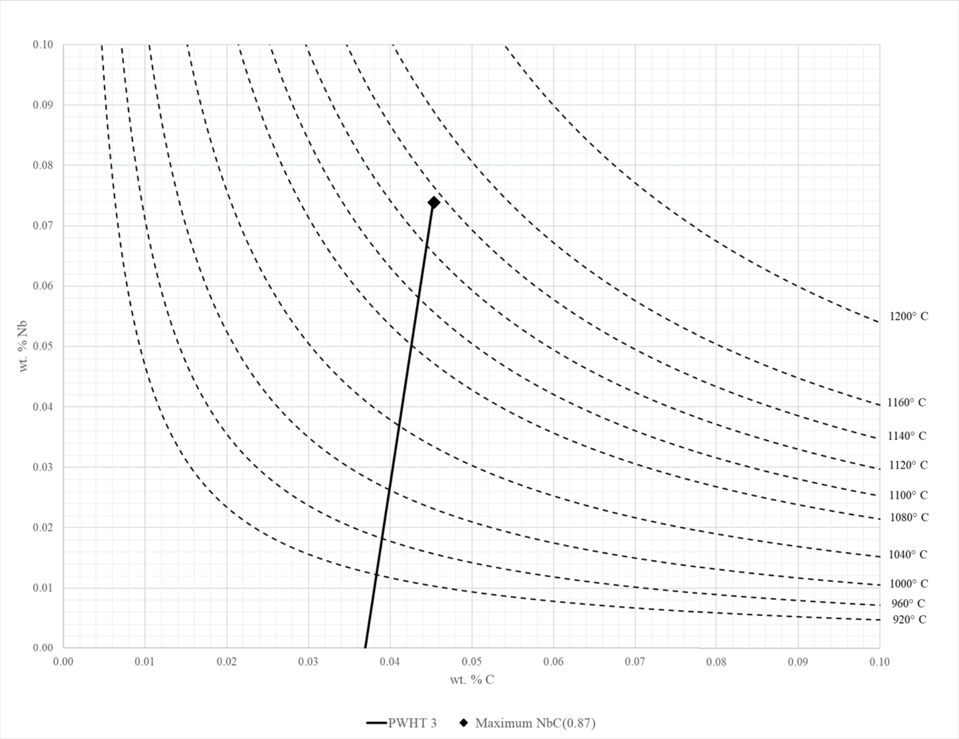

(a) Nb solubility curves.

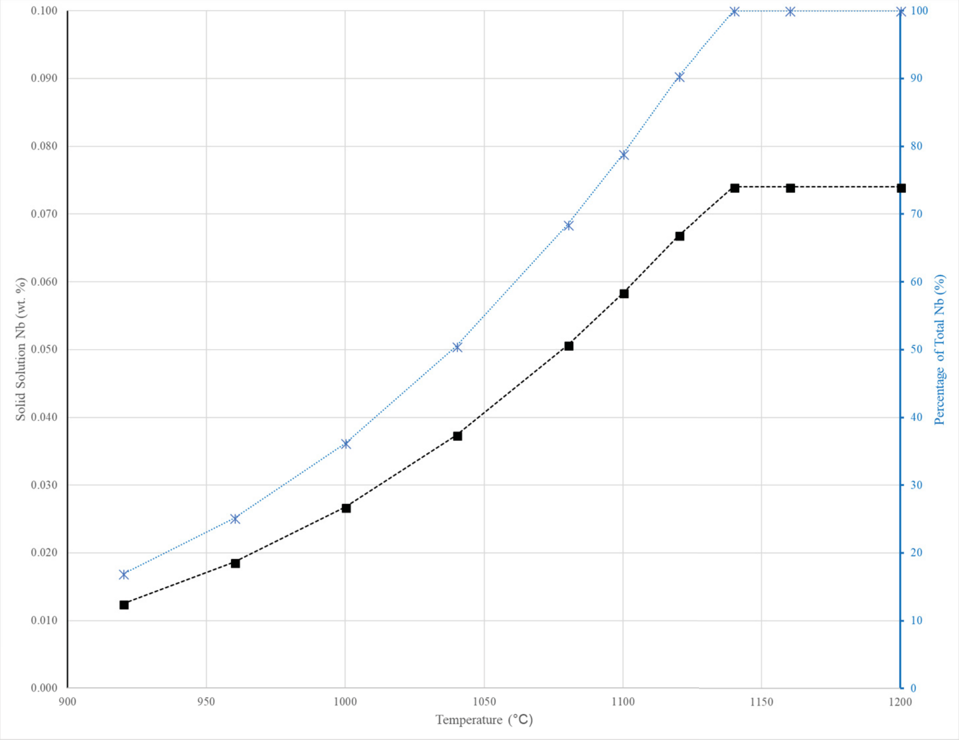

(b) Nb in solid solution in austenite calculated for the material used in PWHT 3.

Figure 4.3: Thermodynamic Nb solubility behaviour.

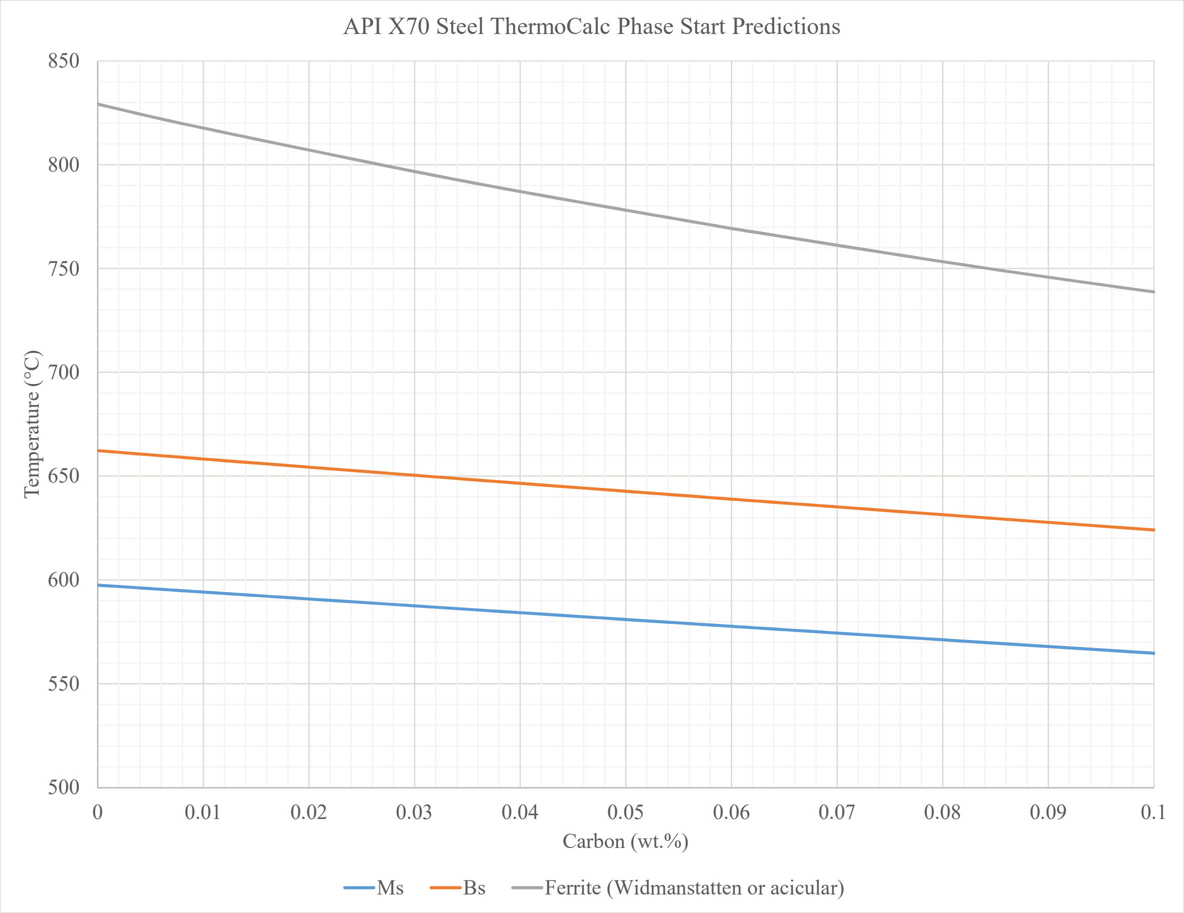

Figure 4.4: Calculated phase transformation start temperatures as function of soluble C.

A more detailed look at the dilatometry curves and their derivatives reveals further evidence to support this hypothesis. Fig. 4.5 shows selected dilatometry data, with the other specimen curves and discussion of details in *Appendix C*. In the derivative of dilation curves, above austenitization smaller phase transformations can be seen; this is attributed to small fractions of niobium carbo-nitride precipitates with various compositions and sizes being dissolved. While only a cursory precipitate analysis was conducted as part of this study in *Chapter 3*, significant work has been done to analyze precipitates in the base material of an X70 steel with somewhat similar chemistry by Chatelier [50].

Chatelier found that the cuboidal precipitates on the order of 1.5 μm were to be various $(\mathrm{Ti}_x\mathrm{Nb}_y\mathrm{Mo}_{1-x-y})$(C,N), where $x + y + z = 1$ [50]. Two main types of smaller spheroidal precipitates were also observed as a significant percentage of the total precipitate mass, where both were predominantly Nb and C: ∼30 wt.% $\mathrm{Nb}_{0.85}\mathrm{Ti}_{0.15}\mathrm{C}$ with a size of ∼15 nm, and ∼50 wt.% $\mathrm{Nb}_{0.68}\mathrm{Mo}_{0.30}\mathrm{Ti}_{0.02}\mathrm{C}$ with a size of ∼4 nm [50]. It can be assumed that similar precipitates may present in the X70 material in this study. In the as-welded ERW material, the likely complete dissolution of the predominantly Nb precipitates followed by extremely rapid cooling which occurs during welding would result in very fine niobium carbide type precipitates, likely even finer than those observed in the base metal by Chatelier. The variation in chemical composition and small precipitate size accounts for the multitude of smaller transformations detected by dilatometry at temperatures below the critical solublity temperature for $\mathrm{NbC}_{0.87}$ in this material. For simplicity, discussion will be limited to NbC precipitates, continuing to assume a $\mathrm{NbC}_{0.87}$ in austenite as found to be most accurate by Nordberg and Aronsson [48].

The circled "peaks" in red for the 3-T_P curves are suspected to be evidence of latent heat during transformations. Due to a changes in heating rate during the normalizer 2 - normalizer 3 interval due to changes in the PWHT cycle, these peaks become more or less obvious; see *Appendix C* for the reasoning. The deviation in slope after this peak is likely due to diffusion driven homogenization of the recently dissolved alloying elements [39]. While it is unknown if the change in heating rate may have exacerbated the slope deviation, this slope change was also observed in constant heating rate dilatometry of a similar X65HIC material by Yan (see *Figure 6.1: Simulation of induction welding on X65HIC base metal. pg. 111.*) [51]. A similar phenomenon was observed in austenitic stainless steel during isothermal heat treatments which dissolved Nb(C,N), where strain levels decreased over time [52]. This is attributed to precipitates causing a larger lattice strain than the elements in solution, leading to a strain relaxation as precipitates are dissolved into the austenitic matrix and the specimen shrinks [52]. This shrinkage in lattice size results in a deviation downwards in the dilation versus temperature curve. This leads to confidence in the evidence for dissolution and homogenization increasing the alloying element content in austenite.

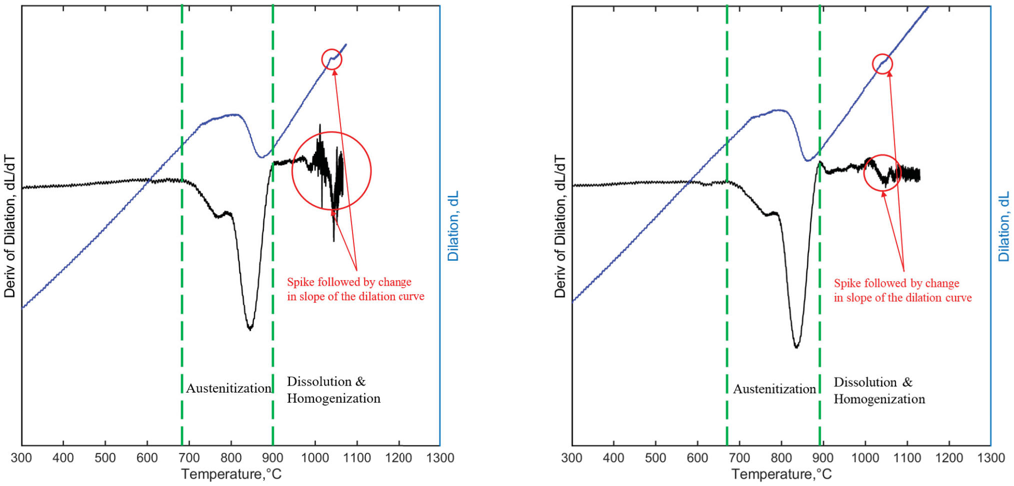

(a) 3-1080.

(b) 3-1160A.

Figure 4.5: Detailed dilatometry analysis of selected specimens.

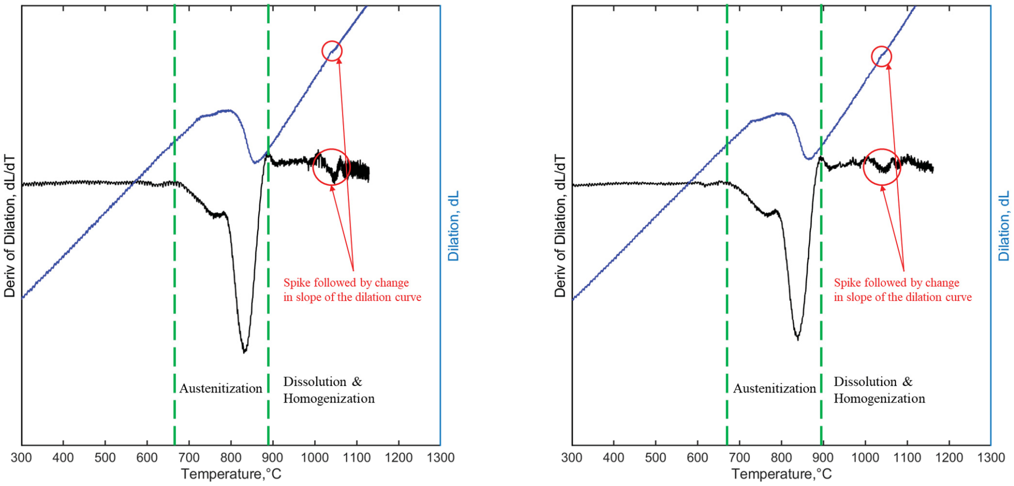

(c) 3-1160B.

(d) 3-1200A.

Figure 4.5: Detailed dilatometry analysis of selected specimens. (cont.)

4.2.1 Microstructural Verification

Figs. 4.6-4.8 show microstructural verification of selected specimens to verify the transformation behaviour previously discussed. 3-1080 exhibits a ferritic microstructure, a mixture of larger and finer grained allotriomorphic ferrite; this structure is quite similar to the microstructure observed in specimen 2-L of the manufactured pipe, with a slightly larger overall grain size. Specimens 3-1160A & 3-1160B are very similar to specimen 1-H from the manufactured pipe with a predominantly fine-grained allotriomorphic bondline and the area adjacent to the bondline being predominantly bainitic with some allotriomorphic ferrite. Again, the simulated specimens appear to have an overall coarser grain size. The main difference between 3-1160A & 3-1160B is the width of the bondline and the fraction of the allotriomorphic ferrite. 3-1160B has a wider bondline area than 3-1160A, and 3-1160A, in line with the observation of a higher A_{r3}, has an increased presence of larger allotriomorphic ferrite. 3-1160B appears to have a larger fraction of finer-grained ferrite in contrast. 3-1200 has a very similar structure to 3-1160B, however the grain size is noticeably larger, the area adjacent to the bondline appears entirely bainitic, and the allotriomorphic ferrite bondline is much narrower. The difference between 3-1160A & 3-1160B is thought to be due to prior structure or chemical composition inhomogeneity along the weld seam, which survived the welding process and thus affected the final transformations after PWHT. 3-1160A would have had a decreased hardenability leading to a increased fraction of allotriomorphic ferrite in the final microstructure of the weld seam.

It appears that increasing the heat input and peak temperature results in a transition from ferritic to bainitic structures in the area adjacent to the bondline, grain growth, and the narrowing of the bondline. This is likely due to increased austenite grain growth, increased soluble alloy content (specifically Nb and C) dissolution and homogenization across the weld seam at high temperatures. The decarburized bondline from welding which produces allotriomorphic ferrite is enriched due to diffusion at higher heat inputs. At increased times or temperatures, this diffusion of higher alloy content would lead to the total conversion of the bondline to a bainitic structure.

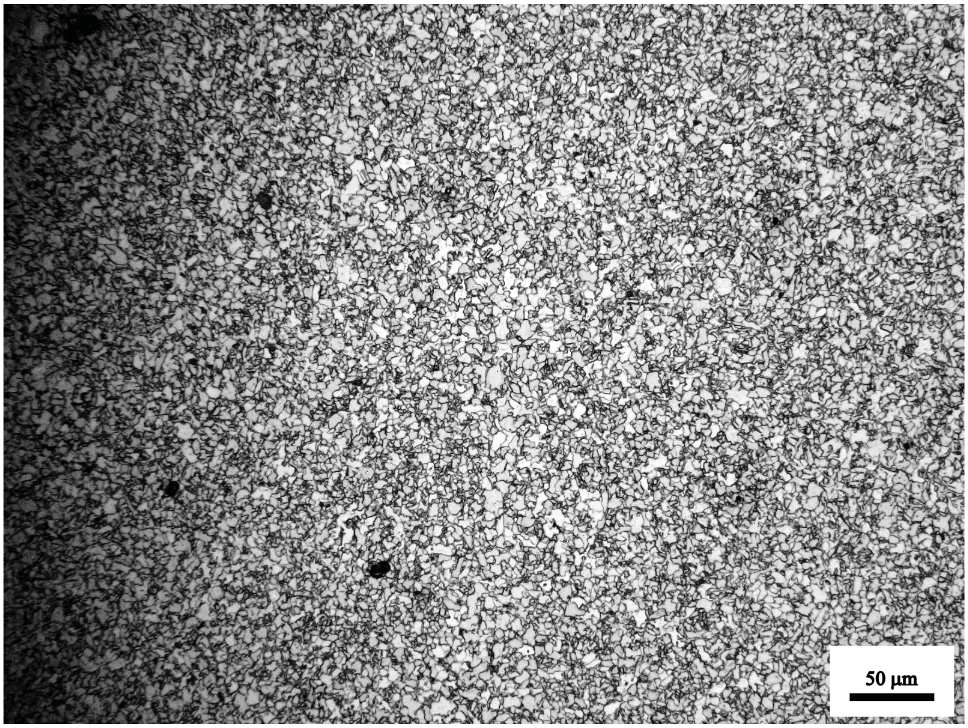

(a) 3-1080 bondline

Figure 4.6: 3-1080 dilatometry sample, optical microscopy.

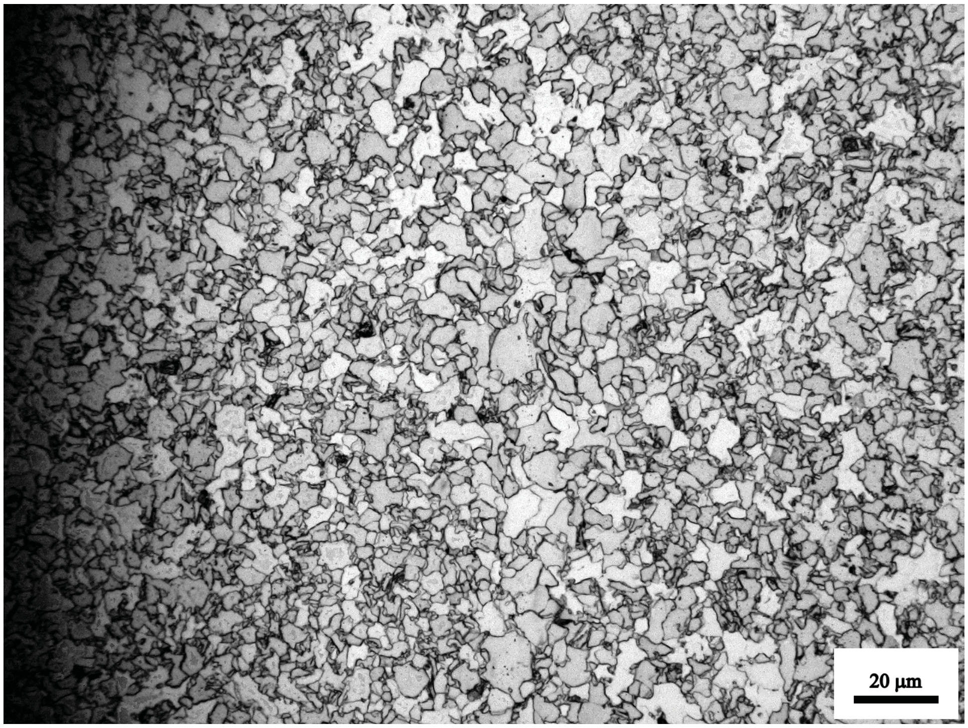

(b) 3-1080 bondline, magnified.

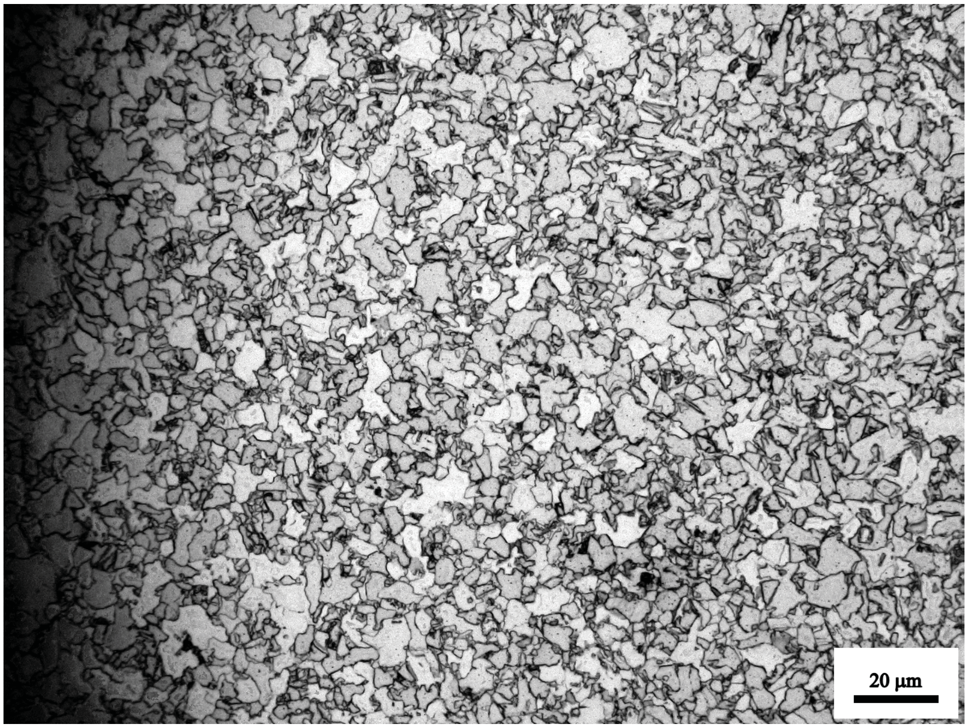

(c) 3-1080 adjacent to bondline, magnified.

Figure 4.6: 3-1080 dilatometry sample, optical microscopy. (cont.)

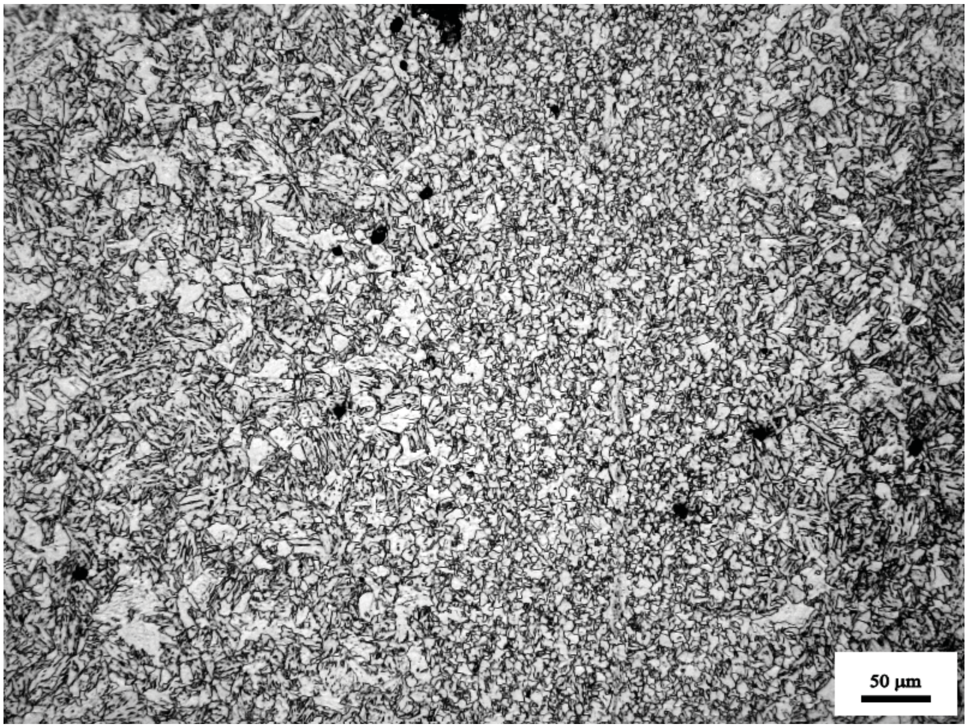

(a) 3-1160A bondline

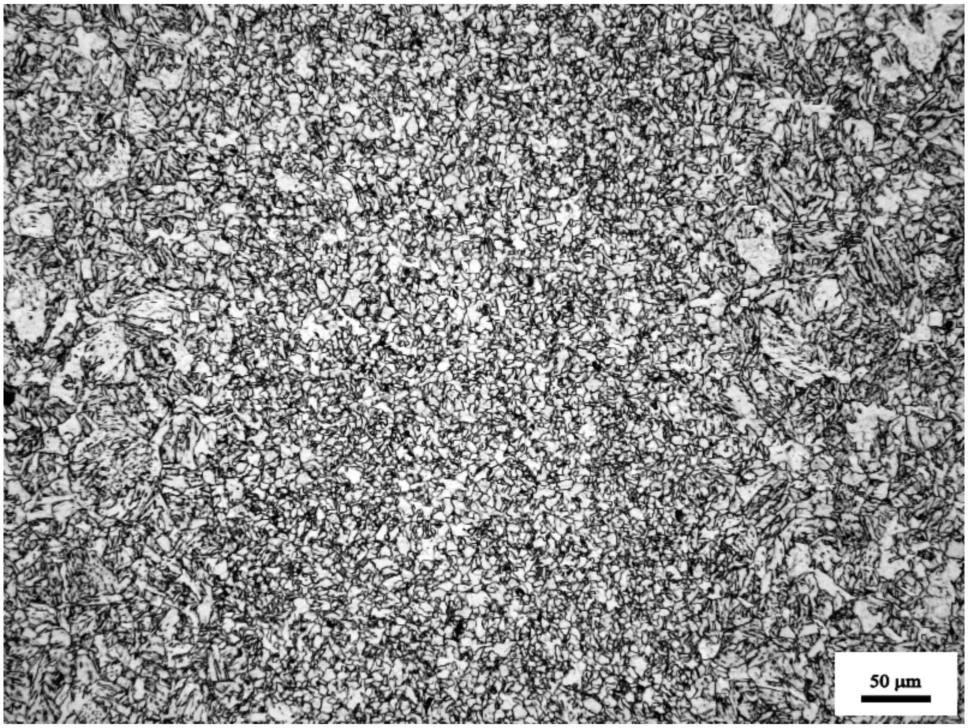

(b) 3-1160B bondline.

Figure 4.7: 3-1160 dilatometry samples, optical microscopy.

(c) 3-1160A adjacent to bondline, magnified.

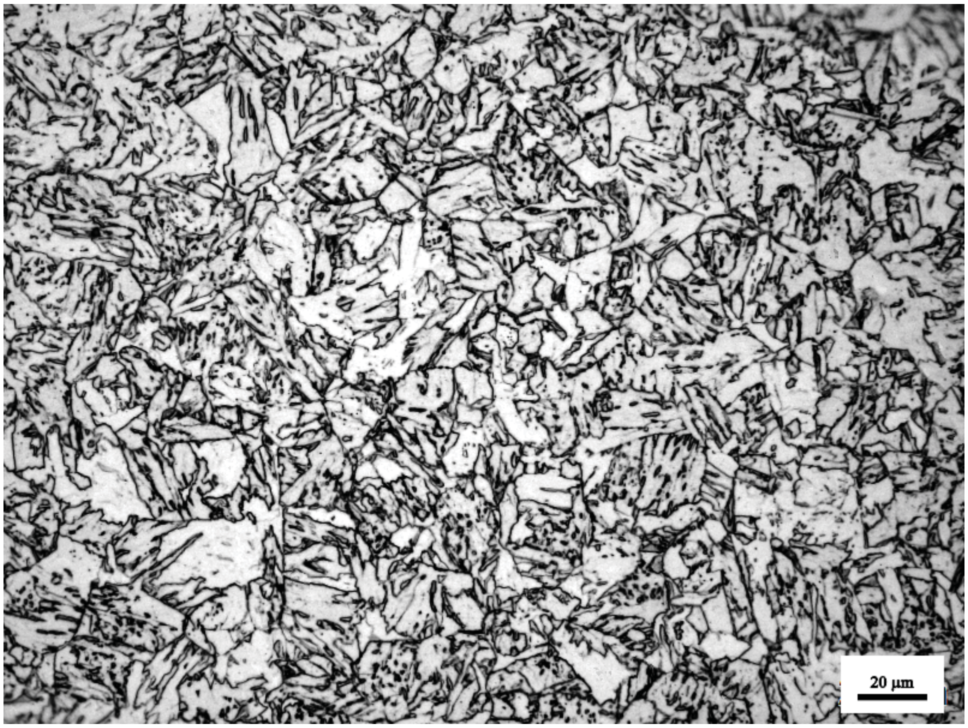

(d) 3-1160B adjacent to bondline, magnified.

Figure 4.7: 3-1160 dilatometry samples, optical microscopy. (cont.)

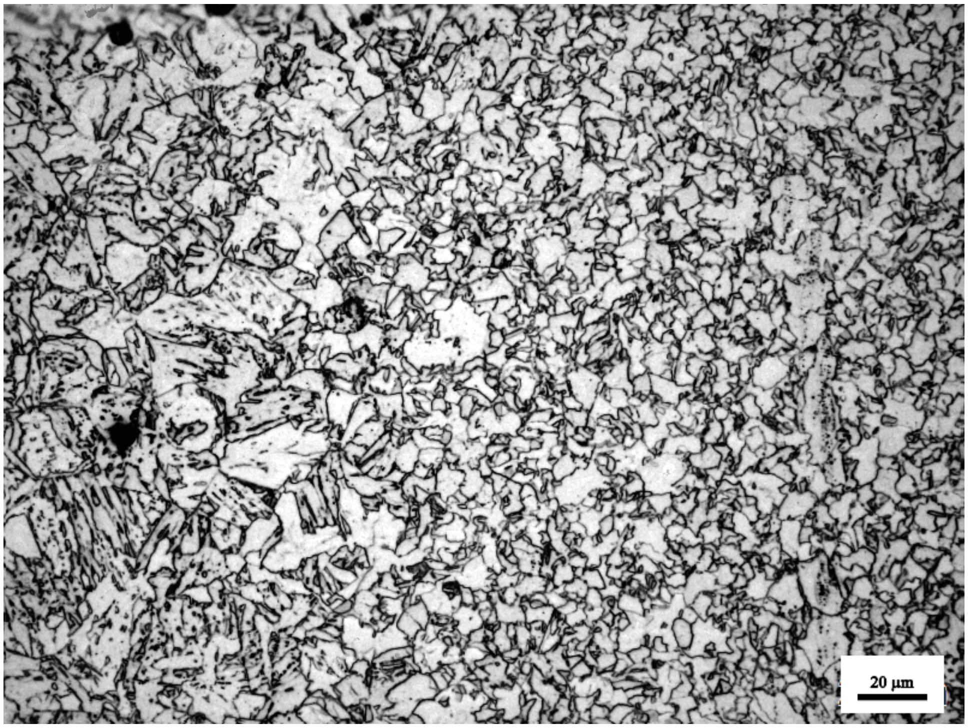

(e) 3-1160A bondline, magnified.

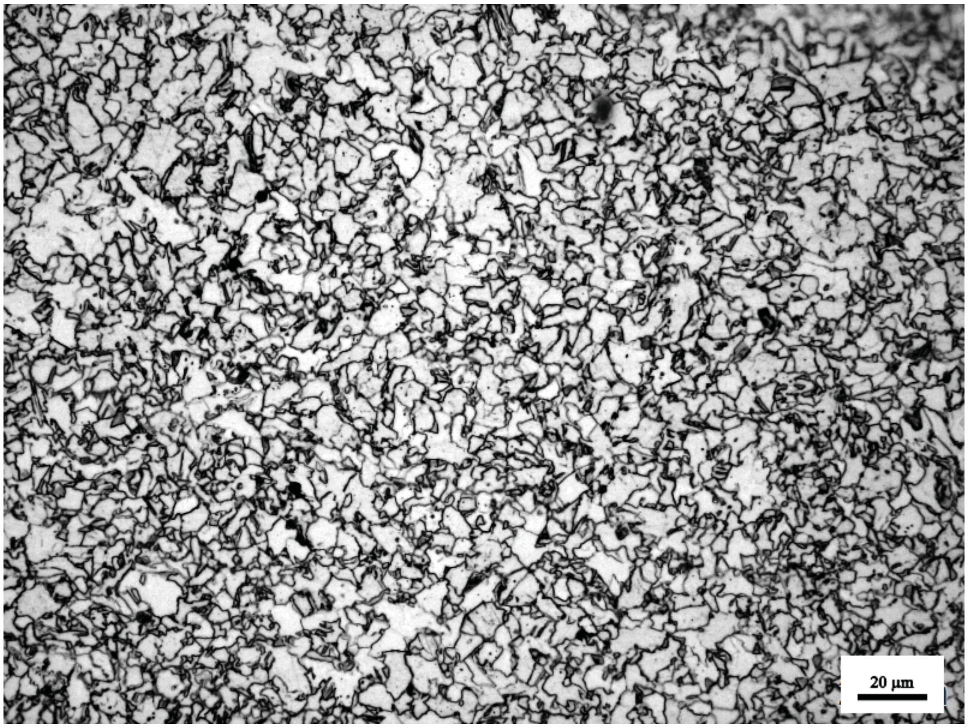

(f) 3-1160B bondline, magnified.

Figure 4.7: 3-1160 dilatometry samples, optical microscopy. (cont.)

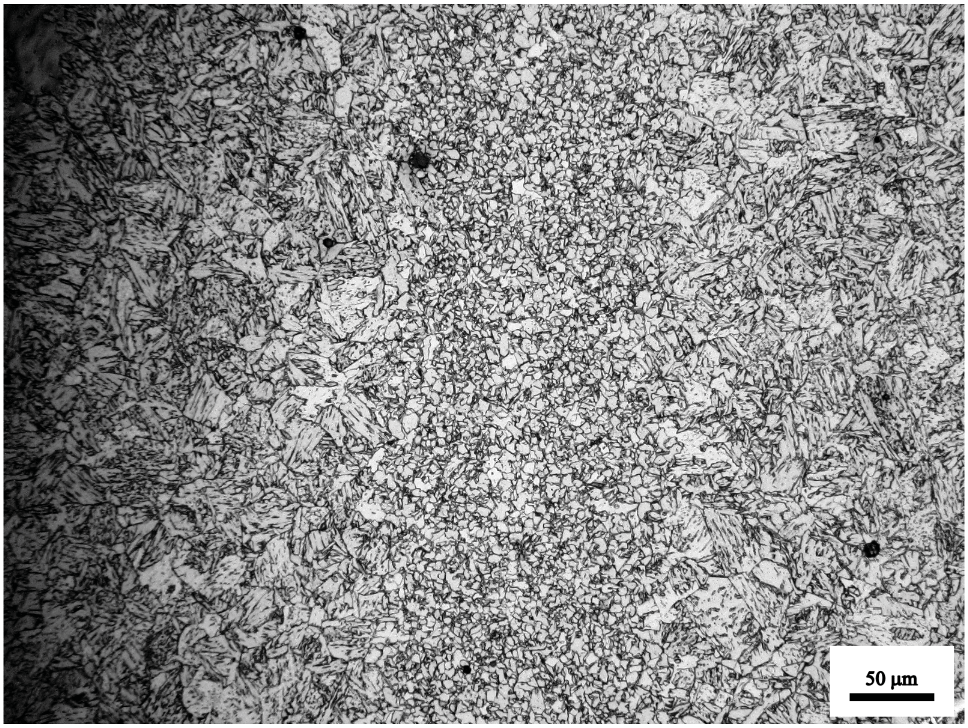

(a) 3-1200 bondline

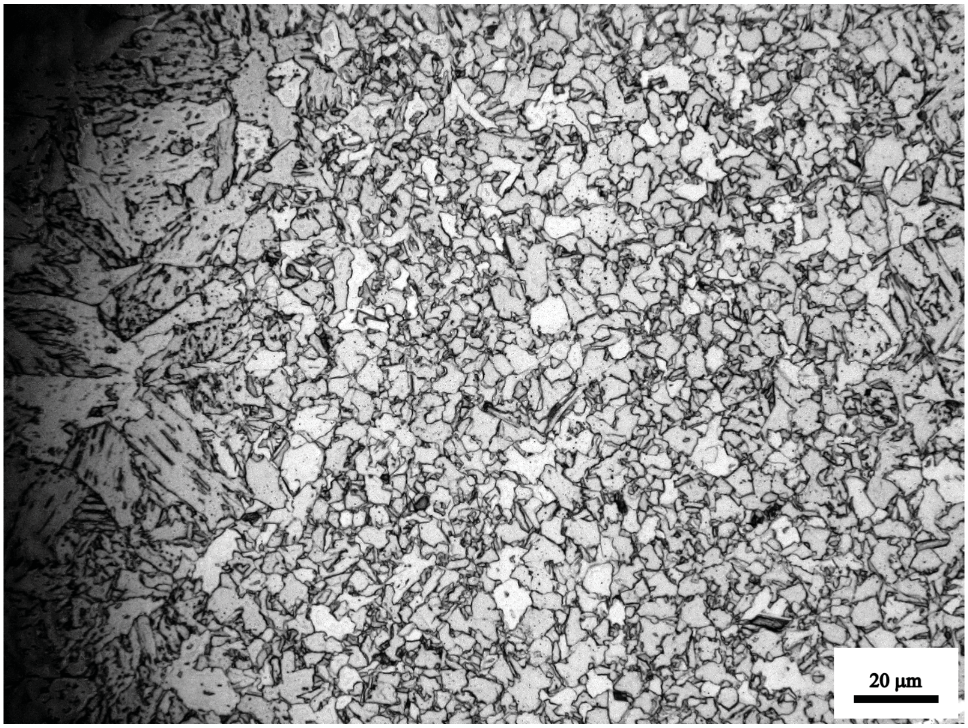

(b) 3-1200 bondline, magnified.

Figure 4.8: 3-1200 dilatometry sample, optical microscopy.

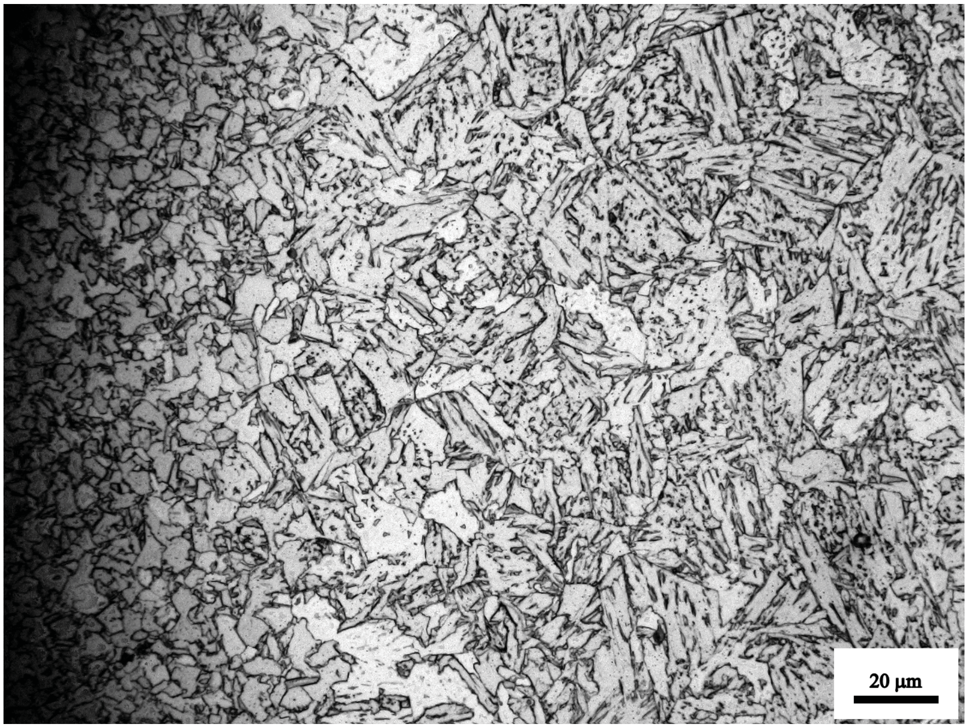

(c) 3-1200 adjacent to bondline, magnified.

Figure 4.8: 3-1200 dilatometry sample, optical microscopy. (cont.)

4.2.2 Influence of Cooling Rate

The PWHT T_P simulation trial specifically fixed the cooling rate to isolate the influence of peak temperature. However, in reality the cooling rate is dependent on the heat input and related to the peak temperature, and will have a strong influence on the resulting transformations and microstructure. In general, an increase in peak temperature will result in a slower cooling rate. In order to briefly investigate the influence of cooling rate on the ERW welding, minimalistic continuous cooling transformation curves were created using dilatometry specimens identical to those used in the PWHT T_P simulation study. PWHT cycles of 3-1080 and 3-1200 were each used with controlled linear cooling rates of 3, 5, and 10 °C/s until 400 °C, after which specimens were allowed to naturally cool. In order to obtain more data sets, the 3-1080 and 3-1200 data sets from the PWHT T_P

simulation trial were also included, with a cooling rate of 6.4 °C/s; the only difference for these data sets is the stop temperature, which was calculated based on the assumptions of line speed and measured travel distances of the manufacturing line. The A_r values measured by dilatometry were plotted to create pseudo CCT diagrams, shown in Fig. 4.9.

When starting from a peak temperature of 1200 °C, the 5, 6.4, & 10 °C/s cooling rates result in a A_{r3} of 650 °C, and the 3 °C/s cooling rate results in a similar but slightly higher A_{r3} of approximately 675 °C. This is consistent with the specimens associated with transformations resulting in bainitic microstructures observed in the PWHT T_P study. In contrast, starting from a peak temperature of 1080 °C it can be seen that at cooling rates of 3 & 5 °C/s transformations begin around an A_{r3} of approximately 750 °C. However, with a cooling rates of 6.4 & 10 °C/s, the A_{r3} shifts downward to 718 & 700 °C respectively. This suggests the existence of a ferrite “nose” at cooling rates greater than 5 °C/s with this peak temperature, and that a different ferritic microstructure may be forming. It is likely the 10 °C/s specimen would have a smaller fraction of allotriomorphic ferrite, and a transition to acicular ferrite or bainite may be seen at higher cooling rates. This exercise demonstrates that both the peak temperature and cooling rate need to be considered to accurately predict the resultant microstructure; for the same base material chemistry, the peak temperature determines the austenite composition, and the cooling rate determines the microstructure that will form.

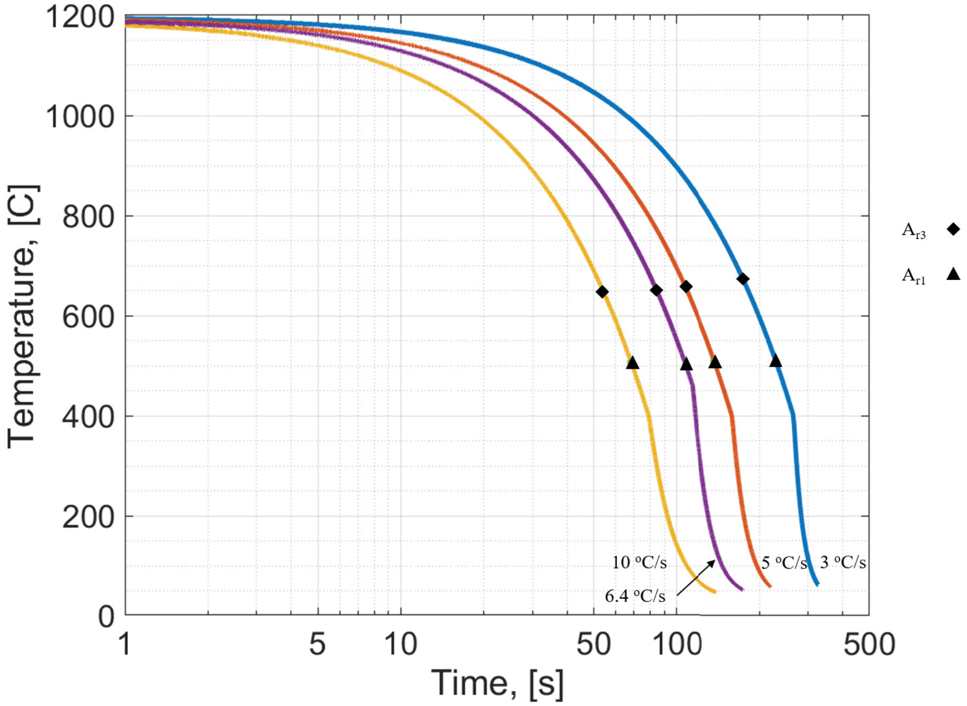

(a) Starting from a peak temperature of 1200 °C.

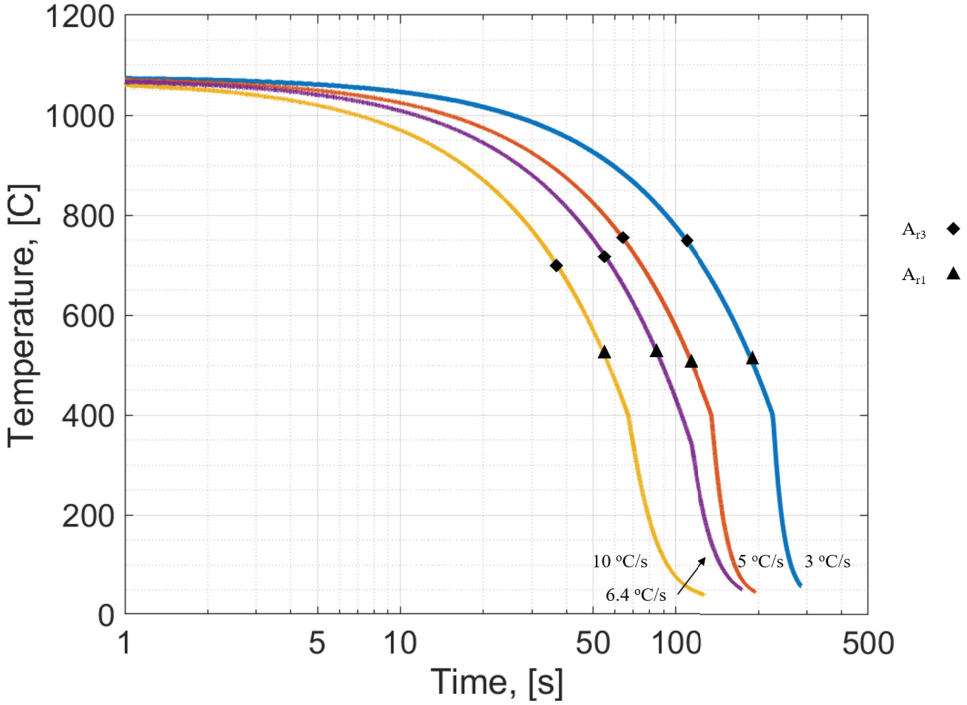

(b) Starting from a peak temperature of 1080 °C.

Figure 4.9: CCT curves showing changes in transformation temperatures on cooling due to changes in peak temperature and cooling rate.

4.3 Summary & Relevance to Manufactured Pipe

Extrapolating the observations of transformations behaviour and subsequent microstructure development provides further insight into the observations made of the manufactured pipes. Of particular value is the expansion of NbC solubility thermodynamics in Fig. 4.10 and the use of dilatometry to acquire evidence of this correlation between Nb(C,N) precipitate solubility and the resulting austenite-to-ferrite transformations. The observations are supported by the theorized effects of carbon and niobium in solid solution in austenite on cooling transformations. Increased substitutional Nb in solid solution retards diffusional ferritic transformations and the increased interstitials of C & N promotes displacive ferritic transformations.

As observed in the PWHT 3 simulated specimens with a T_P that is above the critical temperature for complete solubility (3-1160, 3-1180, & 3-1200), a mainly bainitic microstructure is produced. This behaviour is also observed in the manufactured specimens; the nominal peak temperature of 1-L and 1-H is significantly above the critical temperature predicted for complete solubility (∼1100 °C), and produced the expected predominantly bainitic microstructure in the weld seam. Generally, with the exception of 1-H, these specimens were observed to have poorer low-temperature toughness performance. A similar trend can be seen with the specimens that experience T_P that are below the critical temperature for complete solubility, however in this case an allotriomorphic ferrite is produced. This is observed in the A_{r3} temperatures (and microstructures of selected specimens) of 3-1080, 3-1120, the CCT specimens starting from a T_P of 1080 °C, and specimen 2-H, which has peak temperature less than the critical temperature for complete solubility calculated based on the material composition for PWHT 2. This can be attributed to the lower solubility of Nb and C. In general, the specimens with a T_P that is below the critical temperature for complete solubility showed higher low-temperature toughness performance.

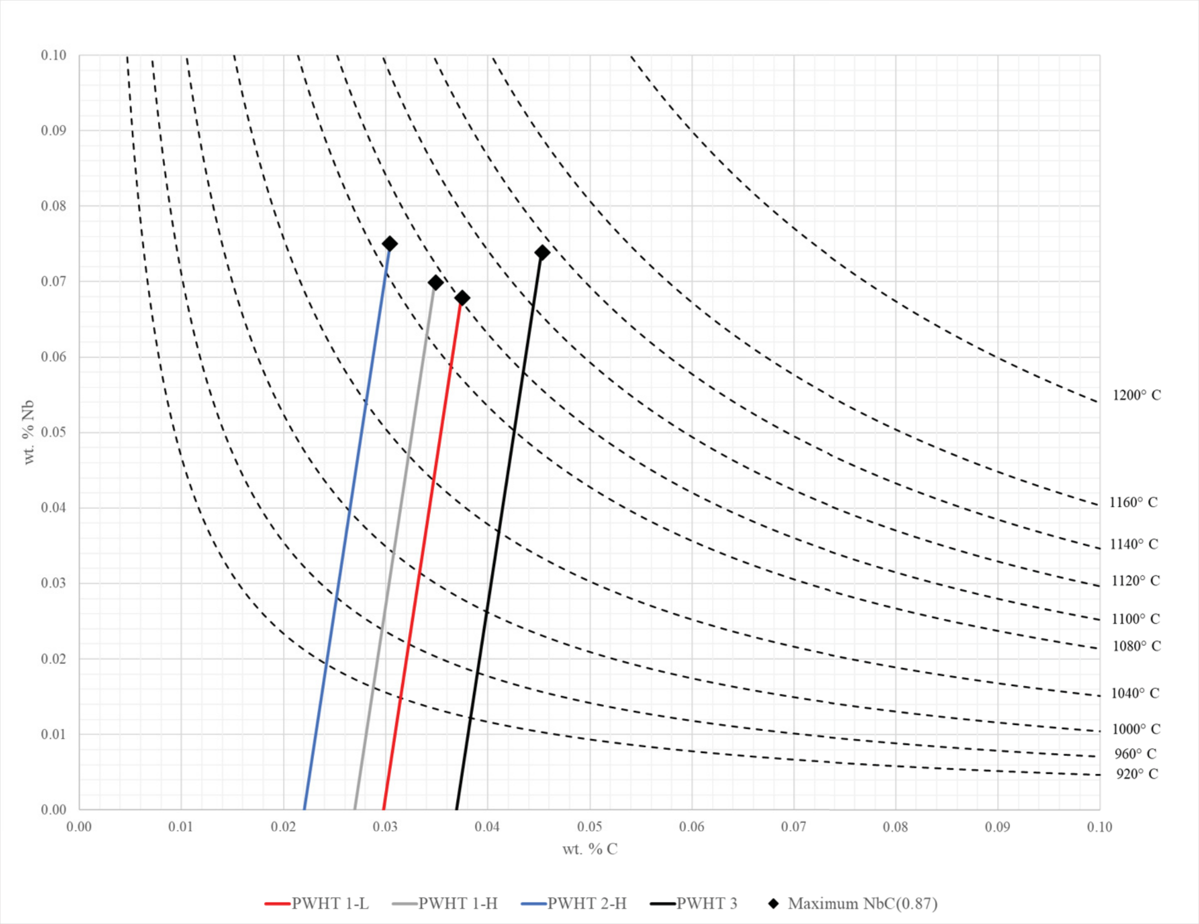

Figure 4.10: $NbC_{0.87}$ solubility for all specimens.

In combination with the rough CCT diagrams, this provides some confidence in the hypothesis that the soft zone in specimen 1-L may be related to local inhomogeneities resulting in a dual phase microstructure. The PWHT T_P study prove that variations in chemical composition will produce different microstructures when subjected to similar cooling rates; the CCTs prove that materials with the same chemical composition may shift to different microstructures when subjected to different cooling rates. Areas with a lower alloy content would behave similar to the CCT with a starting T_P of 1080 °C and would be likely first transform to allotriomorphic ferrite. This diffusional transformation would reject alloying elements into the surrounding austenite, especially C. As the austenite alloy content increased, the remaining enriched austenite would behave more like the CCT with a starting T_P of 1200 °C.

In comparison to the PWHT cycles used for the CCT creation, PWHT 1 has a relatively low normalizer 2 temperature (below significant NbC dissolution), and an intermediate T_P, still significantly higher than the critical temperature for Nb solubility. It is possible that it exists in a state where the majority of NbC precipitates are dissolved into austenite but that homogenization may not have been fully achieved due to the kinetics of diffusion, especially of larger atoms such as Nb. As both 1-H and 1-L have similar chemistry and followed the same nominal heat treatment, their high-temperature austenite composition is likely very similar. Thus we look at cooling rate; since 1-H is approximately 2.5 mm thicker than 1-L, this extra material may act as a heat sink, increasing the cooling rate and resulting in a fully bainitic structure with reasonably high toughness values. Acicular ferrite may not form due to the lack of precipitates and the cleanliness of the steel. An appropriate comparison may be the 3-1160 CVN specimens, which performed reasonably well yet would have a mostly bainitic structure surrounding the allotriomorphic bondline. In contrast, 1-L, as a thinner pipe, may cool somewhat slower when subjected to similar thermal cycles and result in a small fraction of allotriomorphic ferrite. This is merely a hypothesis and additional study as well as a more accurate understanding of the manufacturing parameters used for both changeovers is required. Expansions on current work to investigate this and other phenomena is outlined in *Future Work* in *Chapter 5*.

Another factor which was not discussed but inherently plays a role is the prior austenite grain size development after austenitization. Discussion was omitted as prior austenite grain sizes were not observed in the current study. Generally the higher the heat input, the larger the austenite grain size. However, this can be influenced by chemical composition and precipitate size and distribution due to grain boundary chemistry and precipitate pinning effects. As these are relatively unknown, austenite grain size and MX precipitate pinning cannot be discussed in the current study beyond acknowledging that these would play a role. This deficiency is addressed in *Future Work* in *Chapter 5*.

Chapter 5

Summary and Future Work

5.1 Summary and Conclusions

In this study, weld seams of industrially manufactured electric resistance welded API X70 pipe were investigated with the intent to identify metallurgical explanations for the respective low-temperature toughness performance. Two nominal post-weld heat treatments (PWHT) were investigated; PWHT 1 with a low-toughness changeover and a high-toughness changeover, and PWHT 2 changoever. PWHT 2 was reported to a have more consistent high-toughness performance at low-temperatures, and performed slightly better than the high toughness changeover from PWHT 1 at -45 °C. Standard mechanical property and both standard and advanced metallographic characterization techniques, including electron back-scattered diffraction, were used to investigate the manufactured specimens. Since little is known about the differences in prior material condition or manufacturing parameters used to create each of the three changeovers beyond the nominal settings, a controlled study was also undertaken in an attempt to isolate the effect of PWHT cycle peak temperature on subsequent microstructure and toughness performance. Two main differences were known between PWHT 1 and PWHT 2: the target temperature at the second normalizer, and the target temperature at the third normalizer which is the peak temperature of the PWHT cycle. It was decided that the peak temperature was more critical to study, and as PWHT 2 showed the best low-temperature toughness performance, a Gleeble thermomechanical simulator was used to simulate PWHT 2 on as-manufactured weld seams from the same section of pipe only changing the peak temperature of the cycle. Charpy V-notch specimens were created to investigate toughness, and dilatometry and optical microscopy were used to investigate the material transformation response and subsequent microstructure. Limited continuous cooling transformation experiments also allowed for a small amount of insight into the influence of cooling rate.

5.1.1 Conclusions

- In depth characterization revealed that PWHT 1 produced a weld seam with a predominantly coarser bainitic area adjacent to an allotriomorphic ferrite bondline, while PWHT 2 produced a more homogeneous allotriomorphic ferrite across the entire weld seam.

- Higher toughness specimens were observed to have a finer grain size, larger fraction of high angle grain boundaries (HAGBs), minimized M-A constituents and lower strain at the bondline. Crystallographic texture was not observed to be a significant factor in the investigated specimens.

- A correlation between peak temperature, toughness performance, transformation temperatures, and microstructures was observed. This correlation was linked to the role of niobium and carbon in the microalloyed steel through thermodynamic calculations, the observed retardation of allotriomorphic ferrite formation and lowering of austenite-to-ferrite transformation temperatures with increasing niobium carbide solubility. Post-weld heat treatments which exceeded the critical temperature for complete precipitate solubility were found to result in a predominantly coarse-grained, bainitic microstructure inhomogeneous with the fine-grained, equiaxed allotriomorphic bondline and less desirable low-temperature toughness performance. Post-weld heat treatments below the critical temperature for complete precipitate solubility were found to result in a a homogeneous fine-grained, equiaxed allotriomorphic ferrite weld seam and improved low-temperature toughness performance.

5.1.2 Hypotheses to be Verified

- The poor toughness changeover from PWHT 1 was discovered to have a “soft-zone” within 100-150 μm of the bondline. Similar soft-zones in creep materials have been attributed to preferential cracking under creep loading conditions [44]; it is thought the presence of a soft-zone in this ERW material may explain the significantly worse performance of the low-toughness PWHT 1 changeover. A hypothesis is proposed whereby the soft-zone in the low-toughness PWHT 1 changeover is due to local chemical composition inhomogeneities from prior welded microstructure and a slower cooling rate than the high toughness changeover. This stems from a the high toughness specimen having a thicker pipe wall which acts as a more effective heat sink, increasing the effective cooling rate. Further work is required to establish the validity of this hypothesis.

- Low-temperature toughness performance is suspected to increase when complete niobium carbo-nitride precipitate dissolution does not occur; this is best accomplished by restricting the peak temperature of the PWHT below the critical temperature for complete precipitate solubility in austenite based on the material composition. This is based on the role of MX type precipitates as austenite grain refiners, niobium in solution acting to suppress diffusional ferritic transformations, and carbon and nitrogen in solution promoting displacive bainitic transformations.

The hypothesized role of the MX precipitate formers, (Ti,Nb,V)(C,N), can be summarized as (Fig.):

- As MX precipitates - prevent austenite grain growth, causing grain refinement.
- In solution:
    - M elements - reconstructive transformations require a diffusional redistribition and rejection of alloying elements. Increased M concentrations block diffusion and suppress ferrite formation. Displacive transformation are relatively unaffected.
    - X elements - increase hardenability and promote displacive transformations.

Further work is required to validate this hypothesis.

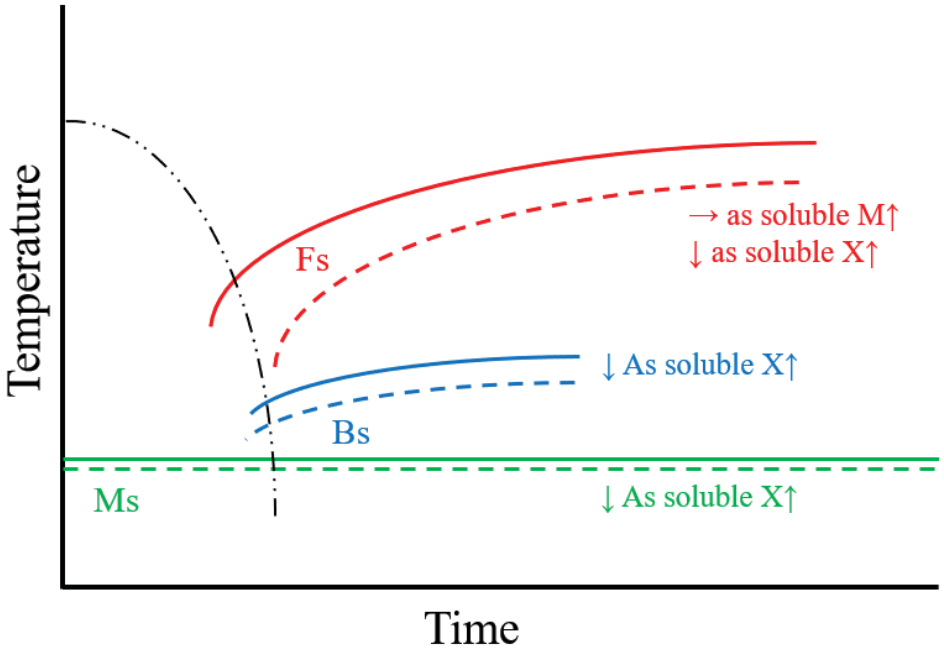

Figure 5.1: Schematic CCT showing hypothesized influence of MX precipitate forming elements.

5.2 Future Work

Over the course of this study, several opportunities to increase the scope of the research, leverage learnings to other applications, and expand the body of knowledge were identified. The sensitivity of the final product to the thermal mechanical controlled processing history starting from the casting of the steel slabs, through rolling, forming, welding, and post-weld heat treating results in a great deal of complexity, metallurgically speaking. As a significant portion of this work was based on industrial practices of which only an incomplete history is known, independent verification of assumptions becomes critical, further increasing the work required. Based on the completed study, three linked areas where additional research would be highly beneficial are described below.

1. **The mechanism and influence of the "soft-zone" in PWHT 1 low-toughness material.**

   A focused study on the "soft-zone", dual phase microstructure adjacent to the bondline in the low-toughness sample from PWHT 1 should be conducted. This study should follow the methodology of Wang *et al.* [44], and be applied to both the high and low toughness specimens from PWHT 1 for comparison. First, fractured specimens should be obtained: fractography, the path of crack propagation, relative to the bondline, and thorough hardness testing should be conducted to determine whether the soft-zone is responsible for the degraded toughness performance. Advanced characterization techniques should be used at the base metal, as-welded, and PWHT-ed material conditions to determine the formation mechanism of the soft-zone. If possible, this should be linked to known processing history to determine why the soft-zone is developing in one changeover and not another. If material is unavailable, further characterization may be able to provide hypotheses for soft-zone formation, and these hypotheses could then be tested through simulated specimens on a Gleeble thermomechanical simulator to attempt to replicate this phenomenon in a controlled environment.

2. **The influence of niobium and its precipitates during ERW welding and PWHT.**

   The present study found correlation between the potential for soluble Nb, C, and N content, precipitate behaviour, and subsequent microstructure formation and toughness performance. However, this correlation is merely based on the known behaviour of Nb in other works, observed transformation temperatures, and thermodynamic calculations. The work in *Chapter 4* should be expanded, and include the analysis of precipitation behavior. Work by Bhattacharya [47] has investigated the role of Nb in in the heat-affected zone of microalloyed steels, and parallels can be drawn to this work as well as work by Yan and Bhadeshia [46]; however, what is unknown is the role of the additional PWHT in ERW welding as well as the effect of the prior condition of the material coming from the welding operation, which will also affect the ratio of soluble Nb and NbC, as well as the precipitates size and distribution in the material. Additional proof for this theory should be investigated using (1) Auger characterization, (2) matrix dissolution and dissolved soluble Nb measurements, and (3) direct observation of Nb(CN) using transmission electron microscopy (TEM). As well, Bhattacharya [47] made observations of the interrelationships between prior austenite grain size, Nb content and NbC precipitates, and the subsequent microstructure developed on cooling. The expansion of the current study to include prior austenite observations would be very useful, and help clarify the holistic role of Nb, C, & N as both precipitates and solute elements. As well, Bhattacharya's study [47] did not investigate the toughness aspect of material performance; this is an area that could be very useful in practical applications. A study of Nb in solute and Nb in precipitates should be conducted at three conditions: PWHT below the critical temperature for complete Nb(CN) solubility, PWHT at the critical temperature for complete Nb(CN) solubility, and PWHT above the critical temperature for complete Nb(CN) solubility. This information should be linked to more thorough thermodynamic and kinetic calculations to better understand the phase transformations during welding and heat treatment.

3. **Toughness testing improvements.**

   The current study would benefit from the usage of more accurate and more applicable toughness testing methodologies if specimens can be obtained. Charpy V-notch impact testing, despite wide usage and simplicity, is not particularly accurate. As well, other techniques, such as single-edge notched bend testing or single-edge notched tension testing are more applicable to material resistance to crack propagation, which is more more importance to pipeline applications than the Charpy impact testing, which is more applicable for material resistant to crack initiation.

Bibliography

[1] American Petroleum Institute. Line pipe. Technical Report Specification 5L, Forty-Sixth Edition, April, 2018. Accessed June 13, 2018.

[2] CSA Group. Steel pipe. Technical Report Z245.1-18, Tenth Edition, Canadian Standards Association, March, 2018. Accessed June 13, 2018.

[3] M. Kimchi. *ASM Handbook Volume 6A: High-Frequency Welding*. ASM International, 2011. Accessed April 9, 2017.

[4] P. Yan, Ö. E. Güngör, P. Thibaux, M. Liebeherr, and H.K.D.H. Bhadeshia. Tackling the toughness of steel pipes produced by high frequency induction welding and heat-treatment. *Materials Science and Engineering: A*, 528(29-30):8492 – 8499, 2011. Accessed April 9, 2017.

[5] J. F. Kiefner and K. M. Kolovich. Final report on erw and flash weld seam failures to battelle. Technical Report Agreement No. DTPH56-11-T-000003 (Final Report No. 12-139), September, 2012. Accessed April 9, 2017.

[6] B. N. Leis and J. B. Nestleroth. Battelle's experience with erw and flash weld seam failures: Causes and implications. Technical Report Contract No. DTPH56-11-T-000003 (Battelle Project No. G006084), September, 2012. Accessed April 9, 2017.

[7] PHMSA. Comprehensive study to understand longitudinal erw seam failures. `https://primis.phmsa.dot.gov/matrix/PrjHome.rdm?prj=390`. Accessed April 9, 2017.

[8] B. N. Leis, B. A. Young, J. F. Kiefner, J. B. Nestleroth, J. A. Beavers, G. T. Quickel, and C. S. Brossia. Final summary report and recommendations for the comprehensive study to understand longitudinal erw seam failures – phase one. Technical Report Contract No. DTPH56-11-T-000003 (Battelle Project No. G006084), Battelle, October, 2013. Accessed April 9, 2017.

[9] Greg T. Quickel. Final report - subtask 2.3: Characterization of the toughness of pipe containing erw seam defects - prepared for the pipeline hazardous material safety administration. Technical Report TAOUS813GTQU (PP017533), Det Norske Veritas (U.S.A.), Inc., May 2013. Accessed April 9, 2017.

[10] Bruce A. Young, Steve Nanney, Brian Leis, and Jennifer M. Smith. Overview of a comprehensive study to understand longitudinal erw seam failures. volume 2, page V002T06A050, 2014. Accessed April 9, 2017.

[11] S. Suzuki and T. Takamura. The formation mechanism of white line in welded joints of erw steel pipes. *Tetsu-to-Hagane*, 70(10):1467–1473, 1984.

[12] B. C. De Cooman and K. Findley. *Introduction to Mechanical Behaviour of Steel*, chapter 13: Fracture. Association for Iron and Steel Technology, Warrendale, PA, U.S.A., 1 edition, 2017.

[13] ASTM International. Standard test methods and definitions for mechanical testing of steel products. Technical Report A370-17a, December 2017. Accessed June 18, 2018.

[14] Xu Su, Andrew Laver, Jim Gianetto, Jie Liang, William R. Tyson, and Shinya (Matt) Matsuno. Charpy toughness of erw seam welds. *Journal of Pipeline Engineering*, 16(3):149 – 167, 2017.

[15] I. Berlanga, R. Bruna, T. Perez, and I. Garcia. Advanced microstructural characterization of a x-70 microalloyed steel for the oil and gas industry. In *OTC Brasil*. Offshore Technology Conference, 2015. Accessed April 9, 2017.

[16] Hiroshi Nakata, Chikara Kami, and Nobuyuki Mathuo. Development of api x80 grade electric resistance welding line pipe with excellent low temperature toughness. *JFE Technical Report*, (12):27–31, 2008. Acessed April 9, 2017.

[17] Shunsuke Toyoda, Sota Goto, Takatoshi Okabe, Hideto Kimura, Satoshi Igi, Yutaka Matsui, Satoru Yabumoto, Akio Sato, Masahito Suzuki, and Tomohiro Inoue. Metallugical design and performance of erw linepipe with high-quality weld seam suitable for extra-low-temperature services. volume 3, pages 439–446, 2012. Acessed April 9. 2017.

[18] Shunsuke Toyoda, Sota Goto, Takatoshi Okabe, Hideto Kimura, and Satoshi Igi. Metallurgical design and performance of high-frequency electric resistance welded linepipe with high-quality weld seam suitable for extra-low-temperature services. *Journal of Offshore Mechanics and Arctic Engineering*, 137(3), 2015. Acessed April 9. 2017.

[19] HU Hong, CM Kim, JB Lee, et al. Fatigue behavior of electric resistance welded seams in api-x70 steel. In *The Fifteenth International Offshore and Polar Engineering Conference*. International Society of Offshore and Polar Engineers, 2005. Acessed April 9. 2017.

[20] Sang Yong Shin, Kyungshik Oh, Ki Bong Kang, and Sunghak Lee. Effects of complex oxides on charpy impact properties of heat affected zones of two api x70 linepipe steels. *ISIJ international*, 49(8):1191–1199, 2009. Acessed April 9, 2017.

[21] J. B. Wiskel. Grain size strengthening and grain size plastic instability failure. Lecture notes from MAT E 689: Advanced Processing of Microalloyed Steels, September 2016.

[22] W. Chen. Topic 6: Fracture control. Lecture notes from MAT E 662: Fracture of Materials, November 2017.

[23] H. K. D. H. Bhadeshia and R. W. K. Honeycombe. *Steels: Microstructure and Properties*, chapter 3: Iron-Carbon Equilibrium and Plain Carbon Steels. Elsevier Ltd., Oxford, UK, 3 edition, 2006.

[24] B. Verlinden, J. Driver, I. Samajdar, and R. D. Doherty. *Thermo-Mechanical Processing of Metallic Materials*, chapter 7: Phase Transformations. Pergamon Materials Series. Elsevier Ltd., Oxford, UK, 1 edition, 2007. Series Editor: R. W. Cahn.

[25] S. Kou. *Welding Metallurgy*, chapter 9: Post-Solidification Phase Transformations. John Wiley and Sons, Inc., Oxford, UK, 2 edition, 2003.

[26] H. K. D. H. Bhadeshia and R. W. K. Honeycombe. *Steels: Microstructure and Properties*, chapter 5: Formation of Martensite. Elsevier Ltd., Oxford, UK, 3 edition, 2006.

[27] H. K. D. H. Bhadeshia and R. W. K. Honeycombe. *Steels: Microstructure and Properties*, chapter 6: The Bainite Reaction. Elsevier Ltd., Oxford, UK, 3 edition, 2006.

[28] H. K. D. H. Bhadeshia and R. W. K. Honeycombe. *Steels: Microstructure and Properties*, chapter 7: Acicular Ferrite. Elsevier Ltd., Oxford, UK, 3 edition, 2006.

[29] Yan Chen, Dantian Zhang, Yongchang Liu, Huijun Li, and Dakun Xu. Effect of dissolution and precipitation of nb on the formation of acicular ferrite-bainite ferrite in low-carbon hsla steels. *Materials Characterization*, 84:232 – 239, October 2013.

[30] Denise Loder, Susanne Michelic, and Christian Bernhard. Acicular ferrite formation and its influencing factors-a review. *Journal of Materials Science Research*, 6:24 – 43, 12 2016.

[31] M. Mohammadijoo. *Development of a welding process to improve welded microalloyed steel characteristics.* PhD thesis, University of Alberta, June 2017.

[32] Fukuhisa Matsuda, Kenji Ikeuchi, Yasuto Fukada, Yukuhiko Horii, Hitoshi Okada, Toyoaki Shiwaku, and Chiaki Shiga. Review of mechanical and metallurgical investigations of ma constituent in welded joint in japan. *Trans. JWRI*, 24, 05 1996.

[33] N. Huda and A. P. Gerlich. A study of martensite-austenite (ma) behaviour in welded x80 linepipe steel heat affected zones. *CWA Journal*, 24:50 – 55, December 2017.

[34] O. Engler and V. Randle. *Introduction to Texture Analysis*, chapter 1: Introduction. CRC Press, Taylor and Francis Group, Boca Raton, FL, U.S.A., 2 edition, 2010.

[35] Stuart I. Wright, Matthew M. Nowell, and David P. Field. A review of strain analysis using electron backscatter diffraction. *Microscopy and Microanalysis*, 17(3):316–329, 2011.

[36] ASTM International. Standard test methods and definitions for mechanical testing of steel products. Technical Report A370-17a, May 2018. Accessed June 18, 2018.

[37] R. Bannister. The identification of low-alloy steel phase transformations and microstructure using characterization and dilatometry. Master's thesis, University of Alberta, Edmonton, Canada, 2018. Unpublished in-progress M. Sc. thesis, the Leijun Li Group.

[38] S. J. Orfanidis. *Introduction to Signal Processing*. Sophocles J. Orfanidis, Rutgers Unviversity, NJ, USA., 2010. Accessed July 16, 2018.

[39] R. Kannan, Y. Wang, R. Bannister, M. Rashid, and L. Li. Homogenization of austenite during non-equilibrium heating in hypereutectoid steels. *Materials Science & Technology*. Under Review.

[40] M. Rashid and L. Collins. Private communication., March 2017.

[41] Canadian Standards Association-CSA Group. Steel pipe. Technical Report Z245.1-14, Ninth Edition, March, 2014. Accessed June 28, 2018.

[42] Oxford Instruments. *Channel5*, September 2014. Accessed through University of Alberta nanoFab.

[43] M. Rashid and L. Collins. Private communication., July 2018.

[44] Yiyu Wang, Rangasayee Kannan, and Leijun Li. Correlation between intercritical heat-affected zone and type iv creep damage zone in grade 91 steel. *Metallurgical and Materials Transactions A*, 49(4):1264–1275, Apr 2018.

[45] M. Rashid and L. Collins. Private communication., May 2018.

[46] P. Yan and H. K. D. H. Bhadeshia. Austenite–ferrite transformation in enhanced niobium, low carbon steel. *Materials Science and Technology*, 31(9):1066–1076, 2015.

[47] N. M. Bhattacharya. *The effect of Niobium in the Heat-Affected Zone of Microalloyed Steel*. PhD thesis, University of Cambridge, May 2017.

[48] H. Nordberg and B. Aronsson. Solubility of niobium carbide in austenite. *Journal of the Iron and Steel Institute*, 206:1263–1268, 1986.

[49] J. B. Wiskel. Solubility curves precipitation. Lecture notes from MAT E 689: Advanced Processing of Microalloyed Steels, October 2016.

[50] C. Chatelier. Precipitation analysis in microalloyed x70 steels and heat treated l80 and t95 steels. Master's thesis, University of Alberta, Edmonton, Canada, 2018.

[51] P. Yan. *High Frequency Induction Welding and Post-Welding Heat Treatment of Pipe Steels*. PhD thesis, University of Cambridge, June 2011.

[52] L. Li and R.W. Messler. Stress relaxation study of heat-affected zone reheat cracking in type 347. *Welding journal*, 79:137–144, 06 2000.

[53] H. K. D. H. Bhadeshia and R. W. K. Honeycombe. *Steels: Microstructure and Properties*, chapter 4: Effects of Alloying Elements on Fe-C Alloys. Elsevier Ltd., Oxford, UK, 3 edition, 2006.

[54] R. Kannan. Predicting Bs and Ms Temperatures in Steels using ThermoCalc. Standard Operating Procedure for the Leijun Li Group, U of A. 2018, January 2018.

[55] H. K. D. H Bhadeshia. *Bainite in Steels*, chapter 5: Thermodynamics of the Bainite Transformation. The Institute of Materials, London, UK, 1992.

[56] H. K. D. H. Bhadeshia. Tempered martensite. `http://www.phase-trans.msm.cam.ac.uk/2004/Tempered.Martensite/tempered.martensite.html`. Accessed June 18, 2018.

[57] J.W. Christian. Thermodynamics and kinetics of martensite. Number Proceedings of the International Conference on Martensitic Tranformations (ICOMAT), pages 220–234, 1979.

Appendix A

Specimen Details of PWHT T$_P$ Study - CVN Testing

A.1 Additional CVN Testing Details

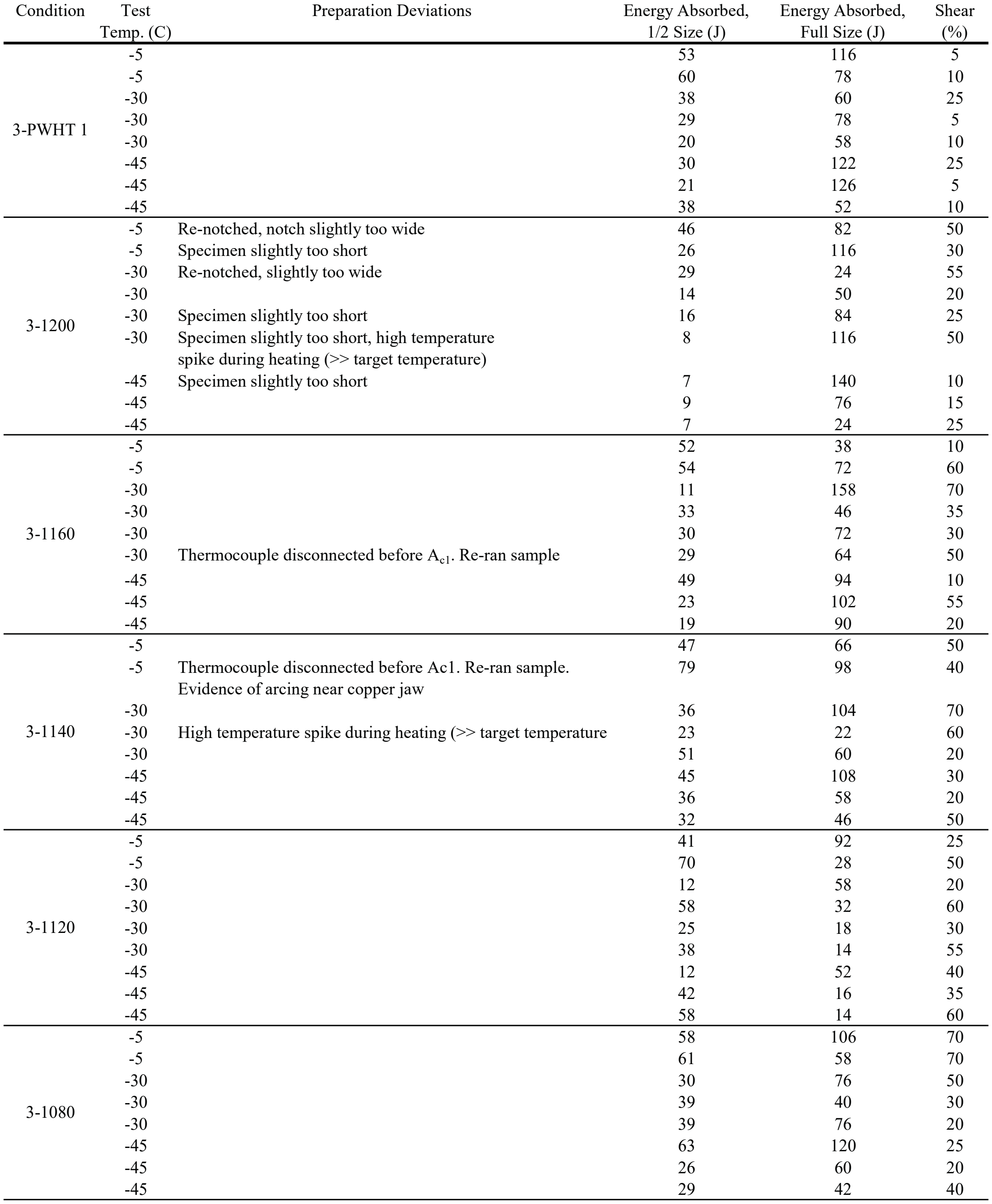

Condition	Test Temp. (C)	Preparation Deviations	Energy Absorbed, 1/2 Size (J)	Energy Absorbed, Full Size (J)	Shear (%)
3-PWHT 1	-5		53	116	5
	-5		60	78	10
	-30		38	60	25
	-30		29	78	5
	-30		20	58	10
	-45		30	122	25
	-45		21	126	5
	-45		38	52	10
3-1200	-5	Re-notched, notch slightly too wide	46	82	50
	-5	Specimen slightly too short	26	116	30
	-30	Re-notched, slightly too wide	29	24	55
	-30		14	50	20
	-30	Specimen slightly too short	16	84	25
	-30	Specimen slightly too short, high temperature spike during heating (>> target temperature)	8	116	50
	-45	Specimen slightly too short	7	140	10
	-45		9	76	15
	-45		7	24	25
3-1160	-5		52	38	10
	-5		54	72	60
	-30		11	158	70
	-30		33	46	35
	-30		30	72	30
	-30	Thermocouple disconnected before A_{c1}. Re-ran sample	29	64	50
	-45		49	94	10
	-45		23	102	55
	-45		19	90	20
3-1140	-5		47	66	50
	-5	Thermocouple disconnected before Ac1. Re-ran sample. Evidence of arcing near copper jaw	79	98	40
	-30		36	104	70
	-30	High temperature spike during heating (>> target temperature	23	22	60
	-30		51	60	20
	-45		45	108	30
	-45		36	58	20
	-45		32	46	50
3-1120	-5		41	92	25
	-5		70	28	50
	-30		12	58	20
	-30		58	32	60
	-30		25	18	30
	-30		38	14	55
	-45		12	52	40
	-45		42	16	35
	-45		58	14	60
3-1080	-5		58	106	70
	-5		61	58	70
	-30		30	76	50
	-30		39	40	30
	-30		39	76	20
	-45		63	120	25
	-45		26	60	20
	-45		29	42	40

Figure A.1: Summary of all CVN specimens and testing results

Appendix B

Determination of Phase Transformation Temperatures

B.1 Equilibrium Ferrite, Bainite, and Martensite Start Temperatures

Prediction of the start temperatures for Widmanstatten ferrrite or acicular ferrite (paraequilibrium ferrite and paraequilibrium cementite), bainite, and martensite on cooling from austenite is possible using the console mode of ThermoCalc, and has been shown to have an accuracy within 10-15 K of experimental results for hypereutectoid steels [54]. This methodology is based on the concept that the Gibb's free energy of diffusionless transformations have several components; a chemical composition component, a strain energy component, and other structural components such as twinning or, in the case of martensite, solute carbon trapping [55, 56].

This is accomplished by first calculating a T_0 versus C content (wt%) curve of the composition of interest using ThermoCalc. As ThermoCalc only considers the chemical composition component of Gibb's free energy, this is appropriate for the calculation of the ferrite start temperature [54]. However, since the bainite and martensite transformations from austenite also have an associated strain energy component of Gibb's free energy, a manual addition of the appropriate strain energy for the diffusionless transformation is necessary to reach a more accurate total Gibb's free energy of transformation, and subsequently a more accurate transformation start temperature. In addition, for martensite, it is also necessary to include the addition of a free energy term to capture the the trapping of carbon atoms; while the energy associated with twin interfaces can also be included for martensite (100 J/mol), it was assumed to be negligible no twins were observed in microstructural samples, and the martensite fractions were observed to be low. The strain energy component additions are summarized in Table B.1. The produced transformation start temperatures for the range of 0 - 0.1 wt% C can be seen in Fig. B.1.

Table B.1: Energy of transformation assumptions.

Microstructure	Chemical component of free energy, J/mol (Calculated by ThermoCalc, gives T_0)	Associated strain energy, J/mol	Free energy of trapping carbon in martensite, J/mol	Total Energy, J/mol
Ferrite (Widmanstatten and Acicular)	385	-	-	385
Bainite	385	400 [55]	-	785
Martensite	385	600^+ [56]	100^*	1085

$^+$ 600 J/mol is a slight overestimation since only the elastic strains are considered [57]. In reality the energy may be reduced by plastic deformation in surrounding austenite [54].

*Varies with respect to carbon content. Estimated from [56]

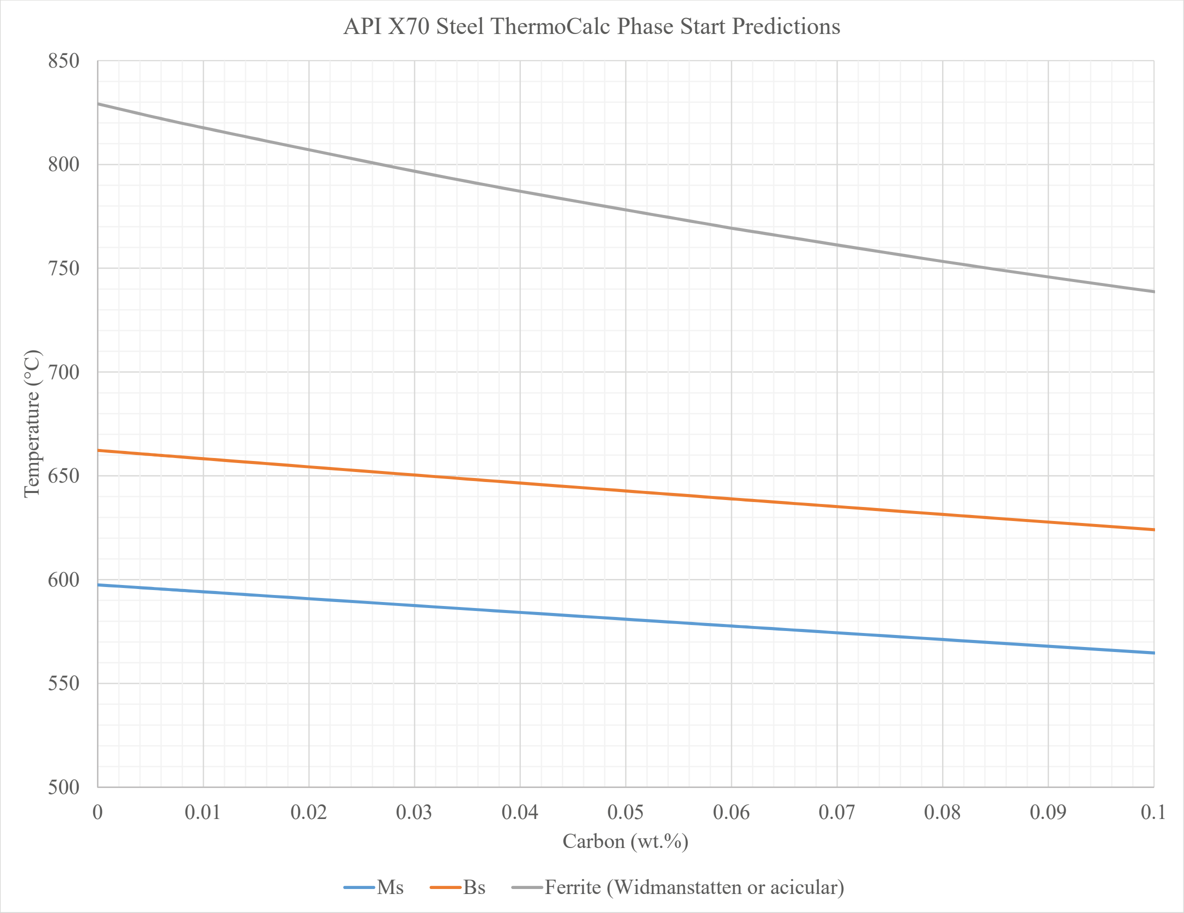

Figure B.1: Calculation of start temperatures on cooling from austenite as a function of carbon content for Widmanstatten or acicular ferrite, bainite, and martensite of a representative X70 chemistry similar those from PWHT 1. Calculated from ThermoCalc.

B.2 Determination of Transformation Temperatures from Dilatometry Curves

Transformation temperatures during the simulated PWHT cycles were determined as per the methods described in ASTM A1033 [36]. A representative curve is shown in Fig. B.2. Transformation start and ends were determined as deviations from the linear slope (of thermal expansion or contraction on heating or cooling respectively). A more detailed description of methodology used to analyze dilatometry data can be found in the thesis of Rebekah Bannister of the University of Alberta [37].

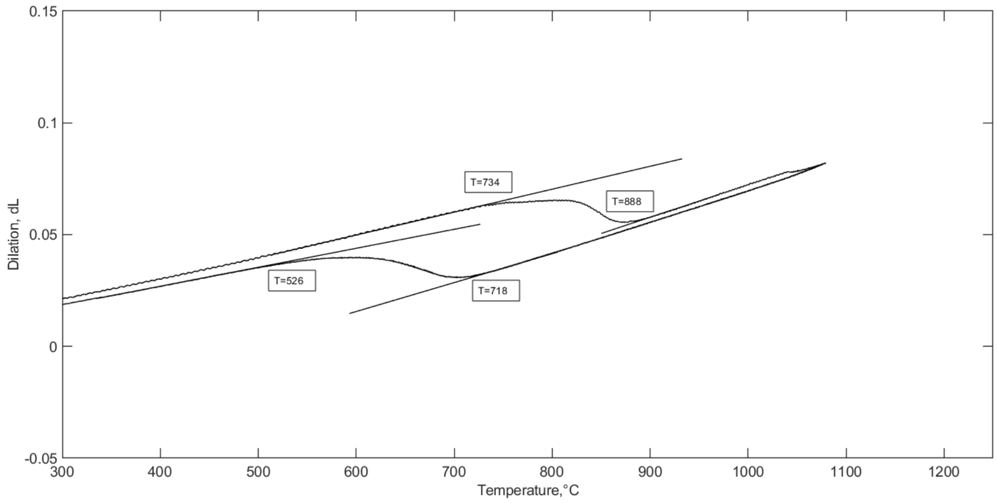

Figure B.2: A representative dilation curve used to accurately identify the transformation temperatures during PWHT simulations. Specimen 3-1080.

∗ References [36, 37, 54-57] can be found in *Bibliography* starting on page 106.

Appendix C

Detailed Dilatometry Curves

C.1 Evidence of Material Response Regimes from Dilatometry Curves

Analysis was carried out as described in *Chapter 2*. Austenitization is identified as the most prominent transformation in the material; by taking the derivative it can be seen that this region is actually composed of two different distinct transformations. After austenitization, subtle transformations are evident in the derivative curve; these are suspected to be precipitate phases such as niobium carbo-nitrides dissolving into austenite, although the exact temperature and number of these transformations can be somewhat obscured by signal noise in some specimens, despite efforts at smoothing. The circled "peaks" in red for the 3-T_P curves are suspected to be evidence of latent heat during transformations. Due to a changes in heating rate during the normalizer 2 - normalizer 3 interval due to changes in the PWHT cycle, these peaks become more or less obvious. The peaks are most obvious in the lower peak temperature specimens, which had heating rates more similar to equilibrium, and the least obvious in the high peak temperature specimens, which had a much higher heating rate, this assumption seems reasonable. The deviation in slope on the dilation versus temperature curve after this peak is likely due to diffusion driven homogenization of the recently dissolved alloying elements [39]. While it is unknown if the change in heating rate may have exacerbated the slope deviation, this slope change was also observed in constant heating rate dilatometry of a similar X65HIC material by Yan (see *Figure 6.1: Simulation of induction welding on X65HIC base metal. pg. 111.*) [51]. A similar phenomenon was observed in austenitic stainless steel during isothermal heat treatments which dissolved Nb(C,N), where strain levels decreased over time [52]. This is attributed to precipitates causing a larger lattice strain than the elements in solution, leading to a strain relaxation as precipitates are dissolved into the austenitic matrix and the specimen shrinks [52]. This shrinkage in lattice size results in a deviation downwards in the dilation versus temperature curve. This leads to confidence in the evidence for homogenization. A representative example is shown in Fig. C.1.

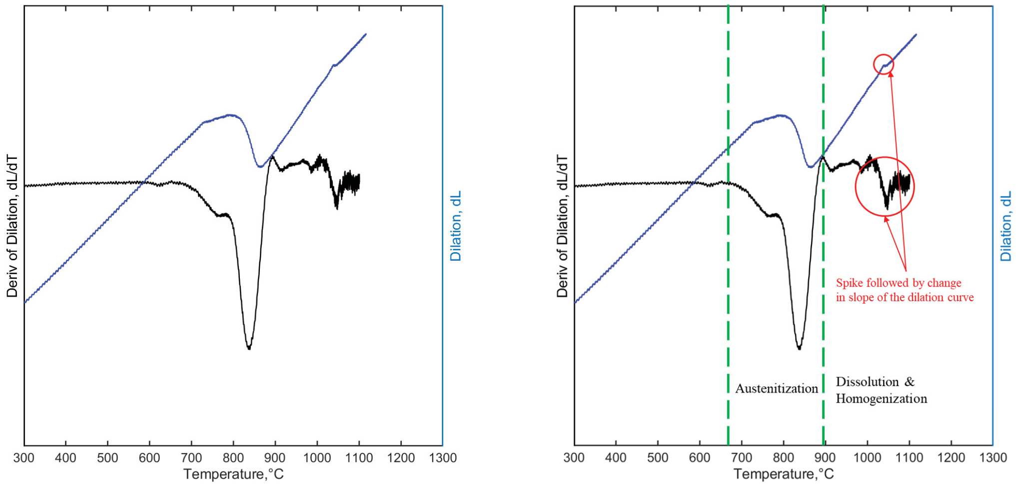

(a) 3-1120 dilatometry curve with derivative of dilation.

(b) Same as (a), marked with different material response regimes.

Figure C.1: Representative dilatometry curve showing different regimes of material response during the heating aspect of the PWHT cycle.

For all specimens in the PWHT 3 peak temperature study, dilatometry curves subject to derivative analysis and marked with the regions of austenitization, and dissolution and homogenization are shown in Fig. C.2.

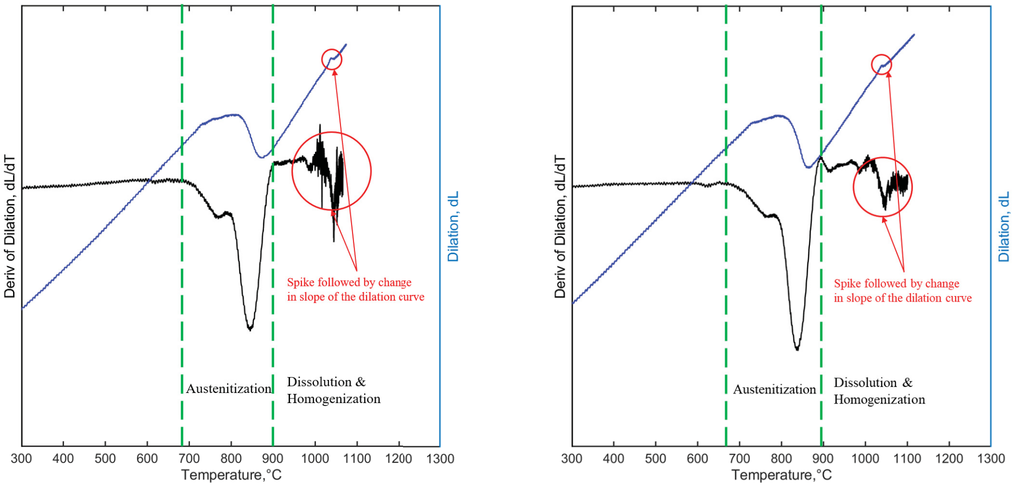

(a) 3-1080. **(b)** 3-1120.

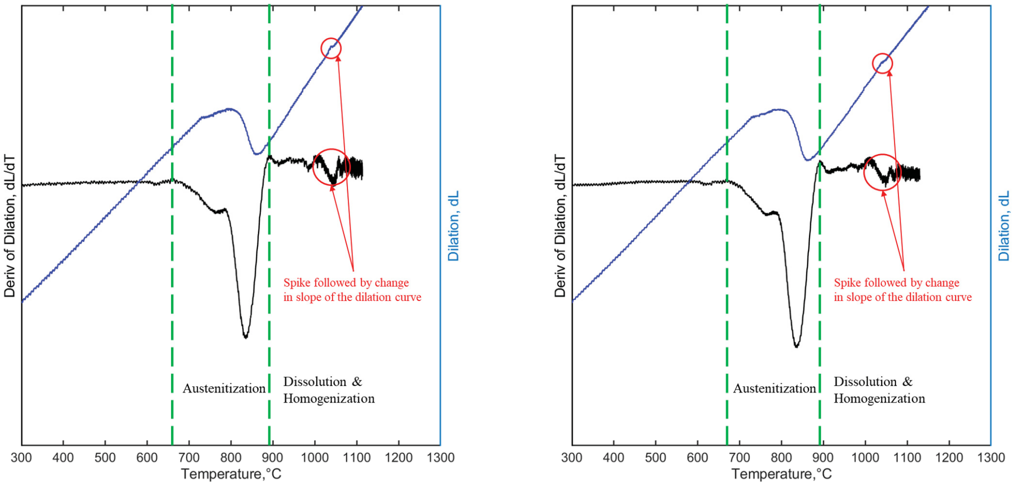

(c) 3-1140. **(d)** 3-1160A.

Figure C.2: Detailed dilatometry curves for T$_P$ trial. (cont.)

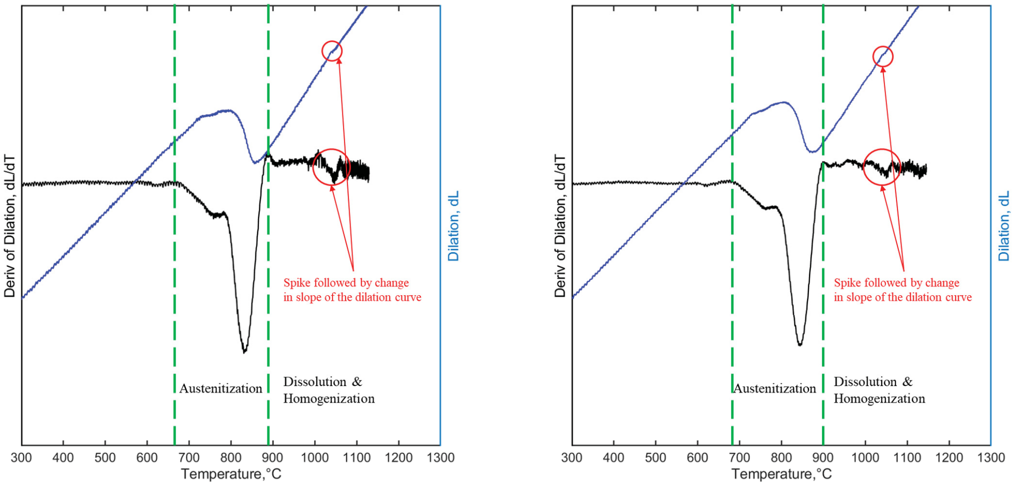

(e) 3-1160B. **(f)** 3-1180.

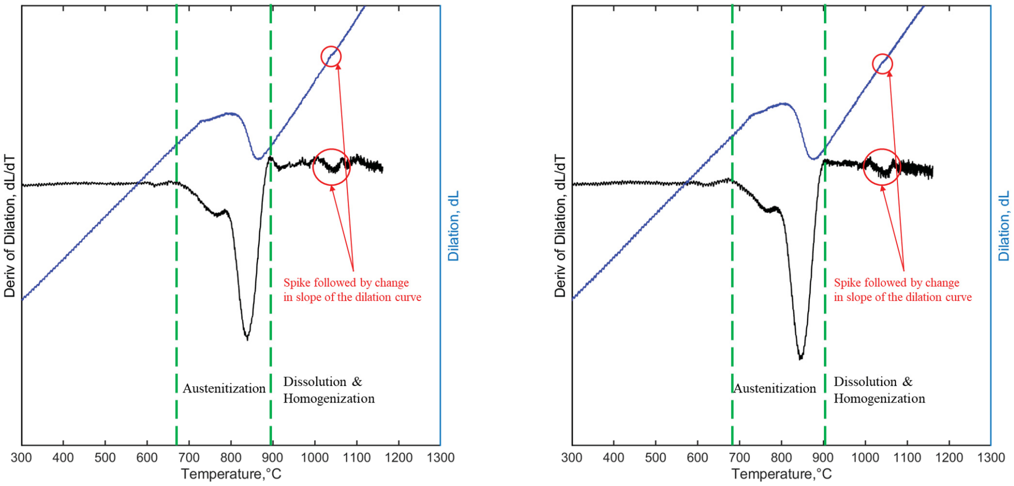

(g) 3-1200A. **(h)** 3-1200B.

Figure C.2: Detailed dilatometry curves for T$_P$ trial. (cont.)

∗ References [39, 51, 52] can be found in *Bibliography* starting on page 106.